Deciphering triangular fracture patterns in PMMA : how crack fragments in mixed mode loading

Aditya Vangal Vasudevan

THÈSE DE DOCTORAT
DE L'UNIVERSITÉ PIERRE ET MARIE CURIE

Spécialité : Mécanique

École doctorale : Sciences mécaniques, acoustique, électronique et robotique de Paris (ED 391 SMAER)

réalisée

au Institut Jean le Rond ∂'Alembert

présentée par

Aditya Vasudevan

pour obtenir le grade de :

DOCTEUR DE L'UNIVERSITÉ PIERRE ET MARIE CURIE

Sujet de la thèse :

Deciphering triangular fracture patterns in PMMA : How crack fragments in mixed mode loading

soutenue le 1er Fevrier 2018

devant le jury composé de :

M.	Adda-Bedia Mokhtar	Rapporteur
M.	Bonamy Daniel	Rapporteur
M.	Baumberger Tristan	Examinateur
M.	Ciccotti Matteo	Examinateur
M.	Karma Alain	Examinateur
M.	Krishnaswamy Ravi-Chandar	Examinateur
M.	Leblond Jean-Baptiste	Examinateur
M.	Ponson Laurent	Directeur de thèse

List of Figures

List of Tables

Contents

Abstract

Cracks when they propagate leave complex patterns behind on the broken material. Deciphering these fracture patterns has always been crucial in framing the basic laws of fracture mechanics. In this work, I study the fracture surfaces of PMMA. At high velocities, $v \simeq 200\text{ms}^{-1}$, the fracture surface is optically smooth. However at the critical velocity $v \simeq 15\text{mms}^{-1}$, we observe a roughening transition characterized by puzzling triangular patterns on the fracture surface. We investigate in detail this transition both experimentally and theoretically. When probed through a profilometer, these patterns show step-like features reminiscent of the facet formation in the so-called crack front fragmentation under tensile and anti-plane shear. The current models predict a critical mode mixity ratio for fragmentation much larger than the experimental values. We revisit these models by assuming a shear dependent fracture energy and show that the threshold may drop significantly. The model predictions are directly tested in our experiments. First, the geometry of the triangular patterns are used to measure the macroscopic shear and anti-plane shear applied to our tensile test specimens. Then, the parameters characterizing the dependency of the fracture energy with the anti-plane shear are extracted using the in-plane deformation of the crack resulting from its fragmentation on some localized region of the front. Finally these parameters are used to predict the critical mode mixity ratio for fragmentation that is found to be the order of a few percent in PMMA. This theoretical threshold is found to be in excellent agreement with the experimentally measured value. Our work opens new perspectives for understanding front fragmentation in other experiments and explain the variations observed from one material to another.

Chapter 1

Introduction

How often has one's smart phone slipped from his/her hand only to ruefully find out that the fall was fatal and cracked the screen completely? After the initial phase of sadness when one looks at the broken screen one then sees a fascinating pattern, quite hierarchical with a combination of long and small cracks. Some other fracture patterns observed in our daily lives are wandering crack patterns on a wall, polygonal patterns in drying mud or paint, network of cracks in some geological formations etc. Cracks when they propagate through a material leave beautiful patterns in its wake [Hull, 1999]. These patterns provide useful information about the mechanics and physics of failure. The field of fracture mechanics has largely benefited from the observation, characterization and then the interpretation of various types of fracture patterns. In this perspective, failure is seen as a pattern formation mechanism and failure patterns are used as benchmarks that allow to probe and validate the fundamental laws ruling the behavior of cracks. In this thesis I will focus on a specific kind of fracture pattern seen on PMMA fracture surfaces (but not only as I will discuss later) and I will show how one can harness them to study the mechanics and physics of cracks under mixed load loading.

This introductory chapter is organized as follows. In the first section we remind briefly the basic laws of fracture mechanics, the criteria allowing to predict crack growth and crack path and I will introduce as a pattern formation mechanism the concepts of modes I II and III. Next I review, some classical fracture experiments that contributed to reveal and validate the basic laws of fracture mechanics. In the last section I present another perspective in the study of fracture and discuss through some examples how fracture pattern can be used to measure material properties such as toughness.

1.1 Basic fracture mechanics concepts

Fracture can be investigated from multiple scales [Chang and Rudnicki, 2000]. At the atomic scale, it can be seen as the separation of atomic planes. At the microstructure scale of the material like grains in a polycrystalline material or fibers in a composite, complex interaction between cracks and heterogeneities or defects take place. These processes increase the amount of energy dissipated during crack growth and largely influence the toughness of materials. At an even larger scale, the material can be described as a continuum which allows us to analyze fracture through concepts of stress, strain and

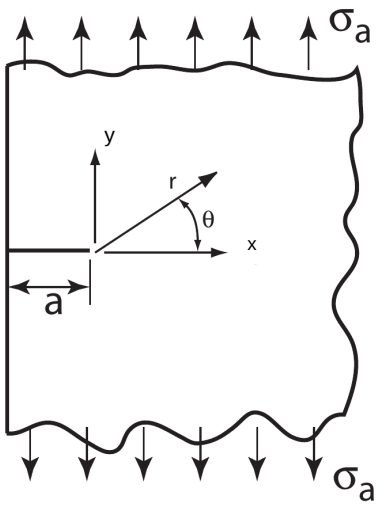

Fig. 1.1 *Edge crack in a plate in tension (taken from [Zehnder, 2012])*

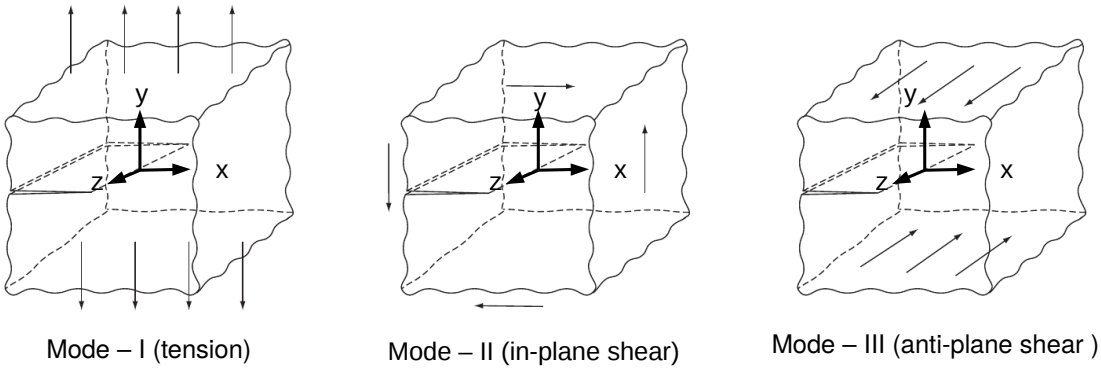

Fig. 1.2 *The three different modes of fracture. A material can break under one or more than one of these modes. (taken from [Zehnder, 2012])*

elastic energy release rate. In this thesis, I investigate fracture at this continuum scale.

Consider a crack of length a on the edge of an infinite plate under a tensile stress σ_A (see Fig. 1.1). The external loading will control the amplitude of stress at the tip of the crack and beyond a certain level, the crack will start to propagate leading ultimately to the failure of the specimen. Using linear elasticity, the above problem can be solved for the displacement and the stress field. At a distance r from the crack tip and at an angle θ w.r.t x, the stress field at the crack tip vicinity is given by

$$\begin{pmatrix} \sigma_{rr} \\ \sigma_{\theta\theta} \\ \sigma_{r\theta} \end{pmatrix} = \frac{K_I}{\sqrt{2\pi r}} \frac{1}{4} \begin{pmatrix} -\cos\frac{3\theta}{2} + 5\cos\frac{\theta}{2} \\ \cos\frac{3\theta}{2} + 3\cos\frac{\theta}{2} \\ \sin\frac{\theta}{2} + \sin\frac{3\theta}{2} \end{pmatrix} + \mathcal{O}(1) \tag{1.1}$$

In Eq. (1.1), the first term shows a scaling to the inverse of $\sqrt{r}$ which implies that as

we approach the crack tip, the stress field diverges. This is not realistic as no material can sustain such a high stress level. Thus, there must exist a small zone of size l_{pz}, the so-called process zone where dissipative failure processes take place and where Eq. (1.1) cannot be applied. If this process zone is small enough, $l_{pz} \ll a$, one can still use the stress field given in Eq. (1.1). This is called the "small scale yielding" condition which states that all dissipation processes occur in this zone and the material behaves elastically outside this zone. For $l_{pz} \ll r \ll a$ the level of the loading and geometry are reflected by a single quantity, K_I, which is called the "stress-intensity factor". In the fracture geometry of Fig. 1.1, it is given by $K_I = 1.12\sigma_a\sqrt{\pi a}$. If two different setups in terms of loading and geometry share however the same stress-intensity factor K_I, then the responses of the crack will also be the same.

1.1.1 Griffith criterion

When a crack grows, some elastic energy is released from the material and transferred to the crack tip at a rate called the energy release rate, G. If this rate is greater than or equal to the required energy, G_c the crack propagates, so one can write

$$G \geq G_c \tag{1.2}$$

This is the so-called Griffith's criterion [Griffith, 1921] and G_c is termed as the fracture energy or fracture toughness. This energy includes all the energy dissipated within the process zone which could be through different mechanisms such as plasticity, damage, void growth, microcracking, acoustic emissions etc. This fracture energy is a property of the material while G depends on the elastic properties of the material, on the loading, geometry and the crack length. It relates to the stress intensity factor introduced in the previous section through the relation $G = \frac{K_I^2}{E}$, where E is the material Young's modulus. This criterion has been successfully applied in explaining to predict growth in a broad class of materials under pure tension.

1.1.2 Modes of fracture

The stress field at the crack tip can be broken into three components, mode I, mode II and mode III as shown in Fig. 1.2. Mode I causes the crack to open orthogonally (along y) to the fracture surface. Mode II causes the crack to slide relatively to the original direction (along x) of the crack. It measures in-plane shear stresses in the x direction. Mode III causes the crack to twist (along z). It measures the anti-plane shear along z. Each of these loading modes can be quantified by the stress-intensity factors K_I, K_{II} and K_{III}. Any complex loading can be expressed as the sum of these which can then be superimposed with different intensities.

1.1.3 Criteria for mixed mode failure

In the previous example of Fig. 1.1, the crack path is prescribed and failure takes place if the Griffith's criterion of Eq. (1.2) is satisfied for a straight crack advance along the x - direction. In the general case, the crack propagation direction is not know a priori. Therefore a crack path criterion is required. In particular, under mixed mode loading

conditions, cracks tend to deviate from straightness and may follow complex trajectories. In 2D, for a problem invariant along the z direction, different criteria have been proposed: (i) maximum circumferential stress[Erdogan and Sih, 1963] (ii) minimum strain energy density[Sih, 1972] (iii) maximum energy release rate [Wu, 1978]and (iv) principle of local symmetry[Gol'dstein and Salganik, 1974]. They all are able to capture reasonably well the kink angles of a crack [Zehnder, 2012]. However, which of these criterion is the most general? In the coming section, I review some experiments which have been decisive in formulating the basic laws of fracture mechanics.

1.2 Crack patterns as a way to probe the basic laws of fracture mechanics

In the previous section we saw that the stress intensity factors depend on both the loading conditions and the specimen geometry. Thus different loading and geometries may lead to a plethora of fracture patterns. Figure 1.3 shows a few fracture patterns observed in recent years. Each of these patterns showed some interesting features which potentially can reveal the basic laws underlying the behavior of cracks. As I will discuss below, their study indeed led to the extension or the confirmation of some fundamental concepts of fracture mechanics.

Figure 1.3 (a) and (b) show an oscillatory instability obtained when a hot glass plate is quenched in a cold bath at some fixed velocity. If the difference in the temperature between the plate and the bath is low, then this feature is absent and the crack propagates straight. At higher temperature differences, an oscillatory instability is triggered which gets chaotic at very high temperature differences [Yang and Ravi-Chandar, 2001, Yuse and Sano, 1993]. Using a double criterion based on $G = G_c$ and $k_{II} = 0$ called the principle of local symmetry, this oscillatory path could be very well captured. In particular, it was found that the criterion $k_{II} = 0$ could be used to predict the onset of this instability and the wavelength of the oscillations[Adda-Bedia and Pomeau, 1995, Corson et al., 2009], establishing the principle of local symmetry as a criterion to predict the crack paths in 2D brittle solids.

Brittle gels show another type of oscillatory instability [Bouchbinder et al., 2010, Livne et al., 2007](see Figure 1.3 (f)) where cracks propagating at high velocities ($v \simeq 0.9\ v_R$ where v_R is the Rayleigh wave speed) show oscillatory out-of-plane excursions with a certain wavelength. These oscillations are understood as an effect of the non-linear elasticity of brittle gels. A new framework developed from non-linear elasticity, the so-called non-linear elastic fracture mechanics (NLEFM) was found to explain very well this oscillatory instability thus providing a way to test and improve the theoretical framework. Another fascinating example is the telephone cord buckling patterns (see Figure 1.3(c)) observed during delamination of thin films from soft substrates under low adhesion[Gioia and Ortiz, 1997]. Interestingly, assuming quantitatively a dependency of the fracture energy on the mode mixity (I and II) was required to decipher these patterns [Faou et al., 2012]. This represented a striking evidence that fracture energy often thought of as a constant parameter may vary with the local loading conditions applied at the crack tip vicinity.

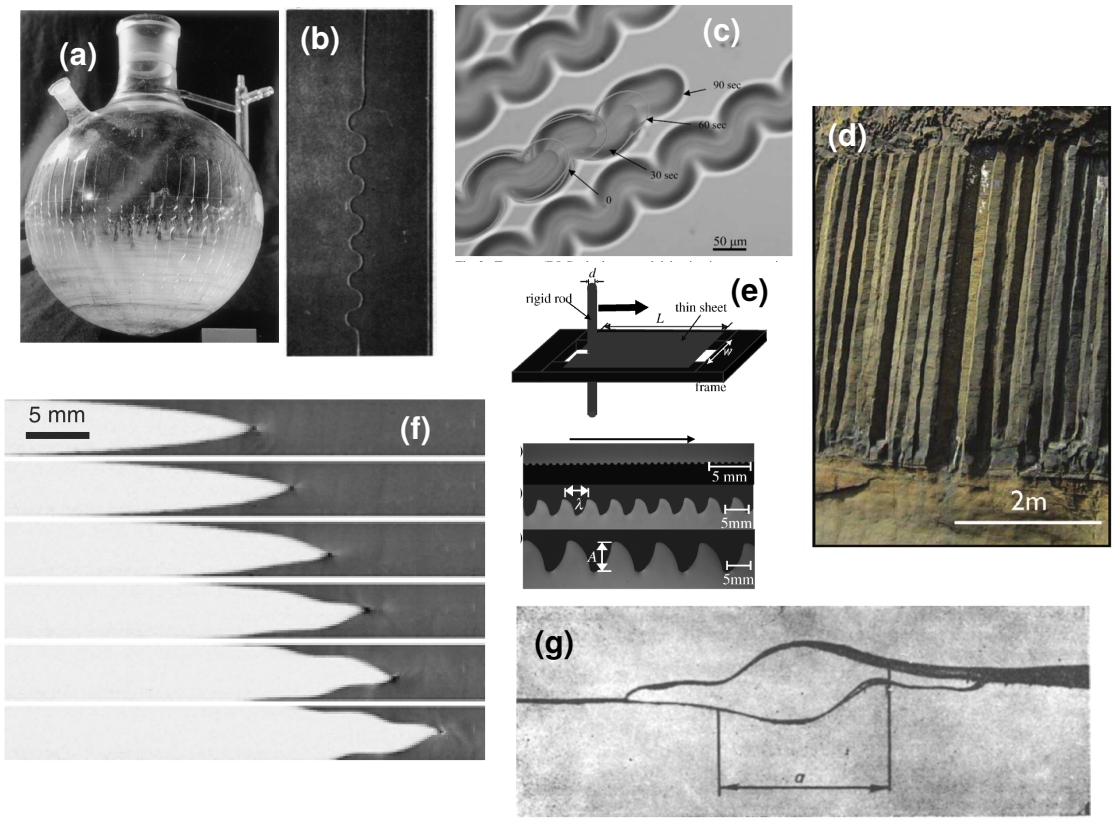

Fig. 1.3 *Variety of fracture patterns created by different materials under certain conditions: (a) and (b) Oscillations in the crack path obtained by the quenching of a glass plate in a cold bath[Bahat, 1991, Yuse and Sano, 1993] (c) Telephone cord buckling fracture patterns are formed when a thin film delaminates from a substrate under low adhesion[Waters and Volinsky, 2007] (d) Columnar joint basalt columns at Fingal's cave[Goehring et al., 2009] (e) Visually arresting crack street when a cylindrical tool cuts through a thin sheet [Ghatak and Mahadevan, 2003](f) Oscillatory instability in brittle gels at high velocities[Bouchbinder et al., 2010] (g) Interaction of two finite cracks at a fixed distance from each other[Eremenko et al., 1979]*

Sometimes, even apparently simple experiments can be used to challenge established laws of fracture mechanics. One such example is the case of two initially straight, parallel and offset cracks interaction. They first show a repellent behavior and then attract before each other. Using the principle of local symmetry one could not explain such a behavior [Dalbe et al., 2015b]. This suggests that plastic deformation close to the crack tip might have to be taken into account to make realistic prediction of crack paths. Another such unresolved pattern till date is the crack propagation in mixed mode I + III: a dominantly tensile loading with a small amount of mode III are observed to fragment the crack along its front into smaller segments forming lances or facets [Sommer, 1969] on the fracture surface. Cracks under mode III necessarily need a 3D treatment, as a small amount of mode III twists the crack causing it go out-of-plane. Does the principle of local symmetry, which was shown to be successful in 2D, also applies in 3D ? In addition, the dissipation rate for a crack under pure mode I may be different to that of a crack under mode I + III, the same way fracture energy was found to depend on the mode mixity ratio K_{II}/K_I. If so, how to describe the variations of G_c with K_{III}/K_I and how to measure them ? We will address these questions later as both laws are crucial in understanding fracture patterns that we will study in the following.

Looking at the study of fracture patterns from another point of view, we now discuss how they may be used to measure some material properties like fracture toughness.

1.3 Fracture surface analysis as a tool to extract material properties

Post-mortem fracture surface of a material not only help us in understanding the physical mechanisms involved during fracture and derive criteria for fracture initiation, but also can act as a tool to extract material properties which are otherwise hard to measure. The first example relates to the statistics of crack roughness. Studies on fracture surface morphologies show that fracture surfaces are rough and show fractal behavior [Mandelbrot et al., 1984]. Their statistics are characterized by anisotropic scaling exponents and along the crack front direction, the scaling exponent are found to be $\zeta \simeq 0.4$ for brittle failure and $\zeta \simeq 0.8$ for damage driven failure[Bonamy and Bouchaud, 2011, Ponson et al., 2006]. The value of these exponents are found to be universal and reminiscent of the microscopic mode of failure (brittle vs damage coalescence). A recent study [Srivastava et al., 2014] shows however, a correlation between the cut-off of the self-affine regime emerging from damage coalescence processes and the fracture energy of the material. This finding is now [Vernède et al., 2015] exploited in quantitative fractography to measure the fracture energy from the statistical analysis of fracture surfaces.

Another relevant example comes from dynamic fracture in PMMA where cracks leave certain characteristic parabolic shaped marks on the fracture surface called “conic marks” [Ravi-Chandar and Yang, 1997],[Guerra et al., 2012]. These conic marks are signatures of the microcracking process taking place ahead of the main crack tip and the interaction between the microcracks and the arriving crack leaves these conic marks on the fracture surface. These conic marks were then used to trace back the full history of the crack and the micro cracks with time and space resolution of $1\mu s$ and $1\mu m$. Pushed even further, this analysis even served as a way to measure the fracture toughness of PMMA at high

velocities. More studies are necessary in the area of measuring the fracture surface morphology, but it can serve as a strong tool to measure the fracture properties of the material.

In this thesis, I will focus on a puzzling pattern present on PMMA fracture surfaces, in the transition region between an optically smooth region corresponding to large crack speed and a rough region characterized by facets that correspond to low crack speeds. Figure 1.4 shows an optical image of the transition region that displays triangular patterns. By exploring the mechanisms at the origin of their formation, we will also try to understand the roughening transition and identify the parameters that control this transition. We will find that a mode III dependent fracture energy is crucial to understand the transition from flat to rough, and we also present a methodology to extract the variations of the fracture energy with the amount of anti-plane shear from the triangular patterns.

1.4 Outline of the thesis

This thesis is organized as follows : In Chapter 2 we present fracture experiments used to study the roughening transition in PMMA and investigate the mechanical conditions under which this transition occurs. Chapter 3 and 4 present a theoretical calculations of the crack front behavior under mode mixity I + II + III which are intended to provide the theoretical concepts that will be used later to interpret the patterns seen in our experiments. In particular chapter 3 deals with the study of the in-plane and out-of-plane deviation of a crack front pinned by a obstacle and in the presence of mode I, II and III. Chapter 4 explores theoretically the fragmentation of a crack front under mode I + II + III. This is achieved through a linear stability analysis with dependency of the fracture energy with mode III. Finally in Chapter 5 all these theoretical derivations are connected and used to decipher the triangular fracture patterns observed on the fracture surface.

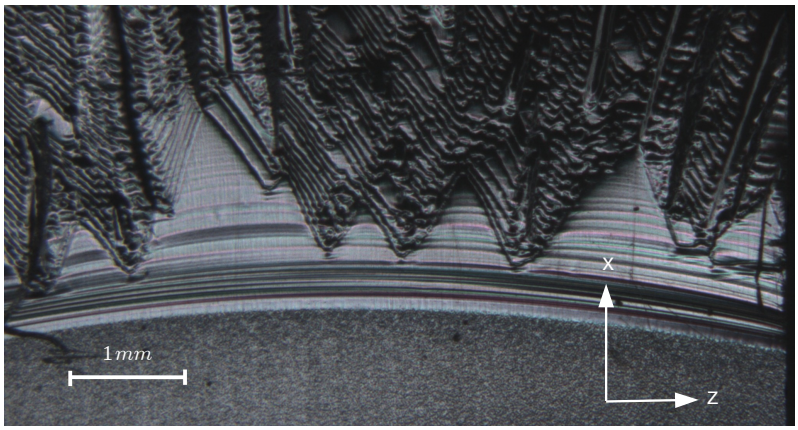

Fig. 1.4 *Triangular fracture pattern observed at the transition from a fast to slow failure in PMMA fracture surfaces. Crack is propagating in the positive x direction*

Chapter 2

Fracture experiments in PMMA

Contents

In this chapter I introduce a new fracture test geometry that has been designed to investigate the failure behavior of brittle solids over a wide range of velocity and that we apply here to study the roughening transition in PMMA. I will first present the application of this test to the study of the fracture properties of materials under pure mode I at low crack velocities and will finally present its implementation for the study of the dynamics of a rapid crack slowing down from very fast to slow speeds.

2.1 Design of a modified TDCB test

A schematic of the proposed fracture test geometry is shown in Fig. 2.1(a). Similar fracture tests have been used in the past (see for example Davalos et al. [1998],Qiao et al. [2003],Blackman et al. [2003] to measure the fracture properties of adhesively bonded joints and Morel et al. [2003] for the study of the R-curve behavior of quasi-brittle solids).

However the specimen used had narrow arms before the taper part of the sample. We have modified this feature by removing this narrow section, resulting in a better control of the crack evolution. Indeed, as I will show later, this new design renders the crack propagation very stable, both from a trajectory perspective and from a dynamics point of view. In other words, the crack path remains rather straight while its speed can be fully controlled by the opening rate imposed to the specimen by the loading machine. To assess the fracture properties of the material, we use a classical technique based on the measurement of the compliance of the sample during crack propagation. We theoretically predict the compliance using finite elements as a function of crack length that we compare to the compliance measured during the test to track the crack tip position.

We describe first our finite element calculations. The sample dimensions are written as a multiple of the mesh size. Quadrilateral square elements are used and the mesh size in both the x and y directions are denoted as $e_x = e_y$. A typical specimen has dimensions $h_1 = 120e_x$, $h_2 = 180e_x$, $L = 400e_x$, $l_x = l_y = 60e_x$ and $R = 12e_x$ that correspond to $h_1 = 3$ cm, $h_2 = 4.5$ cm, $L = 10$ cm, $l_x = l_y = 1.5$ cm and $R = 0.3$ cm with $e_x = e_y = 250\mu$m in our experiments. We run 2D plane stress calculation as we assume that the problem is invariant in the third direction z.

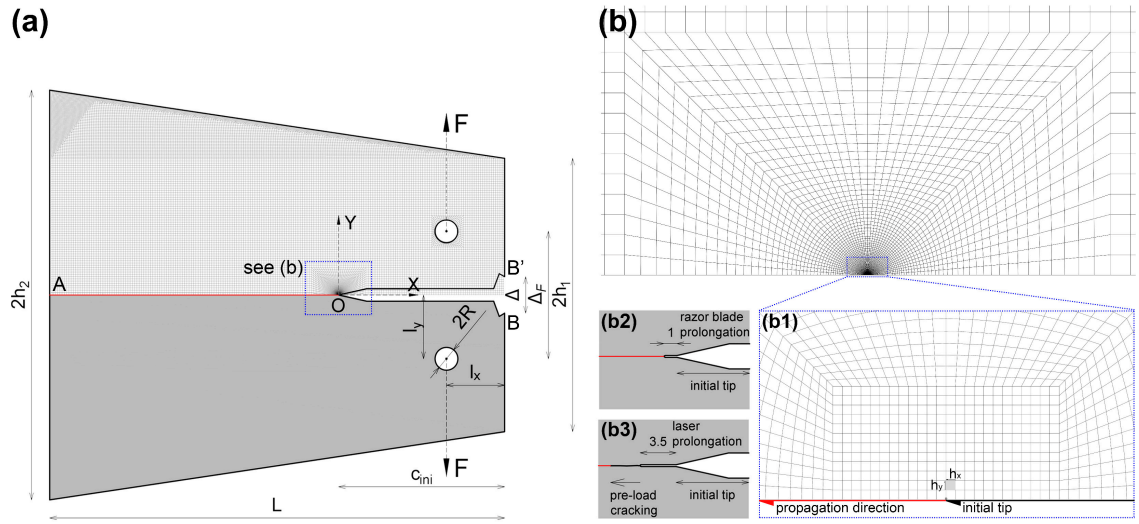

Fig. 2.1 *(a) Schematic of the sample geometry with the finite element mesh superposed on the upper half (b) Finite element mesh at the crack tip vicinity. Note the exponential decay of the mesh size as one gets closer to the crack tip. The mesh used for analysis contains about $\sim 10^5$ nodes and about 2×10^5 dof. (b2) and (b3) show the experimental methodology employed to prepare the tip of the notch and ensure a smooth crack initiation.*

CASTEM open-source finite element package developed by CEA in France is used for the calculations. A typical mesh used in the analysis is shown in Fig. 2.1(b). Exploiting the sample symmetry, we carry out the simulations on the upper half of the sample only and fix the displacements on the crack ligament (red segment OA in 2.1.(a)). A unit vertical force is applied on the hole and describe the force imposed to the sample

by the pins. These boundary conditions ensure a pure mode I fracture in the specimen. Crack length is increased incrementally and the corresponding elasticity problem is solved under plane stress and linear elastic conditions. We extract the displacement δ_F and δ at the point of application of the force and at the location of the clip gauge (B' in Fig. 2.1(a)) respectively. We define the ratio $r = \delta_F/\delta$ that turns out to depend weakly on the crack length and remains close to $r \sim 0.8$. The compliance at these two locations defined as the ratio of the displacement over the force are computed and noted as λ_F and λ respectively. Note that they are related by the same ratio r. All the following calculations are performed using the compliance at the point of application of the force. But as we experimentally measure the crack opening displacement in B' using a clip gauge (see Fig. 2.4) we relate both quantities using the ratio r. We assume a Poisson's ratio $\nu = 0.37$ that correspond to PMMA and set the Young's modulus E to unity as it is subsequently corrected analytically in the expressions of the compliance and elastic energy release rate. Note that the computed value of the compliance λ_F and stress intensity factor K_I in our 2D simulations depend only slightly on the Poisson's ratio.

2.1.1 Finite Element analysis of the modified TDCB sample

A semi-log plot of the non-dimensional compliance as a function of crack length obtained from the finite element solution is shown in Fig. 2.2. We see that for a certain range of crack lengths, the dependence of the compliance on the crack length can be described by an exponential function (black solid line in Fig. 2.2):

$$\lambda_F = \frac{\lambda_0}{Eb} e^{c/c_0} \tag{2.1}$$

where E is the Young's modulus, b the thickness of the specimen while λ_0 and c_0 are the parameters of the exponential fit. The compliance follows an exponential increase in a mid-range of crack lengths from $L/3 < c < 2L/3$, where L is the specimen length along the propagation direction. Once the crack reaches the vicinity of the free surface, the ligament becomes very small and the compliance increases faster than an exponential and it deviates away from the exponential fit. The compliance scales as $1/Eb$ so we plot the non-dimensional compliance λEb as a function of crack length that is normalized by c_0.

We then perform a systematic analysis on the scaling of the parameters of the fit by performing simulations for different geometries. We choose two different geometries (for dimensions see Fig. 2.2) and also vary the length L of the specimen along the propagation direction. The inset of Fig. 2.2 shows the parameter c_0 extracted from the fit for all the simulations. It depends only on L and varies as $c_0 = 0.388L - 91.5$. We find the other fitting parameter scales as $\lambda_0 \sim \frac{c_0^2}{h_1 l_x}$. This scaling is shown from the collapse of the curves in Fig. 2.2 corresponding to different values of c_0, h_1 and l_x. This behavior remains valid in the range $60e_x \leqslant l_x \leqslant 90e_x$, $120e_x \leqslant h_1 \leqslant 160e_x$ and $400e_x \leqslant L \leqslant 1200e_x$. Using this scaling to normalize the axis in Fig. 2.2, different geometries lead to the same exponential regime in some limited range of crack lengths. In this range, the compliance can then be approximated by

$$\lambda_F \simeq \frac{1}{Eb} \beta \frac{c_0^2}{h_1 l_x} e^{c/c_0} \tag{2.2}$$

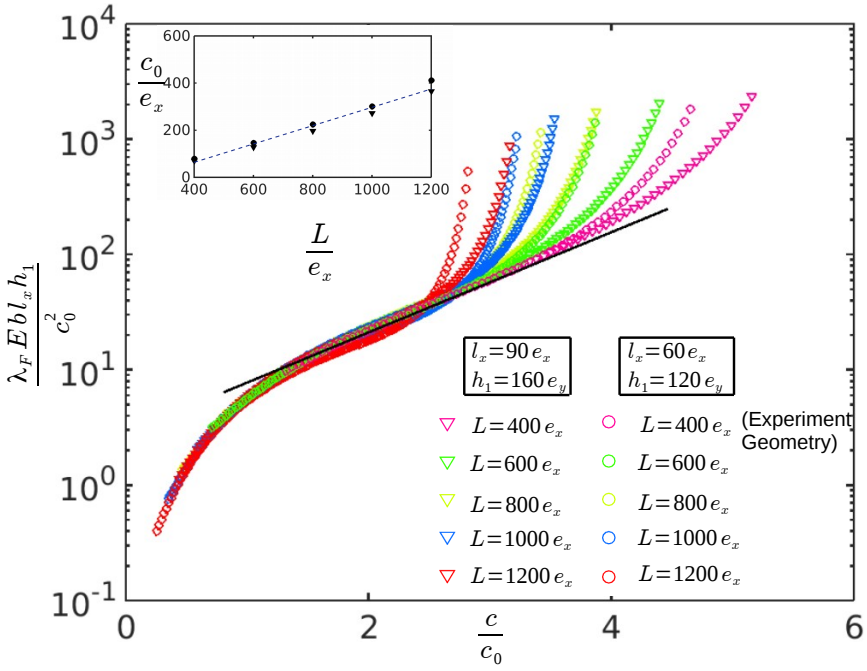

Fig. 2.2 *Variation of the non-dimensional specimen compliance with the non-dimensional crack length for different specimen length and geometry. The simulations are carried out for two different geometries with the same tapering angle α but with different values of l_x and h_1 (see Fig. 2.1(a)). The geometry # 1 is represented by triangles and has dimensions $l_x = 90e_x$ and $h_1 = 160e_y$ while geometry # 2 is represented by circles with dimensions $l_x = 60e_x$ and $h_1 = 120e_y$. The solid line shows the exponential fit of the collapsed curve and corresponds to Eq. (2.1)*

where $\beta \sim 3.0$ is constant obtained from the numerical fit. This is plotted in solid line in Figure 2.2. We can now predict the mechanical energy release rate G that will be subsequently used to analyze our experiments. G can be deduced from the compliance formula also referred to as the Irwin-Keis equation:

$$G = \frac{F^2}{2b}\frac{d\lambda_F}{dc} = F^2 g_F \tag{2.3}$$

where g_F that corresponds to the geometry dependent part of the elastic energy release rate is given by

$$g_F = \frac{1}{2b}\frac{d\lambda_F}{dc} \tag{2.4}$$

Substituting Eq. (2.1) in Eq. (2.4), one obtains its expression as a function of the geometry of the specimen:

$$g_F = \frac{\lambda_0}{2Eb^2c_0}e^{c/c_0} \tag{2.5}$$

Our motivation to define g_F is that it depends only on the specimen geometry and G can be decomposed into the product of the square of the applied force with this geometry

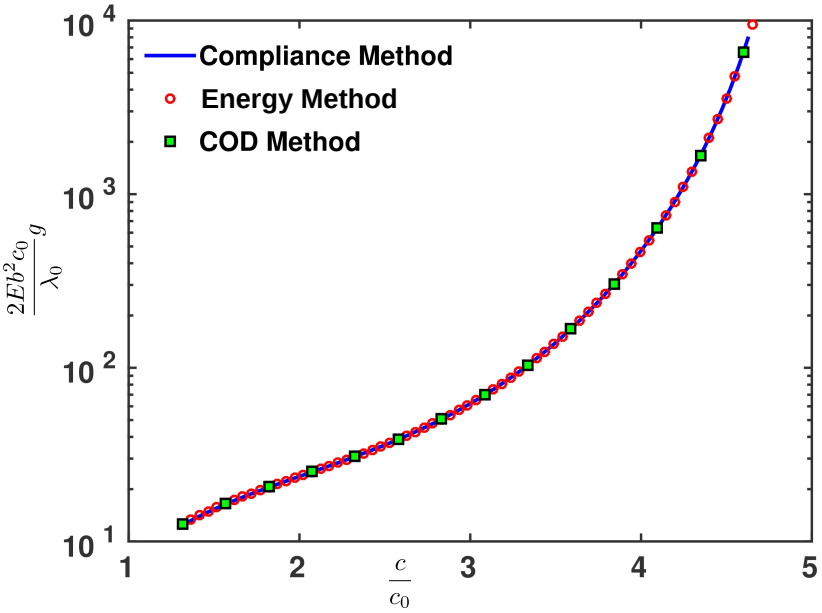

Fig. 2.3 *Variations of the non-dimensional elastic energy release rate g_F as a function of the crack length using different approaches. The figure is plotted for a specimen of dimensions $l_x = 90e_x$, $L = 400e_x$ and $h_1 = 160e_x$*

dependent function. As a result, for a unit force, we have $G = g_F$ that is the quantity measured in our simulations as a unit force is imposed. Taking inspiration from Eq. (2.5), we plot g_F on a semi-log scale as a function of $\frac{c}{c_0}$ after normalization by $\frac{\lambda_0}{2Eb^2c_0}$. The value of g_F is here obtained by three independent methods: (i) The first method consists in using Eq. (2.4) with the compliance method computed numerically using finite elements, (see Fig. 2.2) (ii) second method consists in calculating the variations of elastic energy stored in the specimen between two successive crack positions and deduce from it the rate of elastic energy released and (iii) the third method relies on the crack opening displacement (COD). From LEFM, we know that the crack opening profile follows $u(x) \sim K_I\sqrt{x}$, so the stress intensity factor is obtained by fitting the computed opening profile $u(x)$. This is done in a semi-log representation using a linear fit of slope 0.5. The energy release rate is then obtained from the Irwin's relation $G = K_I^2/E$. These methods are employed for different crack lengths and they give very similar results as shown in Fig. 2.3.

As the compliance is known, we can now go from force constant (dead-weight) loading used in the simulation to displacement constant (fixed-grips) loading used in the experiments. To convert the previous expression in to fixed grip loading, we then replace F in Eq. (2.3) by δ_F/λ_F where the compliance λ is given by Eq. (2.1) and the ratio $r = \frac{\lambda_F}{\lambda}$

$$G = \frac{\delta_F^2}{\lambda_F^2} g_F = \delta_F^2 \frac{Ee^{\frac{-c}{c_0}}}{2\lambda_0 c_0} = \delta_F^2 g \tag{2.6}$$

where g is the geometry dependent part of the compliance defined w.r.t displacement driven loading. From this equation we observe that G decreases exponentially with the

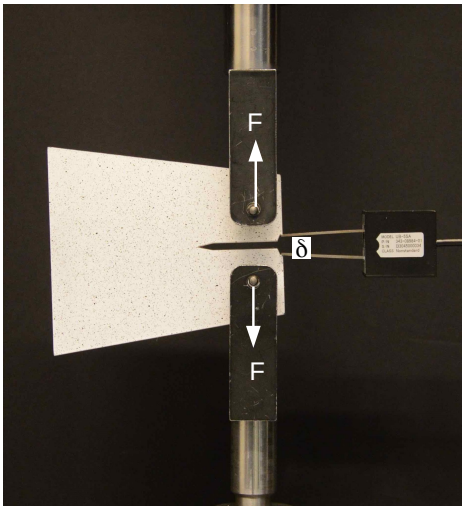

Fig. 2.4 *Setup of the experiment*

crack length, under fixed imposed displacement δ. This is a key property of the modified TDCB test that will allow us to explore different velocities and measure their corresponding fracture energy. For sake of comparison, let us now consider classical fracture tests like Double Cantilever Beam (DCB), Double Torsion and Compact Tension (CT). In DCB and classic TDCB, the compliance increases as the cube of crack length so from Eq. (2.6), the energy release rate decays as one over the fourth power of crack length [Sih, 1972]. For the Double Torsion (DT) test, the compliance varies linearly with crack length and the energy release rate varies inversely to the square of crack length. To have a stable and controlled crack growth, it is decisive that the energy release rate decreases as fast as possible with crack length. The exponential decrease achieved by the TDCB specimens is faster than the one obtained by traditional methods that displays only a polynomial decrease ensuring an extremely stable crack growth as illustrated in the following.

2.2 Experimental Results: Low crack velocities

Fig. 2.4 shows the TDCB specimen loaded on a Schimadzu (model AG-Xplus) universal testing machine of 10 kN maximum loading capacity. In this setup, we use a 1kN load cell to measure the force and a clip gauge to measure the displacement 2δ between the lips of the crack (see Fig. 2.1(a))). The tests are controlled by the clip gauge, *i.e.* the crack opening rate is set to $d\delta/dt = 2.5\ \mu m s^{-1}$. A typical force vs displacement curve is shown in Fig. 2.5.

2.2.1 Experimental validation of the compliance method

Before measuring the fracture properties of the material, we first test our approach by measuring the compliance as a function of crack length and by comparing it to the the one obtained from finite elements. Fig. 2.6 shows the comparison. The experimental compliance is obtained by unloading and reloading the sample for some fixed crack length that is measured independently through optical means. The slope of the force-displacement

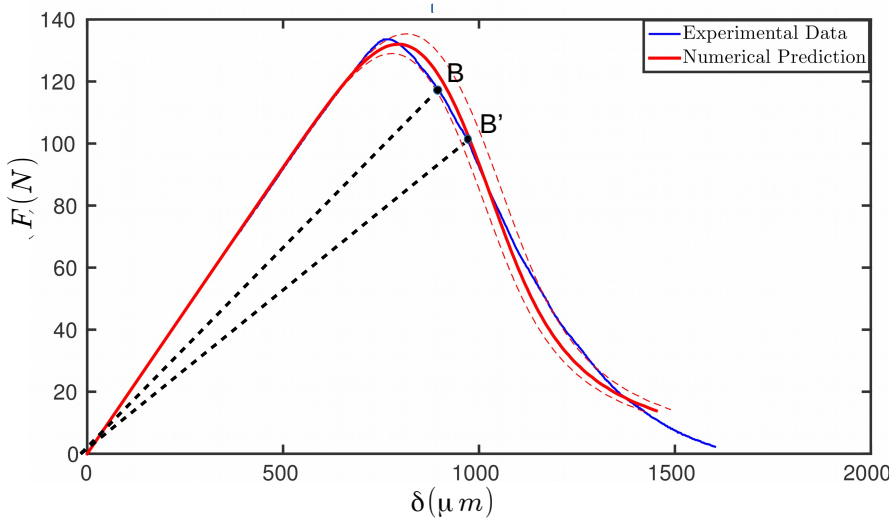

Fig. 2.5 *A typical force vs displacement curve obtained for a constant opening rate at* $2.5\mu m/s$.

provides the value of the compliance after each measurement, we propagate the crack over a small distance and reiterate the procedure again to measure the new compliance value. Fig. 2.6, shows that the experimental and the theoretical compliance agree very well.

2.2.2 Measurement of crack length and crack speed

To measure the crack length $c(t)$ as a function of time, we use the finite element calculations that provides the compliance $\lambda^{FE}(c)$ at the clip gauge location for different crack lengths. By comparison with the compliance obtained from the experiment, $\lambda(t) = \delta/F$ one infers the crack tip position $c(t)$. The crack length normalized w.r.t the length of the sample as a function of the imposed displacement, δ is plotted in Figure 2.7. Along with the use of the full FE result, we also plot the crack length predicted by the analytical formula of (Eq. (2.1)) and observe a good agreement till $\frac{c}{L} = 0.7$, which is due to the fact that the compliance is an exponential function of crack length only in a limited range, typically $(L/3 \lesssim c \lesssim 2L/3)$. The crack growth velocity is then calculated as $v(t) = \dfrac{dc}{dt}$ and is shown in Fig. 2.8(a). We observe a fairly constant crack speed in agreement with the finite element study that predicts very stable crack growth.

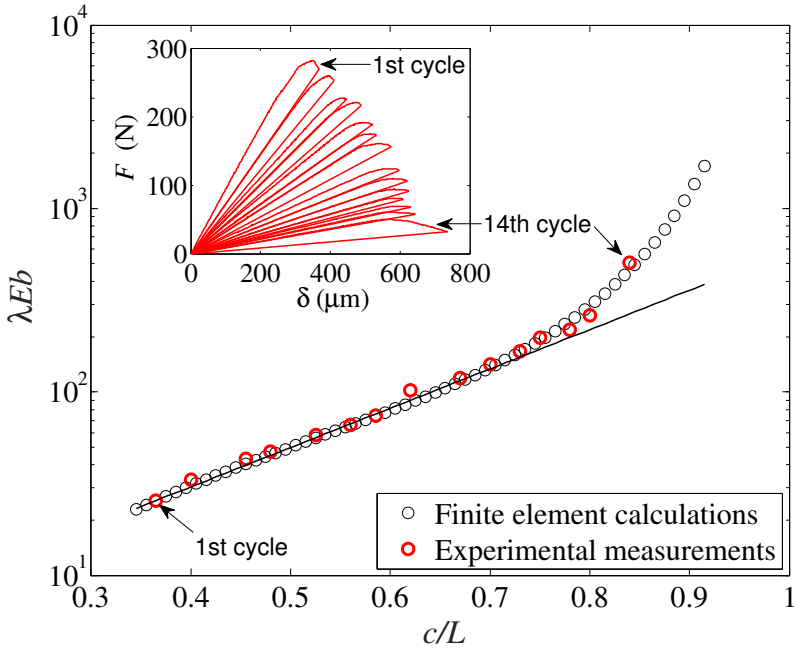

Fig. 2.6 *Normalized compliance as a function of normalized crack length. The black dots are finite element calculations while the red dots are experimental measurements. The inset shows the force-displacement response that includes 14 cycles of unloading-reloading used to measure the compliance.*

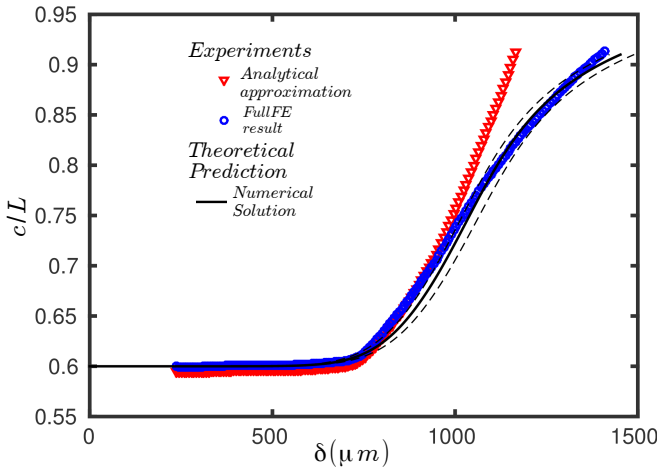

Fig. 2.7 *Calculation of the experimental crack length by two different methods.*

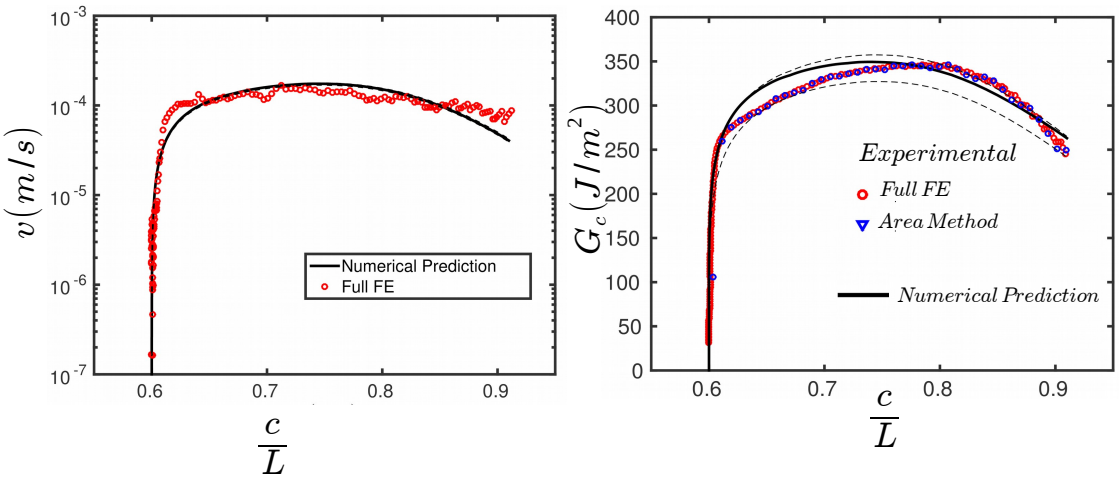

Fig. 2.8 *(a) Semi-log representation of the variations of the crack speed as a function of crack length where the results obtained from the compliance method (see section 2.2.2) are compared with the theoretically predicted behavior (See section 2.2.6) (b) Variation of the elastic energy release rate calculated from the compliance method (see section 2.2.3) and comparison with the theoretically predicted behavior (see section 2.2.6). The dotted lines corresponds to the errorbars in the numerical prediction represented on the $G_c - v$ curve (see Fig. 2.10)*

2.2.3 Measurement of the elastic energy release rate

Once we know the crack length, we then have two methods available to measure the elastic energy release rate, G. The first method relies on the estimation of the energy dissipated for an incremental crack advance using the force-displacement response. Assume that in B in Fig. 2.5 the crack length is c and after time $t + \Delta t$, it is $c + \Delta c$. The mechanical energy release rate is then given by the energy dissipated during this time divided by the area of the newly created fracture surface. The energy dissipated during this time interval Δt is equal to the area OBB'O (see Figure 2.5) and the newly created fracture surface area is Δcb where b is the width of the specimen [Morel et al., 2005]. Thus, $G(t)$ is given by

$$G(t) = \frac{E^d(t)}{\Delta c(t) b}$$

where $E^d(t)$ is the energy dissipated that correspond to the area OBB'O in Fig. 2.5 after replacing δ by δ_F using the ratio r. In the second method, we use direct finite element prediction of Eq. (2.6) derived in section 2.1.1. The energy release rate obtained by both these methods is shown in (Fig. 2.8(b)) and show very similar results. So from now on, Eq. (2.6) is used to measure the energy release rate G in our experiments.

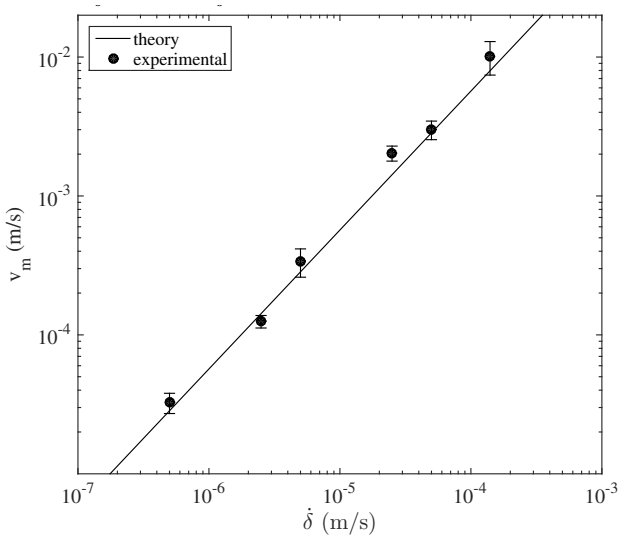

Fig. 2.9 *Log-log representation of the average crack velocity as a function of the imposed opening rate. The straight line corresponds to Eq.* (2.7)*, with the parameters set to* $c_0 = 21$ *mm* , $\lambda_0 = 4.81$, $Gc = 380$ Jm^{-2}, $E = 1.82$ GPa *and* $r = 0.8$.*The crack speed is measured for a crack length* $c \simeq 60$ mm

2.2.4 Prediction of the average crack speed

From the analytic formula presented in Eq.(2.2) of compliance one can estimate the average crack velocity v_{m} as a function of the imposed opening rate $\dot{\delta}$. As the velocity varies weakly during the test, (see Fig. 2.8(a)), we assume that the energy release rate does not vary too much. Taking a constant value $G = G_c$ in Eq. (2.6) and differentiating this equation w.r.t time, one can express the crack growth velocity

$$v_m = \sqrt{\frac{2Ec_0}{\lambda_0 r G_c}} e^{\frac{-c}{2c_0}} \dot{\delta} \tag{2.7}$$

as a function of the opening rate $\dot{\delta}$ where λ_0 and c_0 are the parameters obtained from the exponential fit of the compliance (see Eq 2.1).

Figure 2.9 shows in log-log scale the variations of the average crack speed as a function of the loading rate and the comparison with analytical results from Eq. (2.7) in the range $0.5\mu m s^{-1} \leq \dot{\delta} \leq 100\ \mu m/s$. The agreement is excellent proving therefore that the analytical formula can be used to choose the value of the opening rate in order to achieve some prescribed crack velocity.

2.2.5 Variation of fracture energy with crack speed

In polymeric materials like PMMA, slow crack propagation proceeds in two steps: the polymeric chains are first gradually elongated until full elongation and failure. This elongation phase is a rate-dependent process and so depends on the velocity at which the crack propagates. As a result, the fracture energy is also a function of the crack velocity. The so-called $G_c - v$ curve is a material property and in polymeric materials it can be

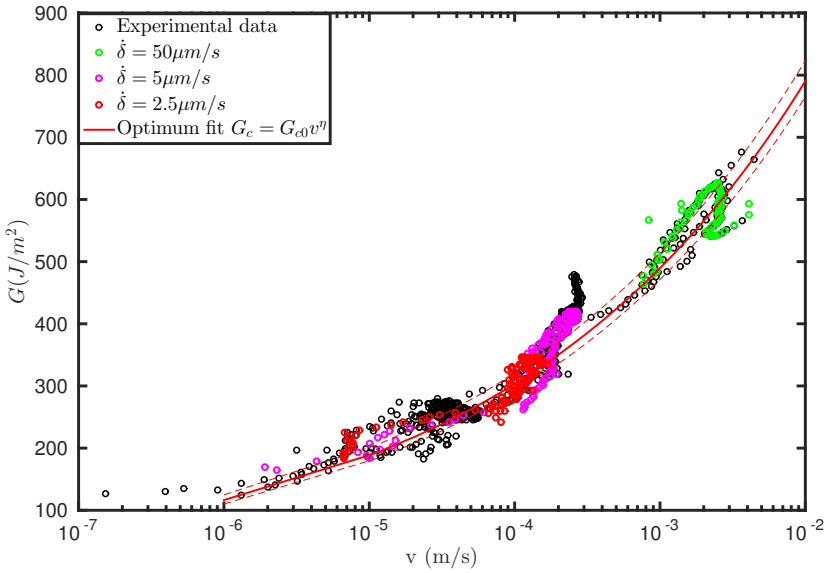

Fig. 2.10 *Diagram showing the variations of the fracture energy with crack speed, for slow crack propagation* $v_m < 5\text{mms}^{-1}$

described by a power law [Maugis and Barquins, 1978]. The $G_c - v$ curve obtained for PMMA from our experiments is shown in Fig. 2.10. Interestingly just few experiments are sufficient to capture the $G_c - v$ over a very large range of velocities. This can be obtained since one single test (for example see the test shown in green in Fig. 2.10 corresponding to $\dot{\delta} = 5\mu m s^{-1}$) explore a rather wide range of crack speed varying typically over a factor three.

2.2.6 Fit of $G_c(v)$

For polymers, the fracture energy strongly depends on crack speed [Maugis and Barquins, 1978] which is consistent with our experimental observations. To describe this variation, one can use a two parameter power law fit of the form

$$G_c(v) = G_{c0}v^{\gamma} \tag{2.8}$$

Determining the kinetic law has many interests as it allows to make predictions on the lifetime of a structure or it can be used to infer the microscopic failure mechanisms taking place at the crack tip vicinity within the process zone (e.g. stress corrosion). This kinetic law will also be used later for the study of the pinning of cracks by tough obstacles (see Chapter 3).

We now propose a methodology that allows for an improved determination of the material parameters involved in the kinetic law $G_c(v_m)$. For illustrating this method, we consider the kinetic law of Eq. (2.8), one can predict the $F - \delta$ response of the TDCB specimen under some given opening rate $\dot{\delta}$. This can be achieved from the variations of the compliance with crack length as predicted from finite elements. We start with the Griffith's criterion that reads as :

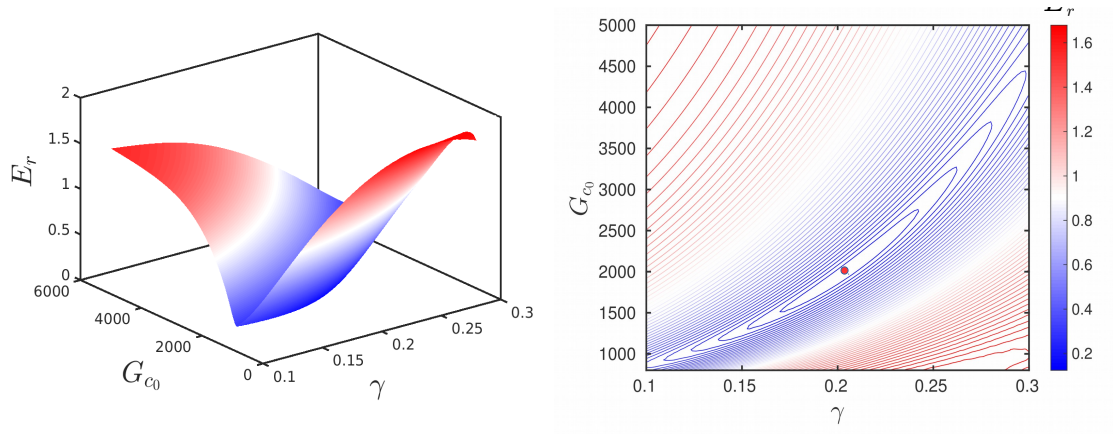

Fig. 2.11 *Error plot E_r as a function of the parameters G_c^0 and γ*

$$G = G_c(v) \Longrightarrow \delta(t)^2 \frac{1}{2b} \frac{1}{\lambda^{FE}(c)^2} \frac{d\lambda(c)^{FE}}{dc} = G_c(\dot{c}) \tag{2.9}$$

where $\delta(t) = \dot{\delta}t$.

Eq. (2.9) is a first order differential equation where the crack length c variations $c(t)$ is the unknown. This equation can be solved numerically, The force-displacement response can then be reconstructed using the parametric function $\delta(t) = \dot{\delta}t$ and $F = \dot{\delta}t/\lambda^{FE}(c(t))$ which can be compared with the experimental force-displacement curve as shown in Fig. 2.5. To precisely determine the material parameters of the kinetic law of Eq. 2.8 we then use an optimization procedure.

Two parameter optimization to obtain the kinetic law

We choose three well controlled experiments corresponding to three different loading rates to carry out the optimization (the three chosen experiments are marked in color in Fig. 2.10). The three experiments are chosen at different loading rates, as a larger region in the $G_c - v$ curve is covered and will lead to a more accurate estimation of these parameters. We systematically vary the parameters G_c^0 and γ and find the best pair of parameters which minimize the error between the numerically predicted $F - \delta$ curve (as illustrated in the previous section) and the experimentally measured $F - \delta$ for these three experiments. Thus for each of the experiments, we can define an error

$$\epsilon_r = \sqrt{\sum_{\delta_i} \left[\frac{F_{num}(\delta_i) - F_{exp}(\delta_i)}{F_p} \right]^2}$$

where F_p is the maximum value of the force used to normalize the error. The cumulative error then for the three experiments would be

$$E_r = \sqrt{\frac{\epsilon_1^2 + \epsilon_2^2 + \epsilon_3^2}{3}}$$

Figure 2.11 shows a map of the error E_r as a function of the parameters γ and G_c^0. The minimum of this map is found for $G_c^0 = 2000 \pm 100$ and $\gamma = 0.2 \pm 0.02$. The power found for our experiments compare well with the power found for various other polymeric materials [Maugis and Barquins, 1978]. A plot of the optimized fit is shown in red in Fig. 2.10 and the two dotted lines are the error in the estimation of these parameters. Once the kinetic law is known, we can predict all the fracture properties like $c(t)$, $v(c)$, $G(c)$, $F - \delta$ etc. The prediction of each of these properties are shows in solid line in Fig. 2.7 , 2.8 and 2.5 and they are in excellent agreement with the experimentally measured properties.

2.2.7 Conclusions drawn from low velocity experiments

In this first part, we have used experiments and finite element simulations to design a new fracture test geometry inspired from TDCB samples to study the fracture properties of PMMA.

- The tapered geometry provides stability to the crack, both in terms of trajectory and dynamics.
- For crack lengths between $\frac{L}{3}$ and $\frac{2L}{3}$, the compliance increases exponentially with crack length. This analytical fit reduces the necessity of using a full finite element calculation, providing a very useful analytical model to investigate the mechanical response of TDCB samples.
- The exponential increase in compliance with crack length for this geometry leads to an exponentially decreasing elastic energy release rate at constant displacement δ. This strong decrease is a hallmark of a stable test.
- A two-parameter optimization of the comparison between the predicted and the experimental force-displacement response provided a good way to measure the kinetic law of brittle solids. The exponent of the power law characterizing $G_c(v)$ in PMMA is found to be $\gamma \sim 0.2$.
- Finally, removing the narrow edges of the traditional TDCB, this modified geometry is easier to machine, especially for materials like rocks, mortar, ceramics etc.

2.3 Experimental study of the slip to stick transition

In this section, we explore the dynamics of fast cracks in PMMA using the experimental setup designed previously. Some materials under the application of a constant extension rate show stick-slip behavior: despite driving the crack at a constant rate, its speed oscillates between fast and slow. This has been observed in different materials such as PMMA [Ravi-Chandar and Balzano, 1988], thermosetting polymers [Leevers, 1986], epoxy resins [Yamini and Young, 1979], rubber [Isherwood and Williams, 1978] as well as during peeling of polymeric adhesives [Dalbe et al., 2015a, Maugis and Barquins, 1988]. The main cause for stick-slip behavior is the non-monotonous variation of the fracture energy with velocity. A typical variation of fracture energy with velocity for materials with stick-slip behavior shows three different regions (see Figure 2.12). First, at low velocities,

there is a stable branch where the fracture energy increases with the velocity (region I) . Another monotonously increasing stable branch is also observed at high velocity (region III). However, between these two branches, there is supposedly another branch with a negative slope that renders crack propagation unstable: if the crack is driven in this region, it begins to oscillate between the large speed and the low speed regions of the $G_c - v$ diagram (the crack jumps from BC to DA as shown in Fig. 2.12).

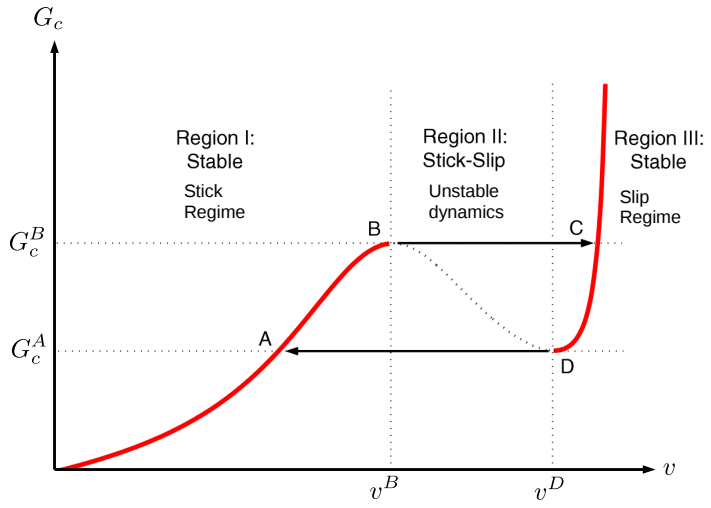

Fig. 2.12 *Kinetic law $G_c(v)$ for materials showing stick-slip behavior [Cortet et al., 2007]. G_c is the fracture energy and v is the velocity of the crack. If the crack is driven in region II, it oscillates between region I and III and exhibits stick-slip behavior.*

In our experiments, the notch is blunted with a circular hole so that we can impose a large driving force at initiation. This makes the crack start directly from the dynamic branch (region 3). The tapered shape of our sample imposes the crack to slow down so that it reaches the slow quasi-static region I after a rather short propagation distance typically ~ 2.5 cm. Thus one can study the transition from the slip (branch III) regime to the stick (branch I). To follow crack evolution, we use a fast camera (Photron SA5 color) at about 48000 fps while we record the force and the displacement using the load cell and the clip gauge. The fast camera is manipulated by an automatic trigger which starts once the crack begins to propagate. At high velocities, our load cell and clip gauge are not capable to record the force and the displacement with a sufficient accuracy. However, once the velocities decreases below 1 ms^{-1}, we can record precisely the force and the displacement. A typical $F - \delta$ curve for a fast to slow crack transition is shown in Fig. 2.13.

2.3.1 Crack dynamics during the slip to stick transition

As PMMA is transparent, the images recorded by the fast camera can be treated with a home made program to extract the position of the crack tip as a function of time. The images captured by the fast camera are shown in Fig. 2.14.

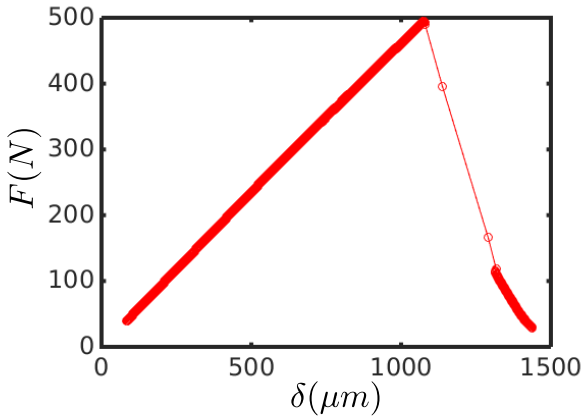

Fig. 2.13 *The force vs displacement response for a typical experiment where the crack goes from very fast speed* $v \simeq 200\text{ms}^{-1}$ *close to initiation to very slow* $v \simeq 0.1\text{mms}^{-1}$

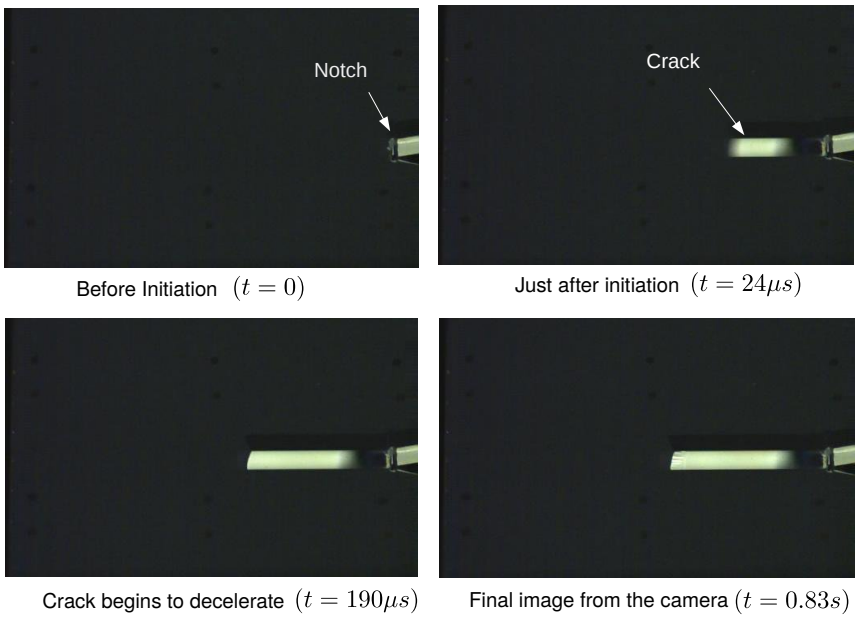

Fig. 2.14 *Images from the fast camera showing the slip to stick transition*

Figure 2.15 shows the crack front position, $\delta c = c(t) - c_{ini}$, where c_{ini} is the initial crack length as a function of time and the velocity as a function of crack length as obtained from the fast camera. The initial velocity of the crack are of the order of $\sim 100 - 200ms^{-1}$ and despite on high acquisition rate, we obtain only about eight images in the fast regime. However we are more interested in the transition from fast to slow which takes place in the range $\sim$ 1 $\text{ms}^{-1} \geq v_m \geq\sim$ 1 mms^{-1} where we have a lot of

data points. The velocities in the slip regime are typically 0.2 to 0.3 times the Rayleigh wave speed ($v_R = 880ms^{-1}$), which are too small to show any kind of dynamic fracture instabilities like microbranching[Boué et al., 2015, Ravi-Chandar and Knauss, 1984] or even microcrack formation [Guerra et al., 2012, Ravi-Chandar and Yang, 1997] on the fracture surface.

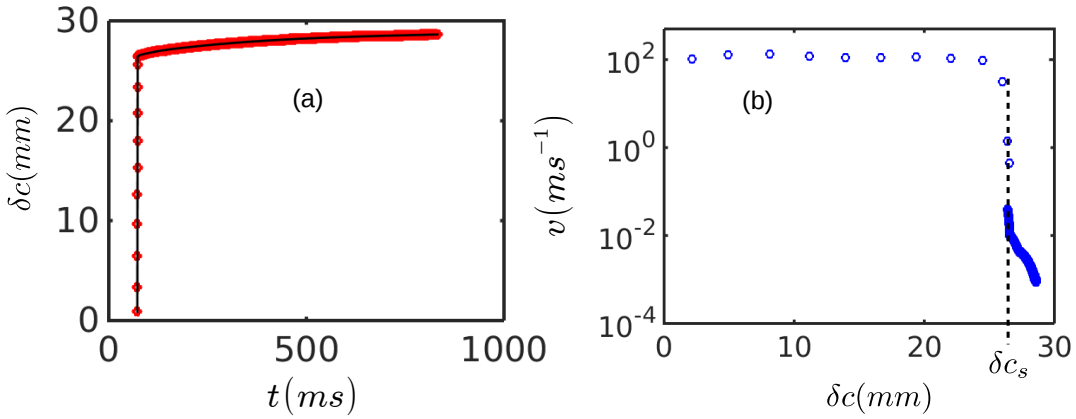

Fig. 2.15 *Experimental measurement of (a) crack length $\delta c = c - c_{ini}$ where c_{ini} is the notch length as a function of time and (b) velocity as a function of crack length*

2.3.2 Fracture energy vs crack speed during the transition

To calculate the fracture energy of the crack, we use the expression of the elastic energy release rate derived in Eq. (2.3) from the Irwin-Keis equation. However, we correct it by a term $1 - \frac{v_m}{v_R}$ taking into account the inertial effect [Freund, 1990] :

$$G^d = G_c = \delta^2 g(c_{cam}) \left(1 - \frac{dc_{cam}}{dt}\frac{1}{v_R}\right) \tag{2.10}$$

As we measure the crack length as a function of time from the fast camera, and the displacement from the clip gauge one can then calculate the fracture energy using the above formula. The obtained $G_c(v)$ curve is shown in Fig. 2.16 for different experiments with different initial conditions G_{ini}. Here the initial elastic energy release rate G_{ini} is computed at the onset of propagation through

$$G_{ini} = \delta_{ini}^2 g(c_{ini}) \left(1 - \frac{v_{ini}}{v_R}\right)$$

where δ_{ini} is the displacement measured by the clip gauge, just when the crack starts to propagate. The initial elastic energy rate being higher than the peak of the low velocity branch I, the crack starts directly from the the fast velocity branch III (see Fig. 2.12). At high velocities, we do not have accurate measurements of the force nor the displacement. However the loading rate imposed by the machine is so slow that we assume $\delta = \delta_{ini}$ for the first few μs where the speed is larger than 100ms^{-1}. Thus, the driving force in this

regime follows $G = \delta_{ini}^2 g(c_{cam}) \left(1 - \frac{v}{v_R}\right)$. These values correspond to the few points on the extreme right of Fig. 2.16. When the crack decelerates below 1ms^{-1}, we can use the recorded value of the displacement that we plug in Eq. (2.10). As the crack propagates, the geometrical part of $g(c) \sim e^{-c/c_0}$ of the elastic energy release rate decreases but the value of δ increases. Both effects compensate so that G remains almost constant while the crack is decelerating. Finally once the crack reaches very low velocities, it catches the low velocity branch I and typically for $v_m \sim 1\text{mms}^{-1}$, we recover the behavior observed for slow cracks as described in the previous section.

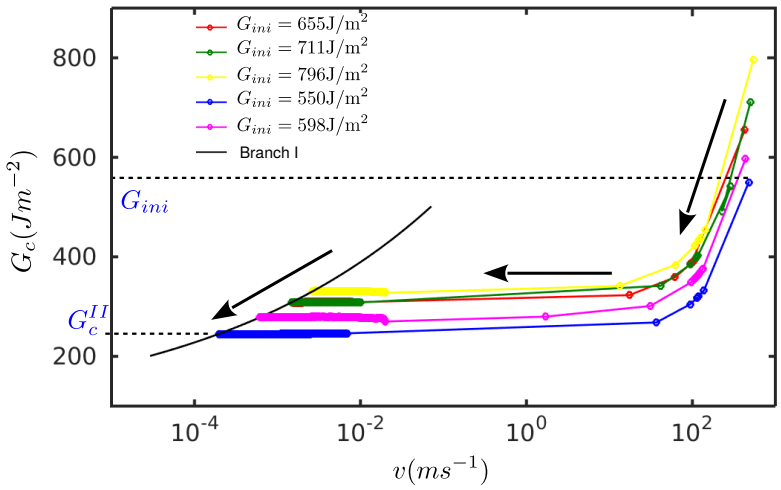

Fig. 2.16 *Fracture energy vs velocity for a decelerating crack for different initial elastic energy release rates G_{ini}. The black curve is the $(G_c - v_m)$ curve in the stick regime at low velocities as measured in Section 2.2.5*

2.3.3 Deceleration dynamics of the crack

In order to decipher the fracture patterns observed in the transition region between the slip and the stick regime, we explore in detail the deceleration dynamics of the crack. Let us first define c_{ini} to be the initial crack length and δc the distance propagated by the crack after initiation so that at any instant of time we can write $c(t) = c_{ini} + \delta c(t)$. Let us also define G_c^{II} as the fracture energy of the crack in the plateau region evidenced in Fig. 2.16. This value is observed when the crack transits from the slip to the stick branch. Let δc_s be the distance propagated by the crack in the slip phase that we define as the crack length corresponding to $v_m = 1\text{ms}^{-1}$. As seen in Fig. 2.15 (b), this coincides with the very sudden crack deceleration. On the fracture surface, this corresponds to the zone right before the triangular patterns. The larger the initial elastic energy release rate, G_{ini}, larger is the initial velocity and larger is the distance δc_s propagated by the crack in the slip phase. However, if one represents the crack speed variations as a function of $\delta c - \delta c_s$, the curves corresponding to different G_{ini} collapse to a single master curve showing a common deceleration dynamics from the slip to stick transition.

To understand quantitatively the dynamics during the slip to stick transition, let us

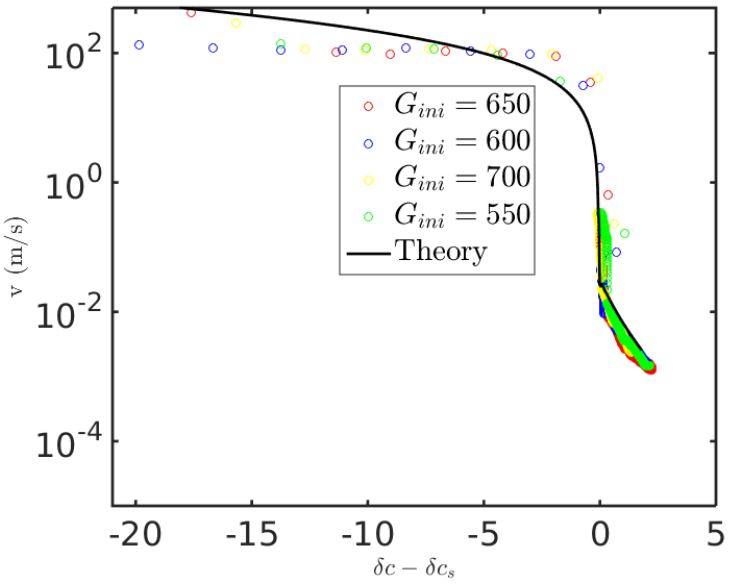

Fig. 2.17 *Once normalized by the distance δc_s crossed by the crack in the slip regime, the crack follows the same deceleration dynamics irrespective of the initial loading G_{ini}.*

first look at the measurement of the clip gauge, δ, as a function of time. This is shown in Fig. 2.18. We can decompose the entire experiment into different phases based on the measurement made by the clip gauge.

- Phase 0 : [$v_m = 0$ and $\delta = \dot{\delta} t$] - Before crack initiation, the displacement increases linearly at a prescribed rate $\dot{\delta}$ (red regime in Fig. 2.18).
- Phase 1: [200 ms^{-1} $< v_m <$ 100 ms^{-1} and $\delta = \delta_{ini}$] - After initiation, during a small interval, δt_{ini}, there is no change in the displacement that remains constant at $\delta = \delta_{ini}$. Typically, this phase corresponds to velocities 200 ms^{-1} $< v_m <$ 100 ms^{-1} and the value $\delta = \delta_{ini}$ was used to calculate the fracture energy in the slip phase (see section 2.3.2).
- Phase 2 : 100 ms^{-1} $< v_m <$ 50 ms^{-1} and δ varies] - In the range 100 ms^{-1} $< v_m <$ 50 ms^{-1}, the clip gauge follows the lips of the crack, but the crack opening is too fast. As a result we see a jump from $\delta = \delta_{ini}$ to $\delta = \delta_t$ (shown in blue color in Fig. 2.18).
- Phase 3: [50 ms^{-1} $< v_m <$ 1 cms^{-1} and $\delta = \delta_t$] - As the imposed opening rate is very small, the displacement during the deceleration does not change much and we can assume that it stays constant at $\delta = \delta_t$ (see inset in Fig. 2.18). The typical velocities of the crack in this phase are 50 ms^{-1} $< v_m <$ 1 cms^{-1}. Most of the deceleration and the triangular patterns appear in this phase (shown in green color in inset of Fig. 2.18).
- Phase 4 : [$v_m <$ 1 cms^{-1} and $\delta \sim \delta(t)$ t] - Below $v_m \simeq$ 1cms^{-1}, the displacement again increases at a rate imposed by the machine.

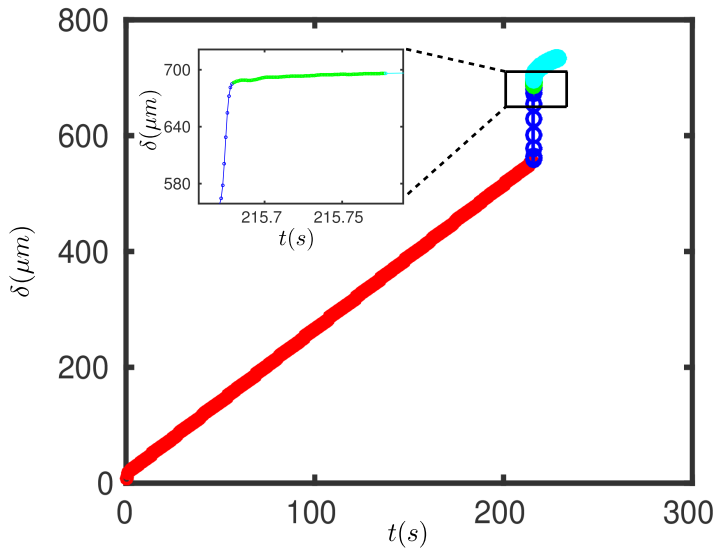

Fig. 2.18 *Displacement measured by the clip gauge as a function of time in different phases. Red: Phase 0- displacement imposed by the machine before crack initiation, $v_m = 0$ and $\delta = \dot{\delta}$; Phase 1 (not shown in figure)- Immediately after initiation, $\delta = \delta_{ini}$ at $200\text{ms}^{-1} < v_m < 100\text{ms}^{-1}$; Blue - Phase 2: Increase in the displacement between $100\text{ms}^{-1} < v_m < 50\text{ms}^{-1}$; Green: Phase 3 - Crack decelerates from to 50ms^{-1} to 1cms^{-1} under constant displacement $\delta = \delta_t$; Cyan: Phase 4 - For $v_m < 1\text{cms}^{-1}$, crack again propagates by the displacement imposed by the machine.*

We now explore in detail the crack deceleration dynamics in Phase 3 as the triangular patterns are formed during this phase. In this phase, we assume $\delta = \delta_t$ where δ_t is measured from the green plateau in inset of Fig. 2.18. To understand the deceleration dynamics, one writes the equation of motion derived from energy balance as [Freund, 1990]:

$$G^{QS}(c)\left(1 - \frac{\dot{c}}{v_R}\right) = G_c(\dot{c})$$

where the elastic energy release rate is corrected by the term $1-\dot{c}/v_r$ that describes energy consumed into kinetic energy and G^{QS} is the energy release rate for a crack propagating quasi-statically. This equation of motion has been shown to predict very well the dynamics of a fast crack till $0.4v_R$ in PMMA [Sharon and Fineberg, 1999] and till $0.96v_R$[Goldman et al., 2010] in brittle gels.

To describe the variations of fracture energy with crack speeds, we use a fit proposed by Scheibert et al. [2010] for PMMA given by :

$$G_c(\dot{c}) = G_c^{II}\left(1 + \frac{2\alpha}{v_R}\dot{c}\right)$$

where α is a fitting parameter that is found to be 1.15 in our experiments, v_R is the Rayleigh wave speed and $\overline{G_c^{II}}$ is the fracture energy in the plateau regime of Fig. 2.16.

The elastic energy release rate follows:

$$G(c) = \delta_t^2 g_\delta(c)$$

The equation of motion then writes as :

$$\delta_t^2 g_\delta(c) \left(1 - \frac{\dot{c}}{v_R}\right) = G_c^{II} \left(1 + \frac{2\alpha}{v_R}\dot{c}\right)$$

For the TDCB geometry, the elastic energy release rate follows (see Eq. (2.6)):

$$g_\delta(c) = \frac{Er^2}{2\lambda_0 c_0} e^{-\frac{c}{c_0}}$$

where λ_0 and c_0 are parameters obtained from the fit of the FE results and E is the Young's modulus of the material. Using this relation the equation of motion writes as:

$$\delta_t^2 \frac{Er^2}{2\lambda_0 c_0} e^{-\frac{c(t)}{c_0}} \left(1 - \frac{\dot{c}}{v_R}\right) = G_c^{II} \left(1 + \frac{2\alpha}{v_R}\dot{c}\right) \tag{2.11}$$

At the velocities $\dot{c} \sim \text{cms}^{-1}$, the terms $\dot{c}/v_R \ll 1$. In addition, the crack length in the transition region is about $c = c_{ini} + \delta c_s$. This allows us to relate δ_t and G_c^{II} through

$$\delta_t^2 \frac{Er^2}{2\lambda_0 c_0} e^{-\frac{c_{ini}+\delta c_s}{c_0}} = G_c^{II} \tag{2.12}$$

Substituting Eq. (2.12) in Eq. (2.11), and writing $c(t) = c_{ini} + \delta c$ the equation of motion becomes independent of G_c^{II} or δ_t and finally writes as :

$$e^{\frac{\delta c_s - \delta c}{c_0}} \left(1 - \frac{\dot{\delta c}}{v_r}\right) = 1 + \frac{2\alpha}{v_R}\dot{\delta c}$$

This equation can be solved analytically to give,

$$c(t) = c_{ini} + \delta c_s + c_0 \log\left(1 - e^{\frac{-t}{\tau}}\right) \tag{2.13}$$

where $\tau = \frac{2\alpha c_0}{v_R}$. The velocity of the crack as a function of its position is obtained as :

$$v(c) = \frac{c_0}{\tau}(e^{\frac{\delta c_s - \delta c}{c_0}} - 1)$$

As $t \to \infty$, $c = c_{ini} + \delta c_s$, the crack comes to a stop as the displacement is kept constant at δ_t. As in Phase 4, the displacement increases beyond δ_t, we can provide $\delta = \delta(t)$ in Eq. (2.11), to capture the crack evolution beyond $c = c_{ini} + \delta c_s$ which is done numerically. The comparison of the $v - c$ curve (solid line) by our model and its comparison with the experimental curve is shown in Fig. 2.17. Upto the value $\delta c - \delta c_s = 0$, we use the analytical solution and for $\delta c - \delta c_s > 0$ (phase 4), we use the numerical solution. The analytical solution provides us a characteristic time scale $\tau = \frac{2\alpha c_0}{v_R}$ of the deceleration process that also corresponds to the duration of the transition from slip to stick. For PMMA, $v_R = 880\text{ms}^{-1}$ and for our TDCB geometry, $c_0 = 21.4$ mm and $\alpha = 1.15$ obtained from the fit of $G_c(v_m)$ one finds $\tau = 56\mu s$, thus giving characteristic deceleration of the order $\frac{\Delta v}{\tau} \sim 10^6$ ms^{-2} ! During the transition from slip to stick, the crack undergoes a tremendous deceleration.

Variation of G_c^{II} with G_{ini}

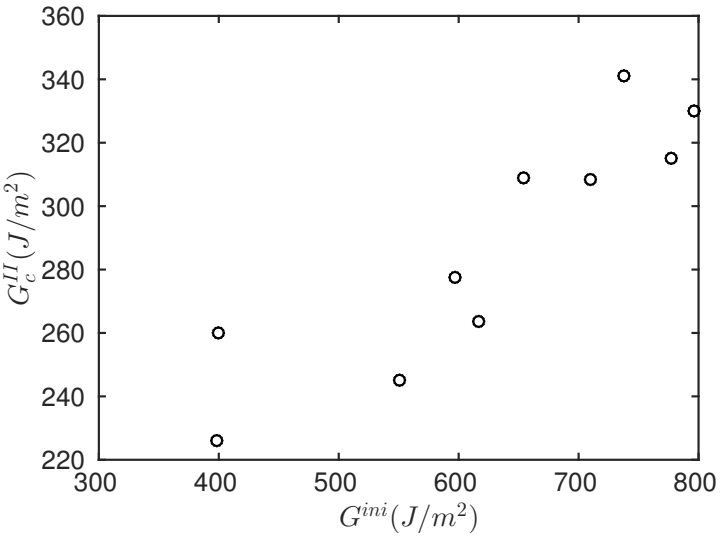

Fig. 2.19 *Variation of G_c^{II} as a function of G_{ini}*

During the transition from slip to stick, the fracture energy remains almost constant (see Fig. 2.16). However, for different initial loading conditions, the horizontal plateau defined by G_c^{II} shows slight variations. Figure 2.19 shows the fracture energy at transition, G_c^{II} as a function of the initial elastic energy release rate G_{ini} and larger G_{ini} results in a larger G_c^{II}. Cracks are normally history independent, and hence for a given velocity they generally exhibit the same fracture energy irrespective of the initial conditions and this correlation is rather surprising.

In the previous section, we were able to predict analytically the crack front evolution during the deceleration phase. As a result, one can use our model to predict the elastic energy release rate

$$G(c) = \delta_t^2 \frac{Er^2}{2\lambda_0 c_0} e^{-\frac{c(t)}{c_0}}$$

Substituting the analytical solution for $c(t)$ from Eq. (2.13) and using the relation between δ_t and G_c^{II} in Eq. (2.12), the elastic energy release rate writes as

$$G(t) = \frac{G_c^{II}}{1 - e^{-t/\tau}}$$

where $\tau = \frac{2\alpha c_0}{v_R}$. Derivating once, the rate of change of elastic energy release rate gives

$$\dot{G}(t) = \frac{-G_c^{II}}{\tau} \frac{e^{-\frac{t}{\tau}}}{(1 - e^{-\frac{t}{\tau}})^2}$$

The decrease of the elastic energy release with time takes a simple form: It is characterized once again by the same time scale $\tau = \frac{2\alpha c_0}{v_R}$ and G_c^{II} provides a measurement of its

amplitude. In principle, G_c^{II} should have been a material constant and so the elastic energy release rate evolution should have been the same for all our experiments, irrespective of the initial condition G_{ini}. However we do observe variations in the experimental value of G_c^{II} (see Fig. 2.19). This means that (i) G_c^{II} is not a function of the instantaneous crack speed only and may depend on the past evolution of the crack. (ii) that the rate $|\dot{G}|$ that increases when G_c^{II} increases varies from one experiment to another. It is larger when G_c^{II} is larger and so when G_{ini} is larger. Overall, our findings indicate that the fracture energy G_c^{II} characterizing the slip to stick transition does vary with $|\dot{G}|$ (the larger $|\dot{G}|$, the larger G_c^{II}). This is an indication that the plateau regime measured in the $G_c(v_m)$ diagram do not correspond to a stationary point (contrary to branches I and III). But instead, it describes a transient state between both stationary points characterized by a toughness that may depend on the initial condition, the variation rate of G, etc.

2.3.4 Crack velocity during the formation of the triangular patterns

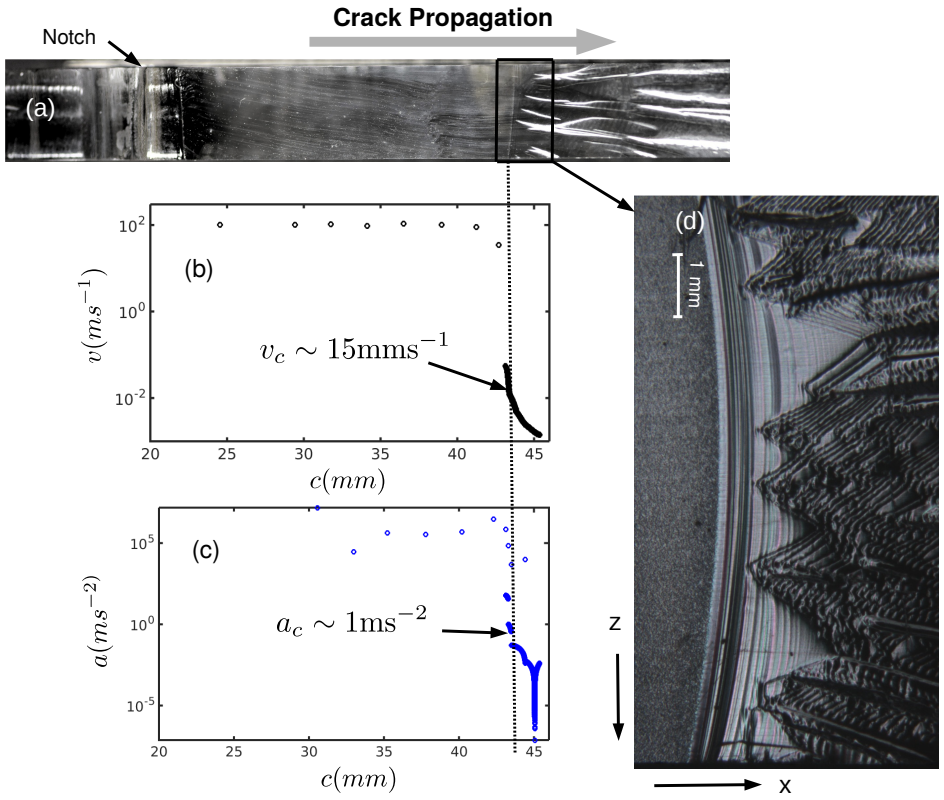

Fig. 2.20 *Fracture surface of PMMA at slip to stick transition: (a) Crack begins at the notch and undergoes one slip to stick transition.(b) velocity as a function of crack length, triangles are formed at* $v_c \sim 15\text{mms}^{-1}$. *(c) Absolute value of deceleration as a function of crack length, at triangles, decelerations are much lower* $a_c \sim 1\text{ms}^{-2}$ *to maximum of* 10^6ms^{-2} *(d) Fracture pattern at the slip to stick transition*

So far, we looked at the dynamics of the crack during the fracture test. In this section, we compare this dynamics with the post-mortem fracture patterns observed near the slip-stick transition. Figure 2.20 shows a fracture surface of a TDCB sample of PMMA. The corresponding variations of the velocity and acceleration are also provided as a function of crack length. At fast crack propagation, the fracture surface is optically smooth (see Fig. 2.20(a)) while at low velocities, the fracture surface is rough. At the transition, the crack fragments forming triangular patterns on the surface (Fig. 2.20(d)). The crack initiates at velocities close to $v_m = 200$ ms^{-1} and slows down to velocites of $v_m = 1$mms^{-1} undergoing a tremendous deceleration. Just before the formation of the triangles, the crack speed changes from $v_m \sim 50$ms^{-1} to $v_m \sim 1$cms^{-1} in a few μs, showing a peak deceleration of $a \sim 10^6$ms^{-2} (see Fig. 2.20(c)). At the same time, parabolic lines are seen on the fracture surface (see 2.20 (d)) which resemble to the Wallner lines let on fracture surfaces when a moving crack encounters a shear wave [Bonamy and Ravi-Chandar, 2003, Wallner, 1939]. In our experiments, these markings occur multiple times and show a spacing which decreases with crack length (See Fig. 2.21). The characteristic distance between two successive lines is $\delta c_w \sim 50\mu m$ and the typical crack speed in this region is $v_m \sim 1$cms^{-1}. Thus the frequency of these markings is $\nu = v_m/\delta c_w \sim 200Hz$. If we assume that between two successive markings, a shear wave travels and reflects from one of the boundaries of the sample before interacting with the moving crack, one obtains a frequency, $\nu = c_s/d$, where d is the distance traveled by the wave and c_s is the shear wave speed in the material. Taking $d = 100$mm, i.e. assuming that the shear waves are reflected from the top of the sample, and $c_s = 1000$ms^{-1} for PMMA, we obtain $\nu = 10^4 Hz$ which is two orders of magnitudes larger than the value extracted from the fracture surface. Thus these markings may not be set by a single shear wave. An alternative could be that the strong deceleration of the crack results in a train of waves or that it excites a vibrational mode of the TDCB specimen at the frequency $\nu \simeq 100Hz$. Further investigations would be required to test these scenario and eventually explain these marks.

Using the crack length measured with the fast camera, one obtains the velocity at which the crack start to form the triangular patterns. We determine the critical velocity $v_c \sim 15$mms^{-1}, with an error bar $\delta v = 5$mms^{-1} below which the fracture surface roughens. The crack has already decelerated so that at the position of the triangles, one typically gets $a_c \sim 1$ms^{-2}. Thus PMMA displays a transition from smooth to rough below a certain crack speed. To understand this transition is the main goal of this thesis.

We observe that these triangles show step like features inside the triangle which look similar to other fragmentation patterns (Baumberger et al. [2008], Lin et al. [2010], Sommer [1969]). Is there a connection between the crack front fragmentation under mode I + III and the triangular patterns? If so, what triggers this transition? We also observe from the fracture surface that the crack front (seen through Wallner lines on the fracture surface) is lagging inside the triangle indicating that they may correspond to regions of higher toughness. These patterns when observed through a profilometer also show a bump (See Fig. 5.4, discussed in detail later). To decipher these puzzling observations, in the next chapter we look at the pinning of a crack front by a triangular obstacle under small imposed mode II and mode III loading conditions. The predicted fracture patterns are then compared with experimental observations in the final Chapter 5.

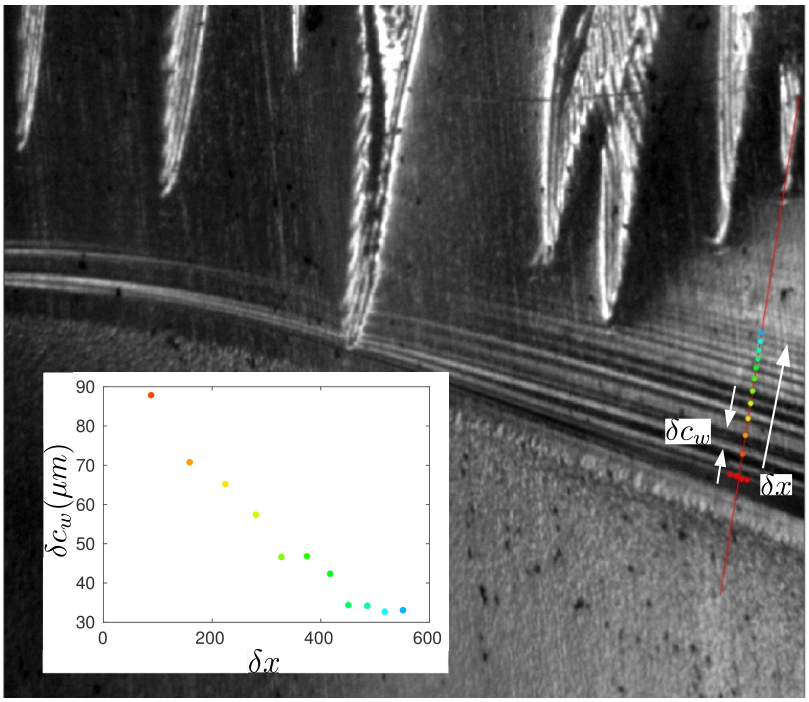

Fig. 2.21 *Wallner line spacing (δc_w)as a function of the distance δx to Wallner line. The spacing is calculated normal to the crack front.*

Chapter 3

Crack front pinned by an obstacle and subjected to mode I + II + III

Contents

The basic foundations of fracture mechanics was set up in 1921 by Griffith [Griffith, 1921] based on an energetic criterion: crack propagation occurs if the mechanical energy released that flows to the crack tip is able to overcome the fracture energy required to propagate the crack over a unit surface. The so-called Griffith criterion translates into

$$\begin{cases} G(c) < G_c \longrightarrow \text{no crack advance} \\ G(c) = G_c \longrightarrow \text{crack propagation} \end{cases}$$

where G is rate of mechanical energy release rate that acts as a driving force for crack propagation and G_c, the fracture energy that is an intrinsic property of the material.

For a homogeneous material this law is clear. However in the presence of heterogeneities in the material, the situation becomes more complex. One may introduce the effective fracture energy of the material that reflects the macroscopic resistance of the material at the macro-scale, and its relation to micro-structural features of materials is not well understood yet. Computing the front geometry is very important for predicting the effective fracture energy [Ponson, 2017] as the crack front by deforming selects the local fracture properties at the small scale that contributes to the effective fracture energy at the large scale.

In the context of our work, at the slip to stick transition, cracks in PMMA fragment to leave triangular fracture patterns on the fracture surface. The crack front shape seen through an optical microscope through the Wallner lines shows a pinned shape at the triangle (see Fig. 5.2) suggesting that these triangles are regions of higher toughness. To understand the shape of the crack front pinned by a triangle, in this chapter we address the problem of a crack encountering a triangular obstacle of higher toughness. The predicted shape allows us to make a comparison with the experiments in Chapter 5 to extract an effective toughness contrast due to the triangles. Moreover, in addition to this primary motivation, the prediction of the shape of crack fronts pinned by a tough obstacle is relevant in the context of the study of fracture of heterogeneous brittle solids to measure the effective fracture energy of the crack.

Further, when scanned by a profilometer, the triangular patterns exhibit out-of-plane features (see Fig. 5.4). The patterns grows out-of-plane non-uniformly with the region inside the triangle deviating larger. To understand this behavior, we apply a small amount of mode II and mode III to the crack perturbed by the triangular obstacle and calculate the out-of-plane deviations. This prediction is then finally compared to the experimental shape of the triangle in Chapter 5. This chapter thus focuses on studying two important problems : the pinning of a crack by a triangular obstacle and the out-of-plane deviations of this pinned crack under a small amount of mode II and mode III. The theoretical predictions are then compared to the experimental shape of the triangles in Chapter 5.

3.1 Evolution equation of a planar crack

To solve the problem of a crack front pinned by an obstacle, we first derive the evolution equation of the crack front following the works of [Chopin et al., 2011],[Vasoya et al., 2013],[Dalmas et al., 2009] etc. For now we assume that the propagation of the crack is planar under pure mode I and propagates under imposed displacement. We also assume that (i) all the characteristic scales of the sample (length, width, crack length etc.) are much larger than the size of the heterogeneities and (ii) that the dissipation failure processes (like plasticity, microcracking, bond breaking etc.) happens in a small zone referred to as the process zone whose size is much smaller than the characteristic size of the heterogeneity ($l_{pz} \ll d$). Under these assumptions, one can reduce the corresponding 3D fracture mechanics problem to a 2D problem where an elastic interface (the crack front) is driven through a heterogeneous field of toughness [Gao and Rice, 1989, Ponson and Bonamy, 2010, Schmittbuhl et al., 1995]. Its three main ingredients are :

- *Driving force of the crack:* In a perturbed configuration, the driving force is not uniform. In the limit of small geometric perturbations, a perturbation analysis

allows to express the driving force of the crack $G(z,t)$ along the front as a function of the crack front configuration $f(z,t)$

- *Fracture Energy:* : The fracture energy is assumed to be constant inside and outside the obstacle, defining the toughness contrast, $C = \frac{G_c^O - G_c^M}{G_c^M}$ where G_c^O is the fracture energy of the obstacle and G_c^M is the fracture energy outside the obstacle. As a result, the toughness along the front follows a step function.
- *Kinetic law:* The local crack speed is inferred from a kinetic law in which the velocity of the crack is linearly proportional to the net driving force $\frac{\partial c}{\partial t} \sim G(z,t) - G_c(z,t)$.

The explicit expression of each contribution is now provided in the following sections:

3.1.1 Driving force of the crack

Figure 3.1 shows a schematic of a perturbed crack front of length c(z). Let f_0 be the reference position of the crack and $\delta f(z,x)$ a small but arbitrary perturbation of the crack so that $c(z) = f_0 + \delta f(z)$. A perturbation in the crack front, leads to the re-distribution of the driving force along the front. Let δ be the imposed displacement, at first order in the front perturbation, $\delta f(z) = c(z) - f_0$, the elastic energy release rate follows [Gao and Rice, 1989],

$$G(z,x) = G(f_0,\delta) + \left.\frac{dG}{df}\right|_{(f_0,\delta)} \delta f(z,x) + \frac{G(c_0,\delta)}{\pi} PV \int_{-\infty}^{\infty} \frac{\delta f(x,z') - \delta f(x,z)}{(z'-z)^2} dz' \quad (3.1)$$

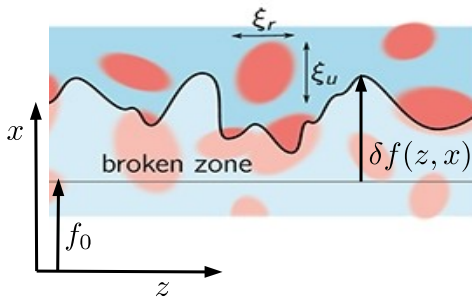

Fig. 3.1 *A semi-infinite crack perturbed in the $x-z$ plane with z directed along the width of the sample and x is direction of propagation. f_0 is the reference crack length position and δf is the perturbation from this reference position[Courtesy of Démery et al. [2014]]*

Now, as the external loading, δ increases, the driving force increases too. For small crack propagation distances, we can write $G(f_0,\delta)$ as

$$G(f_0,\delta) = G(f_0,\delta_0) + \left.\frac{\partial G}{\partial \delta}\right|_{f_0,\delta_0} v_{ext} t \quad (3.2)$$

where v_{ext} is the opening rate imposed by the loading machine. Substituting Eq. (3.2) in Eq. (3.1), it is just the opening rate in Eq. (3.1) which needs to be updated as the contribution to the second and the third term will be of second order.
This allows us to simplify the driving force as

$$G(z,x) = G(f_0,\delta_0) + \left.\frac{\partial G}{\partial \delta}\right|_{f_0,\delta_0} v_{ext}t + \left.\frac{dG}{df}\right|_{(f_0,\delta_0)} \delta f(z,x) + \frac{G(c_0,\delta_0)}{\pi} PV \int_{-\infty}^{\infty} \frac{\delta f(x,z') - \delta f(x,z)}{(z'-z)^2} dz' \tag{3.3}$$

Let us define the normalized variation in the driving force as :

$$\delta g(z,x) = \frac{G(z,x) - G(f_0,\delta_0)}{G(f_0,\delta_0)}$$

Eq. (3.3) can then be rewritten as:

$$\delta g(z,x) = \frac{v_m t - \delta f(z,x)}{\mathcal{L}} + \frac{1}{\pi} PV \int_{-\infty}^{\infty} \frac{\delta f(x,z') - \delta f(x,z)}{(z'-z)^2} dz' \tag{3.4}$$

where we introduce a structural length $\mathcal{L} = -\frac{G(f_0,\delta_0)}{\left.\frac{\partial G}{\partial f}\right|_{f_0,\delta_0}}$. The length scale is defined with a negative sign cause for a stable fracture test geometry, the driving force decreases with the crack length and hence the value of $\frac{dG^0}{df}$ is negative. We also define an average velocity v_m of the crack as $v_m = -\frac{\partial G/\partial\delta|_{(f_0,\delta_0)}}{\partial G \partial f|_{(f_0,\delta_0)}}$. The integral term in the expression of the driving force is a semi-local term contributing to an effective line elasticity of the front and tends to straighten the crack front.

3.1.2 Fracture energy

We define the fracture energy by a toughness contrast , $C \ll 1$ defined as :

$$C g_c(z,x) = \frac{G_c(z,x) - < G_c >}{< G_c >} \tag{3.5}$$

where $< G_c >$ is the average fracture energy of the material.

3.1.3 Kinetic law

To define the kinetic law, we've seen in section 2.2.5 that the fracture energy depends on the velocity of the crack v, following a power law with exponent γ. For a crack whose velocity does not change too much w.r.t mean velocity v_m we can write a Taylor series expansion of $G_c(v)$ around v_m as

$$G_c(v) = G_c(v_m) + \frac{\partial G_c}{\partial v}|_{v_m}(v - v_m)$$

The reference fracture energy at v_m is given by Eq. (3.5) as $G_c(z,x)|v_m = (1+C) < G_c >$. Let us also define $v_0 = \frac{<G_c>}{\frac{\partial G_c}{\partial v}|_{v_m}}$ as a characteristic velocity of the material depending on how the toughness changes with velocity. This allows us to define the normalized variation of the toughness as

$$\delta g_c(z,x) = \frac{G_c(z,x) - < G_c >}{< G_c >}$$

which can be simplified using the definitions of v_0 and $G_c(z,x)|v_m$ as

$$\delta g_c(z,x) = C g_c(z,x) + \frac{v - v_m}{v_0} \tag{3.6}$$

3.2 Crack front pinned by an obstacle

From Eq. (3.4) and (3.6) and the Griffith criterion, we can solve the crack front evolution of a crack encountering an obstacle.

At *zero order*, we have $G(f_0, \delta_0) =< G_c >$ and at *first order* we have $\delta g(z,x) = \delta g_c(z,x)$. This writes as

$$\frac{v_m t - \delta f(z,x)}{\mathcal{L}} + \frac{1}{\pi} PV \int_{-\infty}^{\infty} \frac{\delta f(x,z') - \delta f(x,z)}{(z'-z)^2} dz' = C g_c(z,x) + \frac{\frac{\partial \delta f}{\partial t} - v_m}{v_0}$$

One can simplify this equation by moving to the reference frame of the crack by substituting $\overline{\delta f} = \delta f - v_m t$, which simplifies to

$$\frac{-1}{\mathcal{L}} \overline{\delta f}(z,x) + \frac{1}{\pi} PV \int_{-\infty}^{\infty} \frac{\overline{\delta f}(x,z') - \overline{\delta f}(x,z)}{(z'-z)^2} dz' = C g_c(z,x) + \frac{1}{v_0} \frac{\partial \overline{\delta f}}{\partial t} \tag{3.7}$$

This is a complex integro-differential equation which simplifies a lot if we move to the Fourier space. Let us define the Fourier and the inverse Fourier transform of a function $\phi(z)$ as

$$\phi(z) \equiv \int_{-\infty}^{\infty} \widehat{\phi}(k) e^{ikz} dk \qquad \Longleftrightarrow \qquad \widehat{\phi}(k) \equiv \frac{1}{2\pi} \int_{-\infty}^{\infty} \phi(z) e^{-ikz} dz$$

Thus, Eq. (3.7) simplifies in the Fourier space to,

$$\frac{-1}{\mathcal{L}} \widehat{\delta f}(k,t) - |k| \widehat{\delta f}(k,t) = C \widehat{g_c}(k,t) + \frac{1}{v_0} \frac{\partial \widehat{\delta f}}{\partial t}$$

For completeness and ease of following, we first present the solution for a crack front pinned by an obstacle of constant width already studied in [Chopin et al., 2011, Dalmas et al., 2009, Vasoya et al., 2013] and then we extend this solution to a triangle.

3.2.1 Crack front pinned by an obstacle of constant width

For an obstacle of constant width, a steady-state solution exists, and thus there is no dependence on time. We assume $g_c(z,x)$ as a step function with value 1 inside the obstacle and 0 outside.

$$g_c(x,z) = \begin{cases} 1 & \text{if } |z| \leqq d \\ 0, & |z| > d \end{cases}$$

where d is the width of the defect.

Then, the equation providing the front deformation in the Fourier space is given as

$$\widehat{\delta f}(k) = -\frac{sin(kd)}{\pi k[|k| + \frac{1}{\mathcal{L}}]} \tag{3.8}$$

Taking the inverse fourier transform,

$$\overline{\delta f}(z) = \int_{-\infty}^{\infty} \widehat{\delta f}(k) e^{ikz} dk \tag{3.9}$$

The integral (3.9) is always convergent as for a stable crack, $\frac{\partial G}{\partial f} < 0 \Longleftrightarrow \mathcal{L} > 0$ that corresponds to a stable fracture test geometry. However, in the limit $\frac{\partial G}{\partial f} \to 0 \Longleftrightarrow \mathcal{L} \to \infty$, which in physical terms means that the characteristic distance $\mathcal{L}$ of variations in the driving force is much larger than the front perturbations. The integral can still be computed if one considers the deviation of the front position from the reference position $\delta f(0)$. Thus, the solution of Eq. (3.9) is [Chopin et al., 2011, Vasoya et al., 2013]

$$\delta f(z) - \delta f(0) = \frac{Cd}{\pi}\Big[(1+u)log(|1+u| + (1-u)log(|1-u|)\Big]$$

where $u = \frac{z}{d}$ and C is the toughness contrast. One must observe that as $u \to \infty$, $\delta f \to \frac{2Cd}{\pi} \log(|z|/d)$ which is reminiscent of the long-range elasticity of the front.

3.2.2 Crack front pinned by an obstacle of varying width

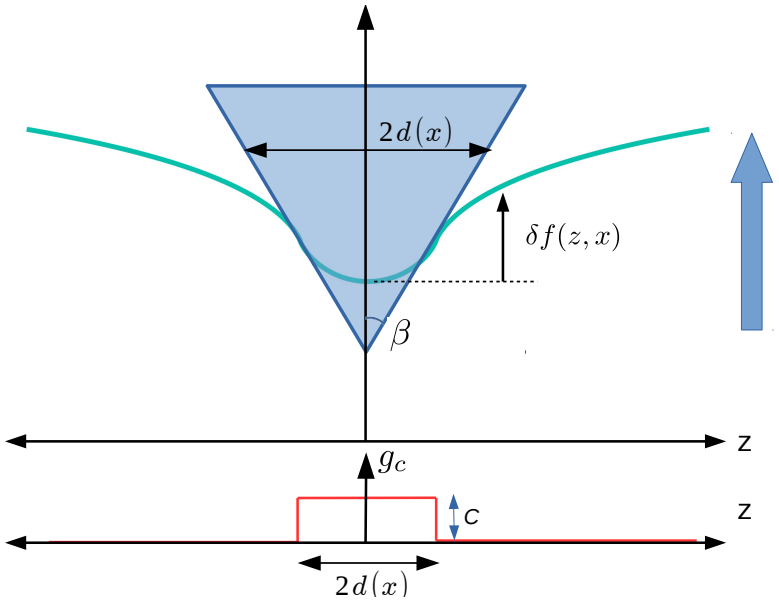

Fig. 3.2 *Schematic of a crack front pinned by a triangular obstacle. The big blue arrow points in the crack propagation direction.*

Fig. 3.2 shows a schematic of a crack front encountering a triangle region of higher toughness. Let us define β as the half-angle of the triangle, $\dot{d} = v_m \tan\beta$ as the rate at

which the triangle width increases. we define $g_c(z,x)$ as a step function with 1 inside the defect and 0 outside.

$$g_c(x,z) = \begin{cases} 1 & \text{if } |z| \leqq d(x) \\ 0, & |z| > d(x) \end{cases}$$

As the defect width varies with time, the equation governing the front shape is now a partial differential equation in time, and in Fourier space, it reads as

$$\frac{1}{v_0}\frac{\partial \widehat{\delta f}}{\partial t} + \left(\frac{1}{\mathcal{L}} + |k|\right)\widehat{\delta f}(k,t) = -C\widehat{g_c}(k,t)$$

Using the Fourier transform of $g_c(z,t)$ for a triangle, we obtain

$$\frac{1}{v_0}\frac{\partial \widehat{\delta f}}{\partial t} + (\frac{1}{\mathcal{L}} + |k|)\widehat{\delta f}(k,t) = -C\frac{sin(kd(t))}{\pi k}$$

This is a linear ODE in time, with the boundary condition $\widehat{\delta f}(k,0) = 0$, its solution in the Fourier space can be written as :

$$\widehat{\delta f}(k,t) = \frac{C\epsilon}{\pi\left((\frac{1}{\mathcal{L}} + |k|)^2 + k^2\epsilon^2\right)}\left[cos(k\dot{d}t) - \frac{1}{k\epsilon}\left(\frac{1}{\mathcal{L}} + |k|\right)sin(k\dot{d}t) - e^{-v_0(\frac{1}{\mathcal{L}}+|k|)t}\right] \quad (3.10)$$

where we introduce the parameter $\epsilon = \dot{d}/v_0$, which is the ratio of rate of increase of the triangle width to a characteristic velocity of the material v_0 introduced in Eq. (3.6). To obtain the solution in real space, we calculate the inverse-Fourier of the above equation given by

$$\overline{\delta f}(z,t) = \int_{-\infty}^{\infty} \widehat{\delta f}(k)e^{ikz}dk$$

We again look at the convergence of the integral as $\mathcal{L} \to \infty$. We find that the integral is divergent, but convergent if we look for the deviation of the crack from straightness. Thus, the deviation of the crack from the reference position $\delta f(0,x)$ is given by

$$\delta f(z,x) - \delta f(0,x) = \frac{Cd(x)}{\pi(1+\epsilon^2)}\Big[-\epsilon\lambda\pi(|u|-1) + (1+u)log(|1+u|) + (1-u)log(|1-u|) + 2\epsilon u\ \tan^{-1}(u\epsilon) - log(1+u^2\epsilon^2)\Big]$$

where $u = \frac{z}{d(x)}$ and λ is a constant dependent on u as follows

$$\lambda(u) = \begin{cases} 0 & \text{if } |u| \leq 1 \\ 1, & \text{if} |u| > 1 \end{cases}$$

As the defect size is continuously increasing, we do not have a steady solution but a front deformation increasing with increasing width of the triangle. However, if we

renormalize the front deformation w.r.t the defect width as $(\delta f(z,x) - \delta f(0,x))/d(x)$ where $u = z/d(x)$, we can collapse the front shapes on a single master curve that is characterized by the toughness contrast of the obstacle and the parameter ϵ introduced earlier which characterizes how fast the defect size increases. Fig. 3.3 shows a plot of the normalized front deformation for different values of ϵ. For high ϵ, when the width of the triangle increases much faster than the characteristic velocity of the material, the front does not have enough time to deform and shows thus small perturbation, while when ϵ approaches zero, we recover the solution of a crack pinned by a constant obstacle. In the latter case we see that the front deformation shows logarithmic tails for $u \to \infty$. However for a triangular obstacle, the deformation of the renormalized front flatten out reaching a constant value $\frac{C}{\pi(1+\epsilon^2)}(\epsilon\pi - 2\log\epsilon)$, which is evident for $\epsilon = 1$ and $\epsilon = 2$ on Fig. 3.3.

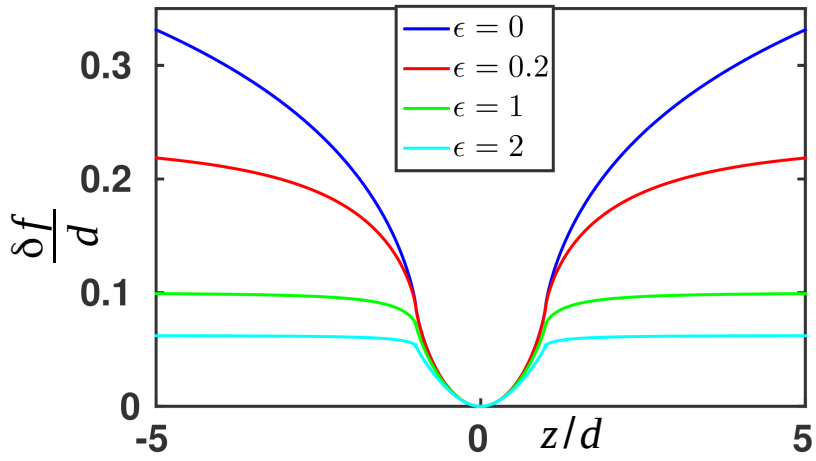

Fig. 3.3 *Solution of a crack front pinned by a triangular obstacle for a given toughness contrast $C = 0.2$ and different ϵ values.*

Physical interpretation of the parameter ϵ

Let us now look at a more physical interpretation of the parameter ϵ. In polymeric materials like PMMA, one can approximate the variation of the fracture energy with crack velocity by a power law as :

$$G_c(v) = G_{c0} v_m^{\gamma}$$

where γ is the exponent of the power law (see section 2.2.6). Assuming such a power law, the value of v_0 for a crack growing with velocity v_m can now be given as :

$$v_0 = \frac{v_m}{\gamma}$$

By following a point on the edge of the defect, one can also relate the average velocity of the crack with the rate of increase of the defect width as

$$\dot{d} = v_m tan(\beta)$$

This leads to a new relation for ϵ that follows

$$\epsilon = \frac{\dot{d}}{v_0} = \gamma tan(\beta)$$

Thus parameter ϵ writes then as a product of two fully independent quantities, β coming from the geometry of the defect and γ coming from the kinetic law $G_c(v_m)$. In the limit $\gamma = 0$, that corresponds to a propagation that ensures $G = G_{c0}$, at any time G_{c0} is a constant, one recovers $\epsilon = 0$, i.e. the behavior of a crack pinned by a rectangular obstacle, irrespective of the value of β.

Extension to heterogeneous dependence of $G_c(v)$

In this section, we would like to address the case when the dependence of the fracture energy with velocity is not the same inside and outside the obstacle. This typically is the case in experiments, where the heterogeneities are patterned using a different material [Chopin et al., 2011, Vasoya et al., 2016]. This would then result in two different characteristic spees v_0^1 and v_0^2 and two different equations inside and outside the defect that are related by the continuity condition of the front at the border of the defect. Let $\epsilon_1 = \dot{d}/v_0^1$ and $\epsilon_2 = \dot{d}/v_0^2$, and without going through the details of the calculation, the deformation of the crack front for a heterogeneous variation of $G_c(v)$ is found to be

Inside the defect ($|u| \leq 1$),

$$\begin{aligned}\frac{\delta f(t,z) - \delta f(t,0)}{d(t)} =& \frac{C}{\pi(1+\epsilon_1^2)}(-\epsilon_1\lambda\pi(|u|-1) + (1+u)log(|1+u|) + \\ & (1-u)log(|1-u|)) + \frac{\delta_1}{\epsilon_1}(2\epsilon_1 u \ \tan^{-1}(u\epsilon_1) - log(1+(u\epsilon_1)^2))\end{aligned}$$

and outside the defect ($|u| > 1$)

$$\begin{aligned}\frac{\delta f(t,z) - \delta f(t,0)}{d(t)} =& \frac{C}{\pi(1+\epsilon_2^2)}(-\epsilon_2\lambda\pi(|u|-1) + (1+u)log(|1+u|) + \\ & (1-u)log(|1-u|)) + \frac{\delta_2}{\epsilon_2}(2\epsilon_2 u \ \tan^{-1}(u\epsilon_2) - log(1+(u\epsilon_2)^2))\end{aligned}$$

where δ_1 and δ_2 are two constants given as

$$\delta_1 = (\frac{\frac{C}{\pi(1+\epsilon_2^2)}}{S_\epsilon} - \frac{T_\epsilon}{S_\epsilon})\epsilon_1$$

$$\delta_2 = (T_\epsilon + \frac{\delta_1 S_\epsilon}{\epsilon_1})\epsilon_2$$

with T_ϵ and S_ϵ given as:

$$T_\epsilon = \frac{2Clog(2)}{\pi}\frac{\frac{1}{1+\epsilon_1 2} - \frac{1}{1+\epsilon_2 2}}{2\epsilon_2 tan^{-1}(\epsilon_2) - log(1+\epsilon_2^2)}$$

$$S_\epsilon = \frac{2\epsilon_1 tan^{-1}(\epsilon_1) - log(1+\epsilon_1^2)}{2\epsilon_2 tan^{-1}(\epsilon_2) - log(1+\epsilon_2^2)}$$

As long as ϵ_1 and ϵ_2 are small, typically of the order of 10% or smaller, the solution of a crack pinned by a rectangular obstacle remains a good approximation.

3.3 Crack pinning under shear loading conditions

Till the last section we dealt with a planar crack that is allowed to propagate within the mean fracture plane. In this section, we will look at the out-of-plane deviation of a crack under the influence of a small amount of shearing mode (mode II), given by its SIF K^0_{II} and a small amount of tearing mode (mode III) and its SIF K^0_{III} while it is pinned by a tough obstacle. This theoretical study is interesting as the coupling between the shearing or the tearing mode with the in-plane deformation of the crack results in non-uniform out-of-plane excursion of the crack. With this in mind, a calculation was recently carried out by Leblond and Ponson [2016] where a crack subject to mode I + III is pinned by an obstacle of constant width. It showed an asymmetric out-of-plane response with the crack rotating inside the defect while staying flat outside. Here we go beyond a mode I + III loading and investigate mode I + II + III study. Later on we will allow the crack to interact with heterogeneities of varying width.

To carry out the calculation of the front geometry, we will use again a perturbative analysis to the first order in the in-plane and out-of-plane perturbations provided by the formulas of Rice [1985] and Movchan et al. [1998] respectively. The solutions of the crack front position will then be calculated using a double criterion:(i) Griffith criterion $G = G_c$ and (ii) the principle of local symmetry [Gol'dstein and Salganik, 1974] that assumes that the local shear is always equal to zero, .i.e. $k_{II}(z, x) = 0$. We first summarize the linearized formulae of the stress-intensity factors for both in-plane and out-of-plane front perturbations in the presence of mode I, II and III.

3.3.1 Stress-intensity factors for a perturbed crack under mode I + II + III

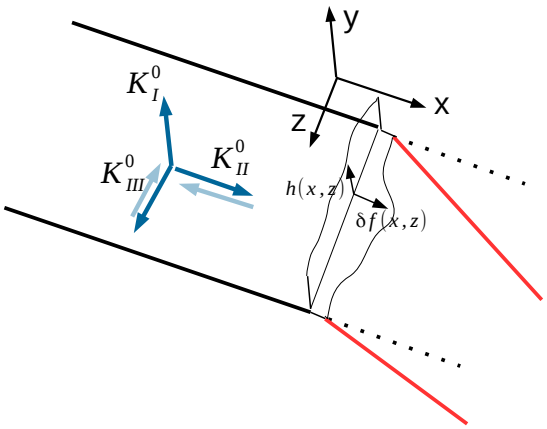

Fig. 3.4 *Figure shows a schematic of a perturbed crack under mixed mode (I + II + III) loading.*

Figure 3.4 shows a schematic of the crack front perturbed in the mean fracture plane and subjected to a mode (I + II+ III) loading. Mode II causes the crack to kink [Erdogan

and Sih, 1963], while mode III causes the crack to rotate and twist [Hull, 1994]. Let us consider an infinite body made of some isotropic material containing a planar semi-infinite crack as shown in Fig. 3.4. We choose standard notations of fracture mechanics where the X-axis provides the direction of propagation, the Z axis corresponds to the crack front direction and Y is perpendicular to the fracture plane. Let us now introduce a small perturbation $\delta f(z,x)$ and $h(z,x)$ in-plane and out-of-plane, respectively. The stress-intensity factors (SIF) are modified along the crack front and to the first order in the front perturbation, they are given by the formulas of Gao and Rice [1986] and Movchan et al. [1998].

Let us denote the p-th SIF due to the in-plane perturbation as $\delta_x k_p(z,x)$ where $p = I, II, III$ and due to the out-of-plane shape as $\delta_y k_p(z,x)$. To the first order, these SIF's are directly additive and thus the resultant SIF for the crack configuration is $\delta k_p = \delta_x k_p(z,x) + \delta_y k_p(z,x)$. We also make the assumption that the wavelength characterizing the crack front perturbation given here by the defect width d, is much smaller than any structural length in the material (especially $\mathcal{L} = K_I^0 / \frac{\partial K_I^0}{\partial f}$).

From the perturbative analysis of Gao and Rice [1986], the stress-intensity factors due to the in-plane perturbation of the crack to first order in perturbation are

$$\begin{cases} \delta_x k_I(z,x) = \dfrac{K_I^0}{2\pi} PV \displaystyle\int_{-\infty}^{\infty} \frac{\delta f(x,z') - \delta f(x,z)}{(z'-z)^2} dz' & (3.11) \\ \delta_x k_{II}(z,x) = -\dfrac{2}{2-\nu} K_{III}^0 \dfrac{\partial \delta f}{\partial z}(z,x) + \\ \qquad \dfrac{2-3\nu}{2-\nu} \dfrac{K_{II}^0}{2\pi} PV \displaystyle\int_{-\infty}^{\infty} \frac{\delta f(x,z') - \delta f(x,z)}{(z'-z)^2} dz' & (3.12) \\ \delta_x k_{III}(z,x) = \dfrac{2(1-\nu)}{2-\nu} K_{II}^0 \dfrac{\partial \delta f(z,x)}{\partial z} + \\ \qquad \dfrac{2+\nu}{2-\nu} \dfrac{K_{III}^0}{2\pi} PV \displaystyle\int_{-\infty}^{\infty} \frac{\delta f(x,z') - \delta f(x,z)}{(z'-z)^2} dz' & (3.13) \end{cases}$$

where ν is the Poisson's ratio of the material.
Now, from the formulae of Movchan et al. [1998], the perturbation in the stress-intensity factors due to out-of-plane deviation of the crack are given by,

$$\begin{cases} \delta_y k_I(z,x) = -\dfrac{3}{2} K_{II}^0 \dfrac{\partial h}{\partial x}(z,x) - 2K_{III}^0 \dfrac{\partial h}{\partial z}(z,x) - \\ \qquad \dfrac{K_{II}^0}{2\pi} PV \displaystyle\int_{-\infty}^{\infty} \frac{h(x,z') - h(x,z)}{(z'-z)^2} dz' + \delta_y K_I^{skew} \\ \delta_y k_{II}(z,x) = \dfrac{K_I^0}{2} \dfrac{\partial h}{\partial x}(z,x) - \dfrac{2-3\nu}{2-\nu} \dfrac{K_I^0}{2\pi} PV \displaystyle\int_{-\infty}^{\infty} \frac{h(x,z') - h(x,z)}{(z'-z)^2} dz' \\ \delta_y k_{III}(z,x) = \dfrac{2(1-\nu)^2}{2-\nu} K_I^0 \dfrac{\partial h}{\partial z}(z,x) \end{cases} \quad (3.14)$$

where $\delta_y K_I^{skew}$ is a non-local term connected to Bueckner's skew-symmetric crack-face weight functions (see [Movchan et al., 1998]). The general expression of this non-local term is

$$\delta_y K_1^{skew} = \frac{\sqrt{(}2)}{4\pi}\frac{1-2\nu}{1-\nu} Re\left[\int_{-\infty}^{0} dx' \int_{-\infty}^{\infty} \frac{K_{III}^0 - i(1-\nu)K_{II}^0}{(-x'+i(z-z'))^{3/2s}} \frac{\partial h/\partial z(x',z')}{\sqrt{-x'}} dz'\right]$$

The total SIF's are then given as $\delta k_p = \delta_x k_p + \delta_y k_p$ with $p = I, II, III$. In the following section, we use these formulae of the SIF's together with the double criterion to determine the full deformation of the crack under the influence of mixed mode loading when pinned by heterogeneities. We first simplify this problem by solving for a crack trapped by a heterogeneity and subjected to mode I and II only. We then later introduce a small amount of mode III to highlight the differences of the front shape for mode I + II + III and I + II.

3.4 Out-of-plane deviation of a crack subject to mode (I + II) and pinned by an obstacle

Let us assume that the obstacle has a toughness contrast, C defined as in section 3.1.2, as

$$C = \frac{G_c^o - < G_c >}{< G_c >}$$

where G_c^o is the fracture energy of the obstacle and $< G_c >$ is the average fracture energy of the material.
Let us define here another variable which quantifies the mode-mixity

$$\phi = \frac{K_{II}^0}{K_I^0}$$

For a crack under mode I + II, we have $K_{III}^0 = 0$, and thus in Eqs. (3.11) -(3.14), terms proportional to K_{III}^0 are ignored.

We now make a small departure to look at the order of the perturbations of each of the terms of the SIF in equations Eq. (3.11) - Eq. (3.14). The in-plane perturbation $\delta f(z,x)$ is only due to the toughness contrast of the obstacle and hence it is of the order $\mathcal{O}(C)$, while the out-of-plane deviation $h(z,x)$ occurs due to a combination of both the in-plane perturbation and mode-mixity and hence it is of order $\mathcal{O}(\phi C)$. As the SIF's are additive, one can simplify further by considering only the dominant terms. All terms are dominant except the contributions of $\delta_y k_I$ which are of the order $\mathcal{O}(\phi^2 C)$ which is ignored as we assume $\phi \ll 1$.
Thus, for a crack under mode (I + II), the final stress-intensity formulae simplify and read as :

$$\begin{cases} \delta_x k_I(z,x) = \dfrac{K_I^0}{2\pi} PV \displaystyle\int_{-\infty}^{\infty} \frac{\delta f(x,z') - \delta f(x,z)}{(z'-z)^2} dz' \\ \delta_x k_{II}(z,x) = \dfrac{2-3\nu}{2-\nu}\dfrac{K_{II}^0}{2\pi} PV \displaystyle\int_{-\infty}^{\infty} \frac{\delta f(x,z') - \delta f(x,z)}{(z'-z)^2} dz' \\ \delta_x k_{III}(z,x) = \dfrac{2(1-\nu)}{2-\nu} K_{II}^0 \dfrac{\partial \delta f(z,x)}{\partial z} \end{cases} \tag{3.15}$$

and

$$\begin{cases} \delta_y k_I(z,x) = 0 \\ \delta_y k_{II}(z,x) = \dfrac{K_I^0}{2}\dfrac{\partial h}{\partial x}(z,x) - \dfrac{2-3\nu}{2-\nu}\dfrac{K_I^0}{2\pi} PV \displaystyle\int_{-\infty}^{\infty} \frac{h(x,z') - h(x,z)}{(z'-z)^2} dz' \\ \delta_y k_{III}(z,x) = \dfrac{2(1-\nu)^2}{2-\nu} k_I^0 \dfrac{\partial h}{\partial z}(z,x) \end{cases} \tag{3.16}$$

We first use the Griffith energetic criterion which is based on the balance of the local energy-release rate and the fracture energy. For a crack under mixed mode (I + II), by using Irwin's formula, the local energy release rate is given as

$$G = \frac{1-\nu^2}{E}(k_I^2 + k_{II}^2)$$

and the perturbation $\delta G(z,x)$ of the energy release-rate can be written as

$$\delta G(z,x) = 2\frac{1-\nu^2}{E} k_I \delta k_I(z,x) + 2\frac{1-\nu^2}{E} k_{II}\delta k_{II}(z,x)$$

However, by the principle of local symmetry, we have $k_{II} = 0$, simplifying the perturbation in the energy-release rate as:

$$\delta G(z,x) = 2\frac{1-\nu^2}{E} K_I^0 \delta k_I(z,x)$$

It is interesting to observe that the perturbation in the energy release rate is completely independent of the mode II SIF and the out-of-plane displacement and the Griffith's criterion reduces to a planar crack problem of a crack front pinned by an obstacle. This problem has been well studied already [Chopin et al., 2011] and for an obstacle of constant and varying width the solution is reported in sections 3.2.1 and 3.2.2.

We now write the second criterion for the crack which is based on the principle of local symmetry [Gol'dstein and Salganik, 1974] which states that the crack chooses a path such that the local mode II shear is zero. In other words, we must've

$$k_{II}(z,x) = 0$$

Adding the contributions of mode II coming from the in-plane and the out-of-plane perturbations (See Eq. (3.15) and (3.16)), and a macroscopic mode II, the total mode II shear faced by the crack is

$$k_{II}(z,x) = K_{II}^0 + K_I^0 \frac{\partial h}{\partial x}(z,x) - \frac{2-3\nu}{2-\nu}\frac{K_I^0}{2\pi} PV \int_{-\infty}^{\infty} \frac{h(x,z') - h(x,z)}{(z'-z)^2} dz' + \frac{2-3\nu}{2-\nu}\frac{K_{II}^0}{2\pi} PV \int_{-\infty}^{\infty} \frac{\delta f(x,z') - \delta f(x,z)}{(z'-z)^2} dz'$$

Dividing the whole equation by K_I^0 and using $\phi = \frac{K_{II}^0}{K_I^0}$, we can re-write it as

$$\phi + \frac{1}{2}\frac{\partial h}{\partial x}(z,x) - \frac{2-3\nu}{2-\nu}\frac{1}{2\pi}PV\int_{-\infty}^{\infty}\frac{h(x,z')-h(x,z)}{(z'-z)^2}dz' + \frac{2-3\nu}{2-\nu}\frac{\phi}{2\pi}PV\int_{-\infty}^{\infty}\frac{\delta f(x,z')-\delta f(x,z)}{(z'-z)^2}dz' = 0$$

With the change of variables $\delta h(z,x) = h(z,x) + 2\phi x$, which subtracts the average kink plane, we can simplify the equation to

$$\frac{\partial \delta h}{\partial x}(z,x) - \frac{2-3\nu}{2-\nu}\frac{1}{\pi}PV\int_{-\infty}^{\infty}\frac{\delta h(x,z')-\delta h(x,z)}{(z'-z)^2}dz' + \frac{2-3\nu}{2-\nu}\frac{\phi}{\pi}PV\int_{-\infty}^{\infty}\frac{\delta f(x,z')-\delta f(x,z)}{(z'-z)^2}dz' = 0$$

This equation is even simpler in the Fourier space. Defining the Fourier transform in the same manner as in Equation 3.2, the equation simplifies to

$$\frac{\partial \widehat{\delta h}}{\partial x}(k,x) + A|k|\widehat{\delta h}(k,x) - A\phi\widehat{\delta f}(k,x) = 0 \tag{3.17}$$

where $A = \frac{2-3\nu}{2-\nu}$, a function of Poisson's ratio, defined for convenience. To solve for the out-of-plane problem, we need to substitute in Eq. (3.17), the Fourier transform of the in-plane perturbation $\widehat{\delta f}(k,x)$. For two obstacle geometries,*viz.* constant width and varying width, this result has already been calculated and we discuss the out-of-plane solution for these two cases in the following sections.

3.4.1 Crack pinned by a rectangular obstacle subjected to mode I+II

From Eq. (3.8) as $\mathcal{L} \to \infty$, the Fourier transform of the in-plane solution is given as

$$\widehat{\delta f}(k) = -\frac{sin(kd)}{\pi k|k|} \tag{3.18}$$

where d is the width of the obstacle. Substituting Eq. (3.18) in Eq. (3.17), we can solve the partial differential equation in $\widehat{\delta h}(k,x)$ and x with the boundary condition $\delta h(k,0) = 0$

$$\widehat{\delta h}(k,x) = -\phi C\frac{sin(kd)}{\pi k|k|}\left(1 - e^{-A|k|x}\right)$$

We are now left to take the inverse-fourier transform to obtain the solution in the real space that follows

$$\delta h(z,x) = \int_{-\infty}^{\infty}\left(-\phi C\frac{sin(kd)}{\pi k|k|}\left(1 - e^{-A|k|x}\right)\right)e^{ikz}dk$$

The final solution reads as :

$$\delta h(z,x) = \frac{-C\phi d}{\pi}\Big[Av\ \ tan^{-1}\Big(\frac{1+u}{Av}\Big) + Av\ \ tan^{-1}\Big(\frac{1-u}{Av}\Big) \\ \frac{1+u}{2}log((1+u)^2+A^2v^2) + \frac{1-u}{2}log((1-u)^2+A^2v^2) \\ -(1+u)log(|1+u|) - (1-u)log(|1-u|)\Big] \quad (3.19)$$

where $u = z/d$ and $v = x/d$ and $A = (2-3\nu)/(2-\nu)$. Note that the solution is here dependent on two parameters : the toughness contrast, C, and the mode-mixity ϕ. Fig. 3.5 plots the out-of-plane deviation of the crack front given in Eq. (3.19). We can see that the out-of-plane shape is highly non-uniform with points that were pinned by the obstacle showing a bump which is due to the coupling of a macroscopic K^0_{II} with $\delta f(z,x)$.

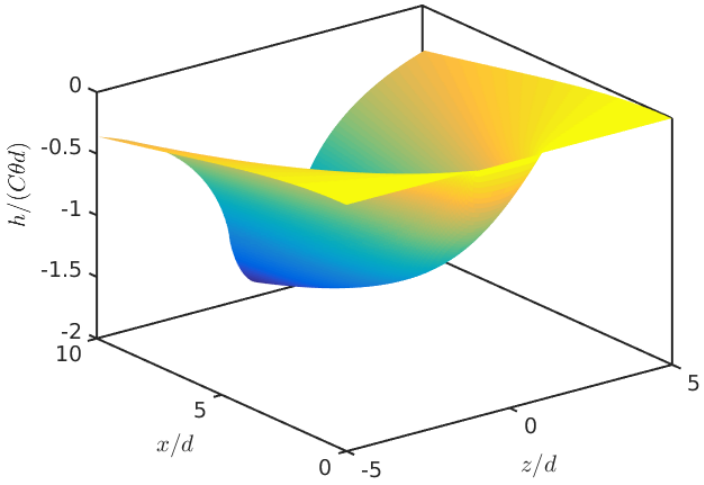

Fig. 3.5 *Out-of-plane solution of a crack pinned by a rectangular obstacle subject to a small amount of mode II. The crack is propagating in the direction of positive x. x, z and δh have been normalized w.r.t half width,d of the defect.*

Fig. 3.6 shows the out-of-plane solution for different values of x. Fig 3.6(a), shows the evolution of the out-of-plane shape as x increases. As x increases, the out-of-plane shape continuously increases and one can show that the point at the centre of the defect diverges logarithmically as $\delta h(0,x) = \frac{-2C\phi d}{\pi}(1+log(Av))$ (See Fig. 3.6 (b)). Far away from the defect $z \to \infty$, the value of $\delta h(z,x) \to 0$ (see Fig. 3.6 (a)).

3.4.2 Crack pinned by a triangular obstacle subjected to mode (I+II)

We continue from Eq. (3.17) and we recollect the in-plane Fourier space solution for a triangular obstacle derived in Eq. (3.10) in the limit $\mathcal{L} \to \infty$

$$\widehat{\delta f}(k,x) = \frac{C\epsilon}{\pi k^2(1+\epsilon^2)}\Big[cos(k\beta x) - \frac{|k|}{k\epsilon}sin(k\beta x) - e^{-\frac{|k|\beta x}{\epsilon}}\Big]$$

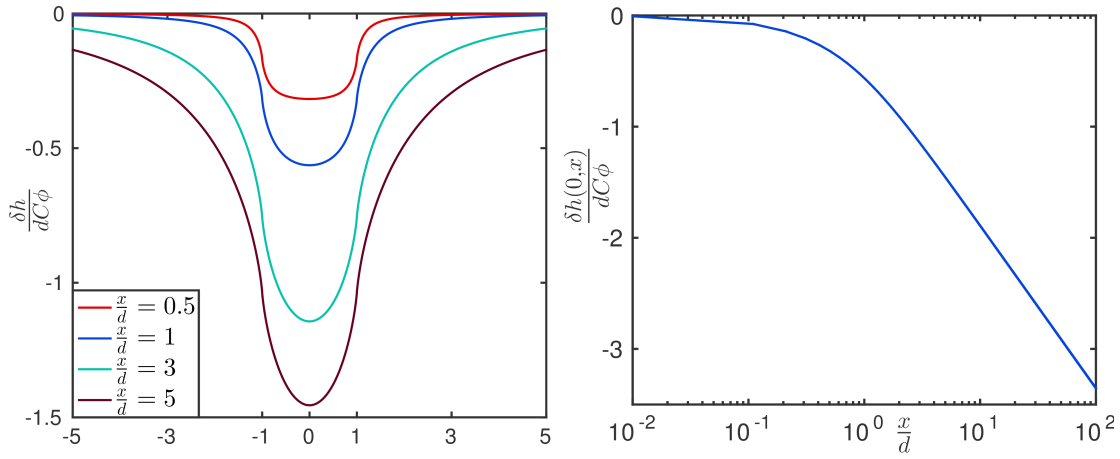

Fig. 3.6 *Evolution of the out-of-plane deformation: (a) Normalized out-of-plane shape with normalized z as x increases. The out-of-plane shape increases as the crack propagates. However far away from the defect for $z \to \infty$, $\delta h \to 0$. (b) shows the evolution of $\delta h(0,x)$ vs x and that exhibit a logarithmic deviation.*

where $\epsilon = \dot{d}/v_0$ and where we changed the variable t by x using the relation $t = \beta x/\dot{d}$. Following a procedure similar to that of the rectangular obstacle, we substitute (3.18) into Eq. (3.17) to solve the linear differential equation with boundary condition $\delta h(k,0) = 0$ and compute the inverse Fourier transform leading to:

$$\frac{\delta h(z,x)}{\beta x} = \frac{A\phi C}{\pi(1+\epsilon^2)}\left\{\frac{A-\beta\epsilon}{A^2+\beta^2}\left[(1+u)\log|1+u| + (1-u)\log|1-u|\right] - \right.$$
$$\frac{A\epsilon+\beta}{A^2+\beta^2}(|u|-1)\lambda\pi + \frac{2\epsilon}{A\epsilon-\beta}\left[u\epsilon\tan^{-1}(u\epsilon) - 0.5log(1+u^2\epsilon^2)\right] -$$
$$\left.\frac{2\beta^2(1+\epsilon^2)}{(A^2+\beta^2)(A\epsilon-\beta)}\frac{A}{\beta}\left[\frac{u\beta}{A}\tan^{-1}(\frac{u\beta}{A} - \frac{1}{2}\log(1+\frac{u^2\beta^2}{A^2}))\right]\right\} + \Xi(x) \quad (3.20)$$

with

$$\Xi(x) = \frac{A\phi C}{\pi(1+\epsilon^2)}\frac{2\epsilon\log\epsilon(A^2+\beta^2) + \pi(\beta - A^2\epsilon^2) - 2A\beta(1+\epsilon^2)\log(\beta/A)}{(A^2+\beta^2)(A\epsilon-\beta)}$$

where $A = (2-3\nu)/(2-\nu)$, $u = z/d(x) = z/\beta x$ and $\epsilon = \dot{d}/v_0$.

An interesting property which we can observe is that the out-of-plane shape here also renormalizes like the in-plane solution, $\delta f(z,x)$ (see Section 3.4.2), i.e. if δh is normalized with $d(x)$, it can be written as a solution depending on $u = \frac{z}{d(x)}$ only. In other words,

$$\frac{\delta h(z,x)}{d(x)} = \mathcal{P}\left(\frac{z}{d(x)}\right)$$

We look at the particular case $\epsilon \to 0$ that corresponds to a large characteristic velocity or equivalently, slowly varying $G_c(v)$ (as a reminder $v_0 = G_c(v)/\frac{\partial G_c}{\partial v}$). The out-of-plane solution for $\epsilon = 0$ is

$$\frac{\delta h(z,x)}{\beta x} = \frac{\phi C}{\pi(1+(\frac{\beta}{A})^2)}\Bigg[(1+u)log(|1+u|)+(1-u)log(|1-u|)-\frac{\beta}{A}\lambda\pi(|u|-1) + \frac{\beta}{A}\Bigg(2utan^{-1}(\frac{u\beta}{A})-\frac{A}{\beta}log(1+\frac{u^2\beta^2}{A^2})\Bigg)-\frac{\beta}{A}\pi+2\log(\frac{\beta}{A})\Bigg] \quad (3.21)$$

Thus the out-of-plane solution also shows a bump inside the triangle. However the solution is now dependent on three parameters : the toughness contrast, C, the mode mixity ϕ and the angle of the triangle β. Figure 3.7 shows a 3D plot of the solution.

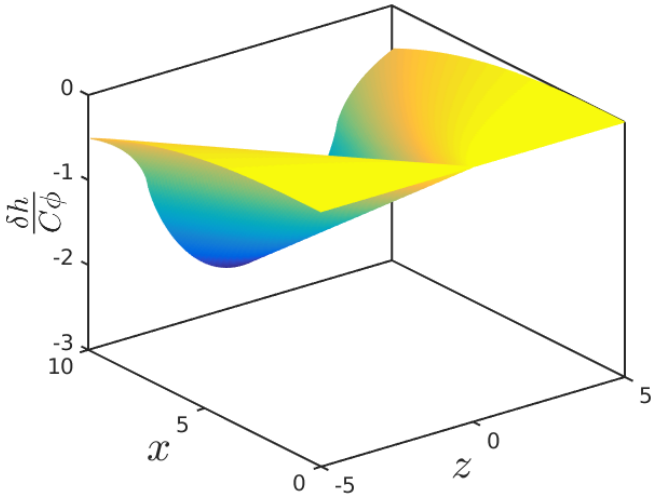

Fig. 3.7 *Out-of-plane shape of a crack pinned by a triangular obstacle subject to a small amount of mode II. To emphasize the evolution of the crack geometry, δh is not normalized by $d(x)$*

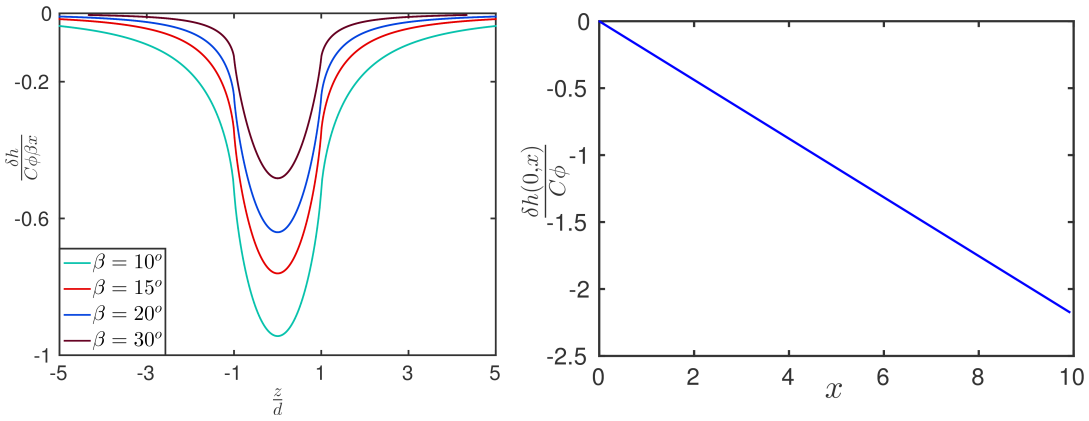

Fig. 3.8 *(a) Variation of the normalized out-of-plane shape with β (b) Deviation of the point, $\delta h(0,x)$, of the front located at the centre of the defect.*

Fig. 3.8(a) plots the normalized out-of-plane solution following Eq. (3.21) for different values of β. As the angle of the triangle increases, the crack faces a larger defect and hence the out-of-plane deviation decreases. Interestingly, even in the limit, $\epsilon \to 0$, we do see an effect of the angle of the triangle while the in-plane deformations are independent od β for $\epsilon \to 0$. This stems from the term $\frac{\partial \delta h}{\partial x}$ in Eq. (3.17) that governs the out-of-plane crack shape and that induces a dependence to the history of the propagation, even in the limit $\epsilon \to 0$. If we now look at the deviation $\delta h(0, x)$ of the point of the front at the centre of the defect, (see Figure 3.8 (b)) the displacement now varies linearly with x unlike the constant obstacle case where this deviation was logarithmic. We will later observe this behavior in experiments and use it to estimate a magnitude of K^0_{II} as the slope follows a linear dependency with x.

3.5 Problem definition for mode I + II + III

We now introduce a small tearing mode characterized by its SIF,K^0_{III} in addition to K^0_{II} and K^0_I. Let us define the mode III mixity parameter for K_{III} as

$$\rho = \frac{K^0_{III}}{K^0_I}$$

The introduction of K^0_{III} now requires to revisit the SIF formulae presented in Equations (3.11) - (3.14). Let us look at the new contributions to the value of δk_I. The two new contributions to be now included are $-2K^0_{III}\frac{\partial h}{\partial z}(z, x)$ and $\delta_y K^{skew}_I$. However each of these terms are proportional to K^0_{III} and to δh. Hence, their contributions are going to be of the order $\mathcal{O}(\rho\phi C)$ and $\mathcal{O}(\rho^2 C)$ which is really small and can be ignored. Thus there is no variation in the perturbation of the SIF in mode I.

The energy release rate can now be calculated as

$$\delta G = \frac{1-\nu^2}{E} 2\delta k_I K^0_I + 2\frac{1+\nu}{E}\delta k_{III} K^0_{III}$$

All terms in δk_{III} are of the order $\mathcal{O}(\rho C)$ or $\mathcal{O}(\phi C)$, hence, multiplied by K^0_{III}, their contribution to the perturbation in energy release rate is negligible. So, just like in the previous section of mode (I + II), this allows us to write the Griffith criterion independent of the out-of-plane perturbations allowing us to directly obtain the in-plane deformation $\delta f(z, x)$ of the crack. (See sections 3.2.1 and 3.2.2). For a rectangular and triangular obstacle, the in-plane solutions have already been derived in equations Eqs.(3.19) and (3.20).

We now look at the resultant mode II. K^0_{III} now introduces a new contribution $-\frac{2}{2-\nu}K^0_{III}\frac{\partial \delta f}{\partial z}(z, x)$ (see Eq. (3.12)) which is not negligible.

Thus the resultant mode II in this case is

$$k_{II}(z,x) = K^0_{II} + \frac{K^0_I}{2}\frac{\partial h}{\partial x}(z,x) - \frac{2-3\nu}{2-\nu}\frac{K^0_I}{2\pi} PV\int_{-\infty}^{\infty} \frac{h(x,z') - h(x,z)}{(z'-z)^2} dz' + \frac{2-3\nu}{2-\nu}\frac{K^0_{II}}{2\pi} PV\int_{-\infty}^{\infty} \frac{\delta f(x,z') - \delta f(x,z)}{(z'-z)^2} dz' - \frac{2}{2-\nu} K^0_{III}\frac{\partial \delta f}{\partial z}(z,x)$$

We then solve for the out-of-plane deformation by using the principle of local symmetry ,[Gol'dstein and Salganik, 1974],

$$k_{II}(z,x) = 0$$

We make a change of variables $\delta h(z,x) = h(z,x) + 2\phi x$ and we move into the Fourier space to simplify the equations as

$$\frac{\partial \widehat{\delta h}}{\partial x}(k,x) + A|k|\widehat{\delta h}(k,x) - A\phi\widehat{\delta f}(k,x) - 2D\rho ik\widehat{\delta f}(k,x) = 0 \tag{3.22}$$

where $A = \frac{2-3\nu}{2-\nu}$ and $D = \frac{2}{2-\nu}$.
Most of the equation retains the same form as Eq. (3.17), except now for a new additional term proportional to ρ. We now solve this equation for a crack pinned by a triangular obstacle under mode I + II + III.

3.6 Out-of-plane shape of a crack pinned by a triangular obstacle under mode I + II + III

The in-plane solution, $\delta f(z,x)$ of a crack pinned by a triangular defect is already derived in Eq. (3.10). We substitute this in Eq. (3.22) and take the inverse Fourier to get the final solution as

$$\delta h(z,x) = \delta h_{II}(z,x) + \delta h_{III}(z,x) \tag{3.23}$$

where δh_{II} is a term proportional to ϕ and δh_{III} is a term proportional to ρ that follows

$$\begin{aligned}\frac{\delta h_{II}(z,x)}{\beta x} = \frac{A\phi C}{\pi(1+\epsilon^2)}\Bigg\{ &\frac{A-\beta\epsilon}{A^2+\beta^2}\left[(1+u)\log|1+u| + (1-u)\log|1-u|\right] - \\ &\frac{A\epsilon+\beta}{A^2+\beta^2}(|u|-1)\lambda_{II}\pi + \frac{2\epsilon}{A\epsilon-\beta}\left[u\epsilon\tan^{-1}(u\epsilon) - 0.5log(1+u^2\epsilon^2)\right] - \\ &\frac{2\beta^2(1+\epsilon^2)}{(A^2+\beta^2)(A\epsilon-\beta)}\frac{A}{\beta}\left[\frac{u\beta}{A}\tan^{-1}(\frac{u\beta}{A} - \frac{1}{2}\log(1+\frac{u^2\beta^2}{A^2}))\right]\Bigg\} + \Xi(x)\end{aligned}$$

where $u = \frac{z}{d(x)} = \frac{z}{\beta x}$, $A = \frac{2-3\nu}{2-\nu}$, λ_{II} is a constant which depends on u as $\lambda_{II} = 0$ if $|u| \leq 1$ and $\lambda_{II} = 1$ if $|u| > 1$. Note that this term δh_{II} is exactly the same as in Eq. (3.20).
and

$$\begin{aligned}\frac{\delta h_{III}(z,x)}{\beta x} = \frac{2D\rho C}{\pi(1+\epsilon^2)}\Bigg\{ &\frac{A-\beta\epsilon}{A^2+\beta^2}\lambda_{III}\pi + \frac{A\epsilon+\beta}{A^2+\beta^2}\left[(1+u)\log|1+u| - (1-u)\log|1-u| - (2u)\log|u|\right] \\ &- \frac{2\epsilon}{A\epsilon-\beta}\left[\tan^{-1}(u\epsilon) + \frac{u\epsilon}{2}\log(1+\frac{1}{u^2\epsilon^2})\right] \\ &+ \frac{2\beta^2(\epsilon^2+1)}{(A^2+\beta^2)(A\epsilon-\beta)}\left[\frac{A}{\beta}\tan^{-1}(\frac{\beta u}{A}) + \frac{u}{2}\log(1+\frac{A^2}{u^2\beta^2})\right]\Bigg\}\end{aligned}$$

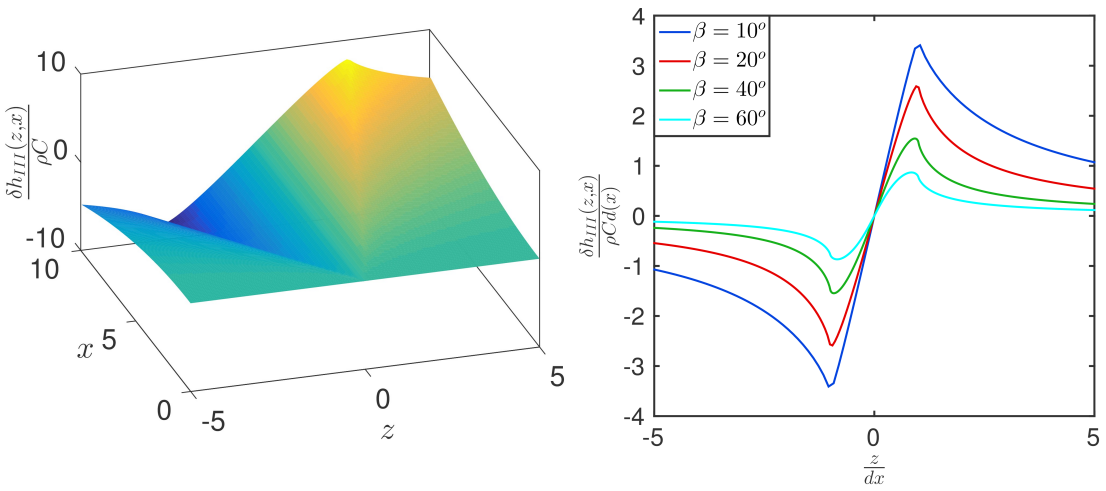

Fig. 3.9 *(a) Out-of-plane shape of a crack pinned by a triangular obstacle subject to mode I + III. Here as the width of the defect continuously varies, δh_{III} is not normalized w.r.t $d(x)$. (b) shows the normalized shape $\delta h_{III}(z,x)$ for different values of β*

where $u = \frac{z}{\beta x}$, $D = \frac{2}{2-\nu}$ and λ_{III} is also a function which depends on u as $\lambda_{III} = -1$ if $u < -1$, $\lambda_{III} = u$ if $|u| < 1$ and $\lambda_{III} = 1$ if $u > 1$.

Let us look at the individual components of the solution δh viz. $\delta h_{II}(z,x)$ (a term proportional to K^0_{II}) and δh_{III} (a term proportional to K^0_{III}) for $\epsilon = 0$. $\delta h_{II}(z,x)$ is symmetric w.r.t the plane Oxy (see Fig. 3.7). One can understand this property by looking at the contribution of the term proportional to K^0_{II} that follows $\frac{2-3\nu}{2-\nu}\frac{\phi}{\pi} PV \int_{-\infty}^{\infty} \frac{\delta f(x,z') - \delta f(x,z)}{(z'-z)^2} dz$. As $\delta f(z) = \delta f(-z)$, the semi-local term is also an even function, the solution $\delta h_{II}(z,x)$ is also even leading to a symmetric shape.

However, the stress-intensity factor contribution coming from mode III is $-\frac{2}{2-\nu} K^0_{III} \frac{\partial \delta f}{\partial z}(z,x)$ and the derivative of $\delta f(z,x)$ w.r.t z is an odd-function. Hence one expects the out-of-plane response to be odd too. The solution $\delta h_{III}(z,x)$ is shown in Figure 3.9. One observes that the crack is twisted inside the obstacle and tends to zero far from it. This behavior is reminiscent of the solution recently derived by Leblond and Ponson [2016] where a crack under mode I + III encounters a rectangular obstacle: the crack twists inside the obstacle while it remains flat outside it. Here, as the defect size continuously increases, the amplitude of the twist also continuously increases proportional to $d(x)$.

The final solution of a crack under mixed mode I + II + III is $\delta h(z,x) = \delta h_{II}(z,x) + \delta h_{III}(z,x)$. It is plotted for $\rho \simeq \phi/10$ in Fig. 3.10.

From this figure, one can readily observe that the resulting fracture surface (that is the trace let by the out-of-plane front shape $\delta h(x,z)$ is no more symmetric but has a slight asymmetry due to the presence of mode III. Thus the position of the top of the bump now translates with some angle w.r.t the propagation direction. This angle can be expressed analytically as

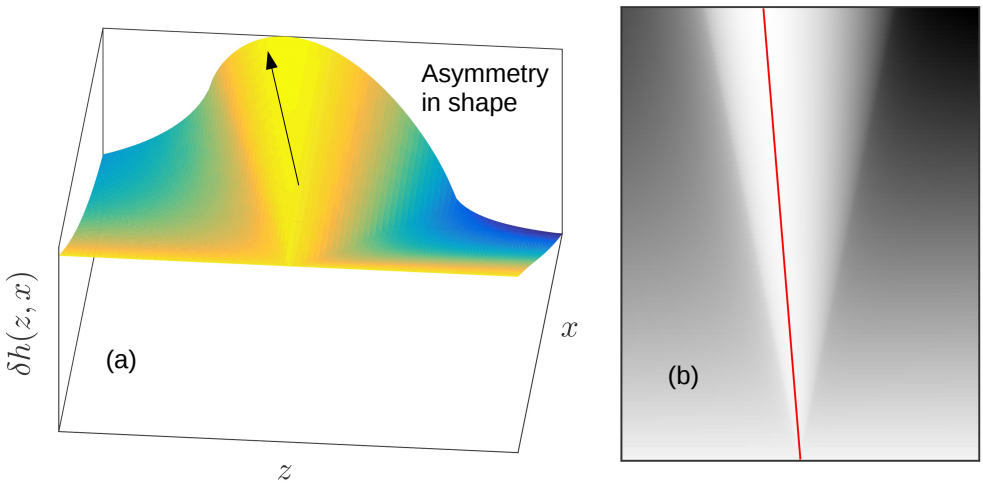

Fig. 3.10 *(a)3D shape of a crack encountering a triangular defect under mode I + II + III (b) highlights the assymmetry of the resulting fracture surface due to mode III*

$$\theta_{shift} = \mathcal{G}\left(\frac{\phi}{\rho}, \beta, \nu\right)$$

Thus for a dominantly tensile crack pinned by a heterogeneity mode II causes a bump in the shape and mode III causes an asymmetry in the shape of the bump. We will use this crucial observation in the coming chapter to analyze the triangular fracture patterns and extract a value of K_{II}^0 and K_{III}^0 from the fracture pattern.

Chapter 4

Linear stability analysis of a crack under mode I + II + III: On the effect of shear dependent fracture energy

Contents

In 1969, Sommer [Sommer, 1969] performed an extraordinary experiment where he breaks glass rods under tension (imposed by fluid pressure) and a small amount of torsion. He found out that the fracture surface shows a transition from a planar to a fragmented geometry as the crack propagates outward radially. This so-called crack front fragmentation under mode I + III is not seen in glass only but in many other materials such as polymeric glass [Knauss, 1970], epoxy resin [Hull, 1994], PMMA [Cooke and Pollard, 1996, Lazarus et al., 2008], Homalite [Lin et al., 2010], alumina [Suresh and Tschegg, 1987], steels [Eberlein et al., 2017, Lazarus et al., 2001, Yates and Miller, 1989], rocks [Pollard and Aydin, 1988, Pollard et al., 1982], gypsum and cheese [Goldstein and Osipenko, 2012], to name a few. In each of these experiments, the presence of a small

amount of mode III causes the crack front to twist, but however as crack cannot twist as a whole, it fragments leaving on the fracture surface the so called 'lances' [Sommer, 1969] or 'facets' that look like the rooftop of a factory. Further, Hourlier and Pineau [1979] observed that fragmented cracks form two types of facets where type A rotate such that it faces lower amount of anti-plane shear while type B rotates in the opposite direction facing a relatively higher anti-plane shear. Similar fracture patterns in various brittle materials suggest that front fragmentation under moder I + III may be captured by a unified theory based on fracture mechanics.

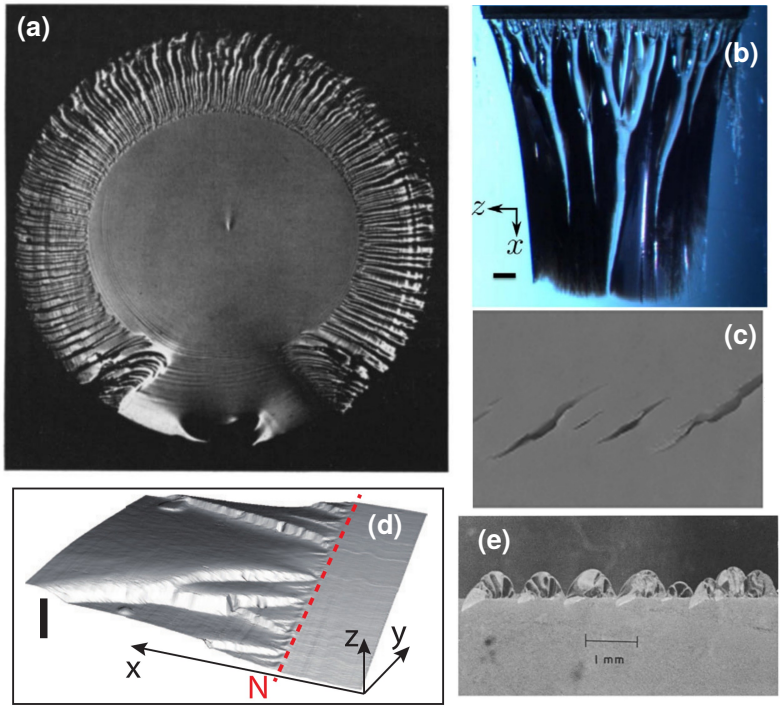

Fig. 4.1 *Fracture surface of a fragmented front in different materials under mode I + III: (a) is the experiment of Sommer on glass rods [Sommer, 1969] (b) shows a faceted crack in PMMA under three point bending of a tilted crack [Chen et al., 2015] (c) are facets observed on cheese [Goldstein and Osipenko, 2012](d) are facets seen on soft brittle gels [Ronsin et al., 2014] and (e) shows Type A facets leading over type B in Solithane 113 [Knauss, 1970]*

Recently, Pons and Karma [2010] showed through phase-field simulations of brittle fracture that a tensile crack under a certain amount of mode III do not remain straight but instead develop facets similar to the ones observed in experiments. Moreover, they found that at the onset of instability the perturbations of the crack front with respect to straightness can be accurately described by a helical front which grow non-linearly to form flat faceted shapes. Taking cue from these observations, Leblond et al. [2011] performed a linear stability analysis of a crack under mode I + III where the bifurcated mode are helicoidal fronts that satisfy both the Griffith criterion and the principle of local symmetry ($k_{II} = 0$ along the front). They found that beyond a critical threshold

$$\left(\frac{K^0_{III}}{K^0_I}\right)_{cr} = \sqrt{\frac{(1-\nu)(2-3\nu)}{3(2-\nu)-4\sqrt{2}(1-2\nu)}}$$

where ν is the Poisson's ratio of the material, the perturbations were growing exponentially fast. Considering the case of PMMA where $\nu = 0.37$, this critical threshold is around 0.4 which is much higher than the experimental value that is much closer to zero - note also that the existence of a finite threshold is even debated (see [Pham and Ravi-Chandar, 2014]). Even though it was proposed that the presence of material heterogeneities could trigger the fragmentation at a lower threshold [Chen et al., 2015, Leblond et al., 2011, Pham and Ravi-Chandar, 2017], the discrepancy between the theoretically predicted threshold and the experimentally measured values remains largely unexplained.

In the following we explore the effect of a shear dependent fracture energy on the fragmentation instability. The fracture energy of a material depends on the dissipative mechanisms happening at the crack tip vicinity. These mechanisms can be as diverse as plasticity in ductile alloys, micro-cracking in quasi-brittle solids like mortar or cavitation and fibrillation in polymeric materials. All these processes (and in particular the amount of energy they dissipate) depends on the nature of the surrounding stress field that can be characterized by its triaxiality (which is zero for pure shear and infinite for hydrostatic pressure). For this reason the fracture energy of weak interfaces is not the same under pure tension and under mixed mode I + II ([Freund and Suresh, 2004]). It turns out that G_c is an increasing function of k_{II}/k_I so that dissipation at the crack tip vicinity is larger in the presence of shear[1]. For cracks in isotropic solids, k_{II} is zero due to the principle of local symmetry. However k_{III} may not be zero along the front so that the dissipation rate could be different to that of a crack under mode I + III. We explore in the following its effect on the fragmentation instability in mode I + III. Let us assume

$$G_c(\rho) = G_c^I(1+\gamma\rho^\kappa) \qquad \text{with } \rho = \frac{k_{III}}{k_I} \tag{4.1}$$

where G_c^I is the fracture energy under pure mode I and γ and κ are material parameters which control the dependence of G_c on mode-mixity.

Recently Leblond et al. [in prep.], revisited the linear stability analysis of a crack under mode I + III with this new ingredient. The detailed calculation is not presented here. It resembles to the one of [Leblond et al., 2011]: helicoidal mode grows beyond a critical ratio $\frac{K^0_{III}}{K^0_I}|_c$. For a small value of K^0_{III} it is well approximated by:

$$\left(\frac{K^0_{III}}{K^0_I}\right)_{cr} \simeq \left[\frac{2-3\nu}{(4-5\nu)\kappa-(2-3\nu)}\frac{1}{\gamma}\right]^{\frac{1}{\kappa}}$$

Interestingly, the fragmentation threshold depends on the value of γ and κ: if γ is high, then the threshold for fragmentation falls down. In the next chapter, I will show that the triangular pattern observed in PMMA is related to the fragmentation instability and I will also show how to extract the value of γ from the shape of the fracture patterns.

[1] The telephone cord buckling pattern observed in thin films is an indirect proof of the dependence of G_c with $\frac{k_{II}}{k_I}$ as this had to be considered to explain and decipher their geometry[Faou et al., 2012].

In our experiments on PMMA samples the loading is dominantly tensile but are also submitted to a small amount of mode II and mode III due to some mis-alignment in the loading condition which I will show in the next chapter. In a more practical perspective, carrying out fracture under mode I + III is a difficult task. Generally fracture test geometries used to generate mode III also induce mode II (See [Lin et al., 2010],[Pham and Ravi-Chandar, 2014],[Ronsin et al., 2014]). Hence it is important to consider the presence of mode II in the previous linear stability analysis to be able to compare as quantitatively as possible experiments with theoretical predictions. In the following, I will present the linear stability analysis of a perturbed crack under mode I + II + III with a dependence of fracture energy on the amount of mode III. The influence of mode II on the geometry of the front and the fragmentation threshold will become clear in the end.

4.1 Loading conditions : local and macroscopic SIFs

We use the same theoretical framework used in the previous chapter to study crack pinning by triangular obstacles under mode II and III. The perturbation in the stress-intensity factors under mode (I + II + III) are given by Eqs. (3.11) - (3.14). We remind them here:

$$\begin{cases} \delta_x k_I(z,x) = \dfrac{K_I^0}{2\pi} PV \displaystyle\int_{-\infty}^{\infty} \frac{\delta f(x,z') - \delta f(x,z)}{(z'-z)^2} dz' \\ \delta_x k_{II}(z,x) = -\dfrac{2}{2-\nu} K_{III}^0 \dfrac{\partial \delta f}{\partial z}(z,x) + \dfrac{2-3\nu}{2-\nu} \dfrac{K_{II}^0}{2\pi} PV \displaystyle\int_{-\infty}^{\infty} \frac{\delta f(x,z') - \delta f(x,z)}{(z'-z)^2} dz' \\ \delta_x k_{III}(z,x) = \dfrac{2(1-\nu)}{2-\nu} K_{II}^0 \dfrac{\partial \delta f(z,x)}{\partial z} + \dfrac{2+\nu}{2-\nu} \dfrac{K_{III}^0}{2\pi} PV \displaystyle\int_{-\infty}^{\infty} \frac{\delta f(x,z') - \delta f(x,z)}{(z'-z)^2} dz' \end{cases} \tag{4.2}$$

and

$$\begin{cases} \delta_y k_I(z,x) = -\dfrac{3}{2} K_{II}^0 \dfrac{\partial h}{\partial x}(z,x) - 2K_{III}^0 \dfrac{\partial h}{\partial z}(z,x) - \\ \qquad \dfrac{K_{II}^0}{2\pi} PV \displaystyle\int_{-\infty}^{\infty} \frac{h(x,z') - h(x,z)}{(z'-z)^2} dz' + \delta_y K_I^{skew} \qquad (4.3) \\ \delta_y k_{II}(z,x) = \dfrac{K_I^0}{2} \dfrac{\partial h}{\partial x}(z,x) - \dfrac{2-3\nu}{2-\nu} \dfrac{K_I^0}{2\pi} PV \displaystyle\int_{-\infty}^{\infty} \frac{h(x,z') - h(x,z)}{(z'-z)^2} dz' \\ \delta_y k_{III}(z,x) = \dfrac{2(1-\nu)^2}{2-\nu} K_I^0 \dfrac{\partial h}{\partial z}(z,x) \qquad (4.4) \end{cases}$$

where ν is the Poisson's ratio of the material while $\delta f(z,x)$ and $h(z,x)$ are the in-plane and out-of-plane perturbations respectively. $\delta_y K_I^{skew}$ is a non-local term connected to

Bueckner's skew-symmetric crack-face weight functions (see [Movchan et al., 1998]). The general expression of this non-local term is

$$\delta_y K_1^{skew} = \frac{\sqrt{(2)}}{4\pi}\frac{1-2\nu}{1-\nu} Re\left[\int_{-\infty}^{0} dx' \int_{-\infty}^{\infty} \frac{K_{III}^0 - i(1-\nu)K_{II}^0}{(-x'+i(z-z'))^{3/2s}} \frac{\partial h/\partial z(x',z')}{\sqrt{-x'}} dz'\right]$$

Let us define the following mode mixity ratios :

$$\phi_0 = \frac{K_{II}^0}{K_I^0} \text{ and } \rho_0 = \frac{K_{III}^0}{K_I^0}$$

In the following, we assume $\rho_0, \phi_0 \ll 1$. The crack path is inferred from the double criterion : (i) the local mode II shear $k_{II}(z)$ vanishes everywhere along the crack front and (i) the Griffith criterion $G(z) = G_c(z)$ is satisfied everywhere along the front. These write as:

$$G(x,z) = G_c(x,z) \tag{4.5}$$
$$k_{II}(z,x) = 0 \tag{4.6}$$

The methodology adopted for the linear stability analysis is rather classic. The trivial solution under any ρ_0, ϕ_0 is a planar crack with $\delta f = h = 0$. But under the same loading conditions another solution with a non-zero perturbation amplitude does exist, as I will show in the following. Does the amplitude of this non-trivial mode of crack growth increase or decrease with the propagation distance? To answer this question, we must find out the geometry of the bifurcated mode that satisfies Eqs. (4.5) and (4.6).

4.2 Geometry of the bifurcated modes

Let us assume the following shape:

$$\delta f(z,x) = Re[e^{\lambda x}\psi_x(z)] \tag{4.7}$$
$$h(z,x) = -2\phi_0 x + Re[e^{\lambda x}\psi_y(z)] \tag{4.8}$$

for the bifurcated modes where $\lambda, \psi_x(z), \psi_y(z) \in \mathbb{C}$. Here λ is the growth rate of the perturbation and is inversely proportional to a length scale. The perturbations are allowed to take complex values for an exhaustive stability analysis, however only their real part is considered as the final perturbations are real and $\delta f(z,x)$ and $h(z,x) \in \mathbb{R}$. If $Re[\lambda] > 0$, the perturbation grows and the front will ultimately fragment while if $Re[\lambda] < 0$, the amplitude of the perturbation decreases and the planar propagation is stable. Note the term $-2\phi_0 x$ in the out-of-plane contribution. It emerges from the presence of a macroscopic mode II that uniformly tilts the cracks in the direction $-2\frac{K_{II}^0}{K_I^0}$.

4.3 Principle of local symmetry

Calculations are simplified to a great extent if they are made in the Fourier space. The following formula allows us to compute the Fourier transform of the semi-local term arising in the perturbation of the SIF's

$$\frac{1}{2\pi}PV\int_{-\infty}^{\infty}\frac{Re[g(x,z')]-Re[g(x,z)]}{(z'-z)^2}dz' = Re\left(-\frac{1}{2}\int_{-\infty}^{\infty}|k|\widehat{g(k)}e^{ikz}dk\right) \tag{4.9}$$

where $\widehat{g(k)}$ is the Fourier transform of $g(z)$.

The application of the principle of local symmetry $k_{II}(z,x)=0$ reads

$$k_{II}(z,x) = K_{II}^0 + \delta_x k_{II}(z,x) + \delta_y k_{II}(z,x) = 0$$

Dividing by K_I^0 leads to,

$$\begin{aligned}\implies \phi_0 + \frac{1}{2}\frac{\partial h}{\partial x}(z,x) - \frac{2-3\nu}{2-\nu}\frac{1}{2\pi}PV\int_{-\infty}^{\infty}\frac{h(x,z')-h(x,z)}{(z'-z)^2}dz' + \\ \frac{2-3\nu}{2-\nu}\frac{\phi_0}{2\pi}PV\int_{-\infty}^{\infty}\frac{\delta f(x,z')-\delta f(x,z)}{(z'-z)^2}dz' - \frac{2}{2-\nu}\rho_0\frac{\partial \delta f}{\partial z}(z,x) = 0\end{aligned}$$

We now use the geometry of the bifurcated mode assumed in equations (4.7) and (4.8). We see that the constant ϕ_0 is immediately canceled due to the presence of the term $-2\phi_0 x$ in the perturbation mode. The net $k_{II}(z,x)$ thus is written as

$$\begin{aligned}k_{II}(z,x) = \frac{1}{2}Re\left[\lambda e^{\lambda x}\psi_y(z)\right] - \frac{2-3\nu}{2-\nu}\frac{1}{2\pi}PV\int_{-\infty}^{\infty}\frac{Re[e^{\lambda x}\psi_y(z)]-Re[e^{\lambda x}\psi_y(z)]}{(z'-z)^2}dz' + \\ \frac{2-3\nu}{2-\nu}\frac{\phi_0}{2\pi}PV\int_{-\infty}^{\infty}\frac{Re[e^{\lambda x}\psi_x(z)]-Re[e^{\lambda x}\psi_x(z)]}{(z'-z)^2}dz' - \frac{2}{2-\nu}\rho_0 Re\left[e^{\lambda x}\frac{\partial\psi_y(z)}{\partial z}(z)\right]\end{aligned}$$

Using the lemma (4.9) the above equation simplifies as:

$$\begin{aligned}k_{II}(z,x) = Re\Bigg\{e^{\lambda x}\Bigg[\frac{\lambda}{2}\int_{-\infty}^{\infty}\widehat{\psi_y(k)}e^{ikz}dk + \frac{2-3\nu}{2-\nu}\frac{1}{2}\int_{-\infty}^{\infty}|k|\widehat{\psi_y(k)}e^{ikz}dk \\ - \frac{2-3\nu}{2-\nu}\frac{\phi_0}{2}\int_{-\infty}^{\infty}|k|\widehat{\psi_x(k)}e^{ikz}dk - \frac{2}{2-\nu}\rho_0\int_{-\infty}^{\infty}ik\widehat{\psi_x(k)}e^{ikz}dk\Bigg]\Bigg\} = 0\end{aligned}$$

where $\widehat{\psi_x}$ and $\widehat{\psi_y}$ are the Fourier transform of ψ_x and ψ_y respectively. Simplifying further leads to

$$Re\left\{e^{\lambda x}\int_{-\infty}^{\infty}e^{ikz}\left[\frac{\lambda}{2}\widehat{\psi_y(k)}+\frac{2-3\nu}{2-\nu}\frac{1}{2}|k|\widehat{\psi_y(k)}-\frac{2-3\nu}{2-\nu}\frac{\phi_0}{2}|k|\widehat{\psi_x(k)}-\frac{2}{2-\nu}\rho_0 ik\widehat{\psi_x(k)}\right]dk\right\} = 0$$

We are now in a position to relate the in-plane and the out-of-plane perturbations of the bifurcated mode. First we use the following property that if $\mathrm{Im}(\lambda) \neq 0$

$$Re\left[Ae^{\lambda x}\right] = 0 \quad \forall x \Longrightarrow A = 0 \tag{4.10}$$

It follows,

$$\left(\frac{-2i}{2-\nu}\rho_0 k - \frac{1}{2}\frac{2-3\nu}{2-\nu}\phi_0|k|\right)\widehat{\psi_x(k)} + \left(\frac{\lambda}{2} + \frac{1}{2}\frac{2-3\nu}{2-\nu}|k|\right)\widehat{\psi_y(k)} = 0$$

Thus, the in-plane and the out-of-plane perturbations in the Fourier space are related as

$$\boxed{\widehat{\psi_y(k)} = \frac{4i\rho_0 \mathrm{sgn}(k) + (2-3\nu)\phi_0}{2-3\nu+(2-\nu)\xi}\widehat{\psi_x(k)}} \tag{4.11}$$

where

$$\xi = \frac{\lambda}{|k|}$$

is a dimensionless parameter which provides the normalized growth rate of the bifurcated mode defined as the ratio of the growth rate λ to the wavenumber $|k|$.

4.4 Calculation of the change in the energy release rate δG and mode-mixity $\delta\rho$

Before applying the criterion based on energy balance, we first derive a couple of useful relations

4.4.1 Perturbations of the energy release rate δG

The energy release rate for an unperturbed crack is given by the Irwin formula as :

$$G^0 = \frac{1-\nu^2}{E}\left(K_I^{0\,2} + {K_{II}^0}^2\right) + \frac{1+\nu}{E}{K_{III}^0}^2 \simeq \frac{1-\nu^2}{E}K_I^{0\,2} \text{ for } K_{III}^0, K_{II}^0 \ll K_I^0$$

For a perturbed crack, the variation in the energy release rate follow

$$G_0 + \delta G = \frac{1-\nu^2}{E}\left((K_I^0 + \delta k_I)^2 + (K_{II}^0 + \delta k_{II})^2\right) + \frac{1+\nu}{E}(K_{III}^0 + \delta k_{III})^2$$

From the principle of local symmetry, we have $K_{II}^0 + \delta k_{II} = 0$. In this calculation we ignore terms which are of the order ρ_0^2 or ϕ_0^2 or $\rho_0\phi_0$ as we have assumed small shear mode $\rho_0, \phi_0 \ll 1$. This allows us to simplify to

$$G_0 + \delta G = G^0 + 2\frac{1-\nu^2}{E}\delta k_I K_I^0$$

Normalizing w.r.t the unperturbed energy release rate, we obtain

$$\frac{\delta G}{G_0} = 2\frac{\delta k_I}{K_I^0} \tag{4.12}$$

The perturbation in the mode I stress-intensity factor writes as

$$\delta k_I(z,x) = \delta_x k_I(z,x) + \delta_y k_I(z,x)$$

where $\delta_x k_I(z,x)$ and $\delta_y k_I(z,x)$ are given by equations (4.2) and (4.3). Notice that all the terms in $\delta_y k_I(z,x)$ are of the order of ρ_0^2 or $\rho_0\phi_0$. Hence we simplify by ignoring the term $\delta_y k_I(z,x)$. This gives $\delta k_I(z,x) = \delta_x k_I(z,x) = \frac{K_I^0}{2\pi} PV \int_{-\infty}^{\infty} \frac{\delta f(x,z') - \delta f(x,z)}{(z'-z)^2} dz'$. Continuing from equation (4.12), the perturbation in energy release rate is

$$\frac{\delta G}{G_0} = \frac{1}{\pi} PV \int_{-\infty}^{\infty} \frac{Re[e^{\lambda x}\psi_x(z')] - Re[e^{\lambda x}\psi_x(z)}{(z'-z)^2} dz'$$

that can be written in terms of the Fourier transform of the perturbation as

$$\boxed{\frac{\delta G}{G_0} = Re\left(-e^{\lambda x}\int_{-\infty}^{\infty} |k|\widehat{\psi_x(k)}e^{ikz}dk\right)} \tag{4.13}$$

4.4.2 Perturbations of the mode-mixity ratio $\delta\rho$

The mode mixity ratio in (I + III) defined as earlier is

$$\rho(z,x) = \frac{k_{III}(z,x)}{k_I(z,x)}$$

The variation in the mode-mixity ratio due to the crack front perturbations is

$$\delta\rho = \delta\left(\frac{k_{III}(z,x)}{k_I(z,x)}\right) = \frac{\delta k_{III}}{K_I^0} - K_{III}^0\frac{\delta k_I}{K_I^0} = \frac{\delta k_{III}}{K_I^0} - \rho_0\frac{\delta k_I}{K_I^0}$$

Again using the perturbation formulae of the stress-intensity factors given in equations (4.2) - (4.4), we express the variations in the mode-mixity ratio as a function of geometrical perturbation of the crack. This calculation is quite lengthy so we only give the final result which reads as

$$\boxed{\delta\rho = Re\left[e^{\lambda x}\int_{-\infty}^{\infty} |k|\widehat{\psi_x(k)}e^{ikz}dk\frac{-(4-5\nu+\nu\xi)\rho_0 + 2(1-\nu)(2-3\nu+\xi)i\phi_0\mathrm{sgn}(k)}{(2-3\nu)+(2-\nu)\xi}\right]} \tag{4.14}$$

4.5 Application of the Griffith criterion

We use the above derived formulae to enforce the Griffith's criterion $G(z,x) = G_c(z,x)$ everywhere along the crack front. The perturbations in the energy release rate and the fracture energy can be written as

$$\left.\begin{aligned} G(z,x) &= G^0 + \delta G(z,x) \\ G_c(z,x) &= G_c(\rho_0) + \frac{d(G_c)}{d\rho}(\rho_0)\delta\rho(z,x) \end{aligned}\right\}$$

At order 0, the unperturbed energy release rate is equal to the average fracture energy, i.e. $G^0 = G_c(\rho_0)$. Thus, the Griffith criterion simplifies at first order as :

$$\delta G(z,x) = \frac{dG_c}{d\rho}(\rho_0)\delta\rho(z,x)$$

Normalizing w.r.t G^0 and rearranging the terms, we can write it as

$$\frac{\delta G(z,x)}{G^0} - \frac{d(lnG_c)}{d\rho}\delta\rho(z,x)$$

Having derived the expressions of perturbation in the energy release rate δG and mode mixity $\delta\rho$ substituting equations (4.14) and (4.13) in the above equation

$$Re\Bigg\{ e^{\lambda x}\int_{-\infty}^{\infty} |k|\widehat{\psi_x(k)}e^{ikz}dk\Bigg[-1 + \frac{d(lnG_c)}{d\rho}\times \\ \frac{-(4-5\nu+\nu\xi)\rho_0 + 2(1-\nu)(2-3\nu+\xi)i\phi_0\mathrm{sgn}(k)}{(2-3\nu)+(2-\nu)\xi}\Bigg]\Bigg\} = 0$$

Using the lemma (4.10), the terms inside the square brackets [...] must vanish.

Thus we have,

$$\frac{d(lnG_c)}{d\rho}\frac{-(4-5\nu+\nu\xi)\rho_0 + 2(1-\nu)(2-3\nu+\xi)i\phi_0\mathrm{sgn}(k)}{(2-3\nu)+(2-\nu)\xi} = 1$$

This condition gives a relation between the normalized growth rate $\xi = \lambda/|k|$ and the mode-mixity ratios ϕ_0 and ρ_0. Simplifying the above equation by substituting $G_c(\rho) = G_c^I(1+\gamma\rho^\kappa)$ and rearranging the terms to extract the normalized growth rate one obtains

$$\xi = \frac{N_1 + iN_2}{D_1 + iD_2} \Longleftrightarrow \varphi(\rho_0,\phi_0,\xi) \equiv \xi - \frac{N_1 + iN_2}{D_1 + iD_2} = 0$$

where

$$\begin{aligned} N_1 &= -(2-3\nu) + A(4-5\nu) & & & D_1 &= 2-\nu-A\nu \\ N_2 &= -2A(1-\nu)(2-3\nu)\frac{\phi_0}{\rho_0}s & \text{and} & & D_2 &= 2A(1-\nu)\frac{\phi_0}{\rho_0}s \\ A &= \frac{\kappa\gamma\rho_0^\kappa}{1+\gamma\rho_0^\kappa} & & & s &= sgn(k) \end{aligned} \tag{4.15}$$

Thus, identifying bifurcated solutions amounts to search for values of ξ which satisfy $\varphi(\rho_0,\phi_0,\xi) = 0$ i.e.

$$\boxed{\varphi(\rho_0, \phi_0, \xi) = \xi - \frac{N_1 D_1 + N_2 D_2 + i(-N_1 D_2 + N_2 D_1)}{D_1^2 + D_2^2} = 0} \tag{4.16}$$

Under some fixed loading conditions ϕ_0, ρ_0, the planar crack propagation is unstable if there exists a competing crack growth mode with an exponentially growing amplitude. As a results the condition $Re(\xi) = 0$ provides the onset of the fragmentation instability. In the following we show that for some large values of the shear loading ϕ_0, ρ_0 such an unstable solution does exist

Thus to look for the instability, we need to look for solutions for which $Re(\xi) > 0$ as their amplitude would grow exponentially. Thus, do there exist material parameters γ, κ , ν and loading conditions ρ_0 and ϕ_0 for which $Re(\xi) > 0$. As we show in the following, it does exist and this solution is unique.

4.5.1 Unstable bifurcated mode

Having five parameters, we fix two of them in the analysis presented henceforth. First, we fix $\nu = 0.37$, which is the Poisson's ratio of PMMA used in our experiments; then we choose the power κ as an even number. As a positive or a negative value of same ρ should result in the same value G_c we take $\kappa = 2$ is the smallest even power which will contribute more than terms applied in ρ^4, ρ^6 etc as small values of ρ are considered. Figure 4.2 shows the variation of $Re[\xi]$ as a function of the mode mixity ratio ρ_0. For values of ρ_0 beyond a critical threshold a positive solution to $Re(\xi)$ exists. We now investigate the effect of γ that describes the dependence of G_c with mode mixity ($\gamma = 0$ leading to a fracture energy independent of ρ_0). As γ increases, the threshold ρ_c beyond which a growing bifurcated mode exist, reduces to very low values and as we increase the value of ϕ_0, the threshold increases.

4.5.2 Critical mode III mixity

One can now determine the critical mode III mixity ratio corresponding to the onset of fragmentation by solving for the equation (4.16) $Re[\xi] = 0$. Thus for $\rho_0 = \rho_c$, the critical mode mixity ratio is given by

$$Re[\xi] = 0 \Longrightarrow N_1 D_1 + N_2 D_2 = 0$$

Substituting for N_1, N_2, D_1, D_2

$$\boxed{[2 - 3\nu - A(4 - 5\nu)](2 - \nu - A\nu) + 4A^2(1 - \nu)^2(2 - 3\nu)\frac{\phi_0^2}{\rho_c^2} = 0 \text{ where } A = \frac{\kappa\gamma\rho_c^\kappa}{1 + \gamma\rho_c^\kappa}}$$

For $\kappa = 2$, this equation is a polynomial of second order in ρ_c^2 and can be solved analytically. The critical ratio ρ_c for different values of ϕ_0 and $\nu = 0.37$ as a function of γ is shown in Figure 4.3. For large values of γ and a small amount of mode II, the critical threshold is really small, of the order of a few percents.

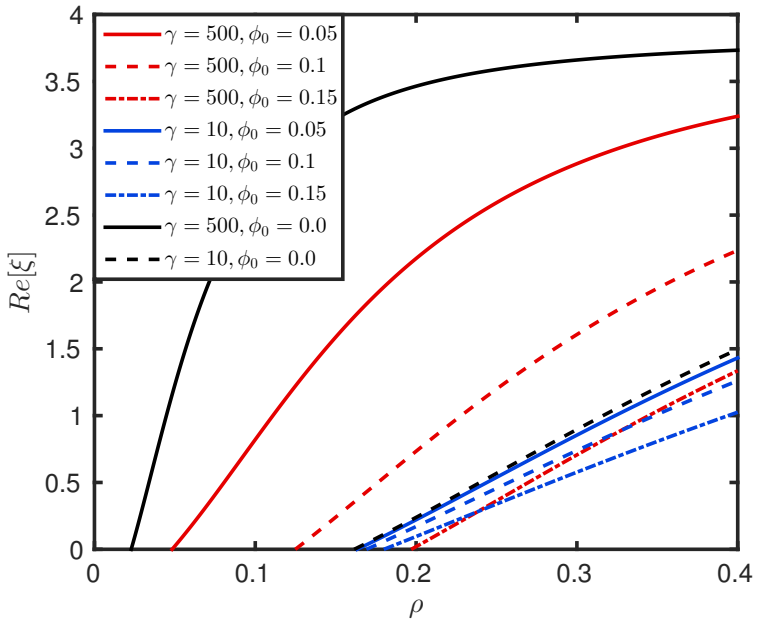

Fig. 4.2 *Normalized growth rate ξ that informs about the stability as a function of the applied mode III ρ_0 for different material parameters and applied mode II mixity ratio ϕ_0. Here we $\nu = 0.37$ (for PMMA) and $\kappa = 2$. When γ is large, notice that the threshold is lower. Note also the effect of mode II which tend to stabilize the front. The black curve corresponds to $\phi_0 = 0$ which is the solution derived in Leblond et al. [in prep.] under mode I + III only.*

4.6 Shape of the unstable bifurcated mode

Knowing that an unstable bifurcated mode exists, we now look at its geometry. Let us first study the case when $\rho_0 > \rho_c$.

Case 1: $\rho_0 > \rho_c$

We have already shown in the previous section that beyond the threshold, there is a unique solution for ξ given by Eq (4.16)

$$\xi = \xi_1 + i\xi_2 \quad \text{where} \quad \xi_1 = \frac{N_1 D_1 + N_2 D_2}{D_1^2 + D_2^2} \quad \text{and} \quad \xi_2 = \frac{-N_1 D_2 + N_2 D_1}{D_1^2 + D_2^2} \tag{4.17}$$

For this value of $\xi = \frac{\lambda}{|k|}$ corresponds an infinite number of bifurcated modes with growth rate given by $\lambda = |k|\xi$. It can be verified that for positive or negative k leads to the same geometry of the unstable mode and hence in the following we assume $k > 0$ leading to,

$$\lambda = \xi_1 k + i\xi_2 k$$

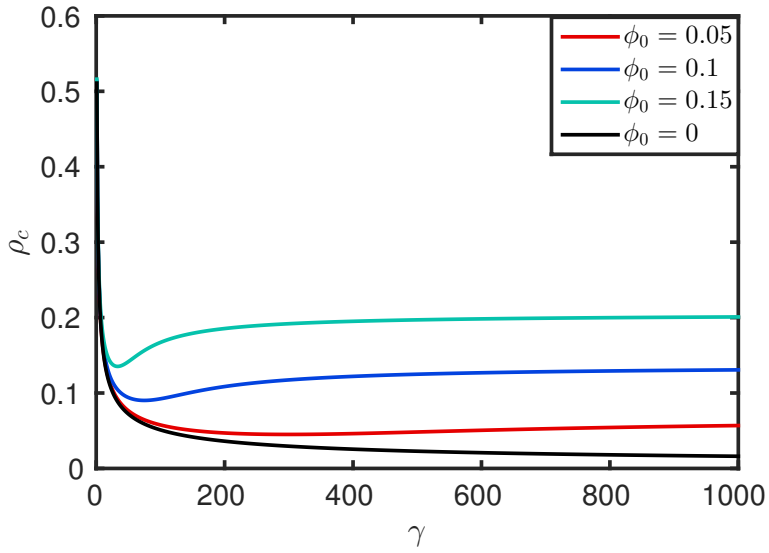

Fig. 4.3 *Critical mode III mixity ratio ρ_c as a function of the parameter γ . For large values of γ and small amount of mode II ϕ_0, the value of ρ_c is really small, of the order of a few percents*

The Fourier transform of the perturbation in z, $\psi_x(z)$ must be a dirac function of the form:

$$\widehat{\psi_x(k')} = Ce^{i\theta}\delta(k'-k) = Ce^{i\theta}\delta(k'-k)$$

where $C \in \mathbb{R}$.

Taking the inverse Fourier transform,

$$\psi_x(z) = \int_{-\infty}^{\infty} \widehat{\psi_x(k')} e^{ik'z} dk' = Ce^{i\theta}e^{ikz}$$

Thus, the in-plane geometry shape of the bifurcated mode follows

$$\delta f(z,x) = Re[e^{\lambda x}\psi_x(z)] = Re[e^{\xi_1 x}e^{i\xi_2 x}Ce^{i(kz+\theta)}]$$

$$\Longrightarrow \boxed{\delta f(z,x) = Ce^{\xi_1 x}\cos[k(z+\xi_2 x)+\theta]}$$

Using the relation between the in-plane and the out-of-plane displacements ψ_x and ψ_y presented in equation (4.11) we evaluate the Fourier transform of ψ_y as

$$\widehat{\psi_y(k)} = \frac{4i\rho_0 \mathrm{sgn}(k) + (2-3\nu)\phi_0}{2-3\nu+(2-\nu)(\xi_1+i\xi_2)}\widehat{\psi_x(k)}$$

Simplifying, the denominator one gets

$$\widehat{\psi_y(k)} = (b-ia)\widehat{\psi_x(k)}$$

where

$$\begin{cases} b = \dfrac{(2-3\nu)\phi_0[2-3\nu+(2-\nu)\xi_1]+4(2-\nu)\xi_2\rho_0}{[(2-3\nu+(2-\nu)\xi_1)]^2+[(2-\nu)\xi_2]^2} & (4.18) \\ a = \dfrac{(2-\nu)(2-3\nu)\xi_2\phi_0-4\rho_0[2-3\nu+(2-\nu)\xi_1]}{[(2-3\nu+(2-\nu)\xi_1)]^2+[(2-\nu)\xi_2]^2} & (4.19) \end{cases}$$

Taking the inverse Fourier transform,

$$\psi_y(z) = \int_{-\infty}^{\infty} \widehat{\psi_y(k')} e^{ik'z} dk' = \int_{-\infty}^{\infty} (b-ia)Ce^{i\theta}\delta(k'-k)e^{ik'z}dk' = (b-ia)Ce^{i\theta}e^{ikz}$$

Thus the geometry of the out-of-plane mode (after subtraction of the average plane in the kink angle direction $-2\phi_0$) is

$$\delta h(z,x) = h(z,x) + 2\phi_0 x = Re[e^{\lambda x}\psi_y(z)] = Re[e^{\xi_1 x}e^{i\xi_2 x}(b-ia)Ce^{i\theta}e^{ikz}]$$

$$\Longrightarrow \boxed{\delta h(z,x) = Ce^{\xi_1 kx}[a\sin(k(z+\xi_2 x)+\theta)+b\cos(k(z+\xi_2 x)+\theta)]}$$

Thus the bifurcated modes are elliptical helices, however the major and minor axes of these helices are not exactly along Ox and Oz. Let's consider a small rotation $\eta \ll 1$ along the z-axis, so that

$$\begin{aligned} \bar{\delta f} &= \delta f + \eta\delta h \\ \bar{h} &= -\eta\delta f + \delta h \end{aligned}$$

Ignoring the term $\eta\delta h$ that is proportional to ρ_0^2 or ϕ_0^2 or $\rho_0\phi_0$ in the rotated reference frame, the geometry of the unstable modes reads

$$\left.\begin{aligned} \bar{\delta f} &= Ce^{\xi_1 x}cos[k(z+\xi_2 x)+\theta] \\ \bar{h} &= aCe^{\xi_1 x}sin[k(z+\xi_2 x)+\theta] \end{aligned}\right\}$$

Thus from a small rotation in the axes, we've obtained the standard equations of an elliptic helix. A plot of the fragmented mode is shown in Figure 4.4.
Now we draw some important conclusions about the geometry of the helicoidal bifurcated mode:

4.6.1 Conclusions for $\rho_0 > \rho_c$

- The geometry of the growing unstable mode is found to be an elliptic helix. In the analysis of [Leblond et al., 2011], where the dependency of G_c with the mode mixity ratio is neglected, the bifurcated crack shape was assumed a priori to be an elliptic helix. This was motivated by the phase-field results of Pons and Karma [2010] who found out that the unstable mode can be parameterized by an elliptic helix.

- The axis of the elliptic helix are not exactly in the direction of Ox and Oy, but are slightly tilted to the Z-axis. This effect results from the macroscopic mode II. If we now assume $\phi_0 = 0$, one then observes in eq (4.19) and (4.18) that $b = 0$ but $a \neq 0$ and the equation is an elliptic without the necessity of any rotation.

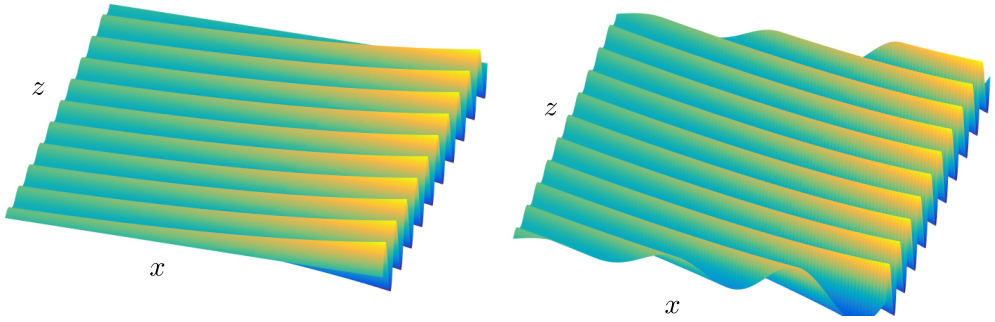

Fig. 4.4 *(a) Geometry of the bifurcated mode for $\phi_0 = 0$ and (b) a non-zero ϕ_0. Notice that the modes are exponentially growing and for a non-zero mode II, there is a drift along z-axis*

- As x increases, the amplitude of both the in-plane and out-of-plane bifurcated modes increase exponentially and are proportional to $e^{k\xi_1 x}$ where ξ_1 is fixed by the material properties (ν, γ, κ) and the loading conditions ϕ_0 and ρ_0.

- An another very interesting property we observe is that the argument in the cosine and the sine terms are dependent on both z and x. Thus as x increases, the leading points of the helix are translated along z, thus the helix also has a translatory motion (highlighted in Fig. 4.4). Observed from the top, this results in a drift of angle given by $\frac{dz}{dx} = -\xi_2$. This is again due to the presence of mode II as $\xi_2 \propto \phi_0$ (see equation (4.15) and (4.17)).

- If we now take $\gamma = 0$, corresponding to a fracture energy that is independent on the mode-mixity ratio ρ, one obtains from equation (4.15) $N_2 = 0$ and $D_2 = 0$ and again $\xi_2 = 0$. Thus, if the fracture energy is not a function of mode-mixity, we do not predict any drift of the elliptic helix along z. As a result, translation of the unstable mode emerges from a mode-III dependent fracture energy and a non-zero mode II.

- In our experiments (see Chapter 1), we observe that the sides of the triangular fracture patterns drift with some finite angle from the direction of propagation. Is this a proof of the existence of a small amount of mode II and a shear-dependent fracture energy ? Let us find out in the next chapter where we make quantitative comparisons with experiments.

4.6.2 Case 2: $\rho_0 = \rho_c$

If $\rho_0 = \rho_c$, then $\xi = 0$ and so $\lambda = 0$. This means that the in-plane and the out-of-plane perturbations are now independent of x. As $\lambda = 0$, k can take any arbitrary value and thus the in-plane perturbation can be arbitrary. However fixing one of the perturbations fixes the other perturbation as both functions are related by eq (4.11).

Derivation of the perturbation in mode-mixity $\delta\rho$ for $\rho_0 = \rho_c$

We finally derive another important result that concerns perturbations which are independent of x, i.e perturbations which are stationary. The mode-mixity ratio $\delta\rho$ is given by the equation (4.14) as

$$\delta\rho = Re\left[e^{\lambda x}\int_{-\infty}^{\infty}|k|\widehat{\psi_x(k)}e^{ikz}dk\frac{-(4-5\nu+\nu\xi)\rho_0+2(1-\nu)(2-3\nu+\xi)i\phi_0 sgn(k)}{(2-3\nu)+(2-\nu)\xi}\right]$$

We use equation (4.11) to write it as a function of the out-of-plane perturbations. We take the inverse Fourier and present here the final result as

$$\delta\rho = -\frac{\rho_0\phi_0(2-3\nu)(4-3\nu)}{(2-3\nu)^2\phi_0^2+16\rho_0^2}\frac{1}{\pi}PV\int_{-\infty}^{\infty}\frac{\delta h(z')-\delta h(z)}{(z'-z)^2}dz+ \frac{2(2-3\nu)^2(1-\nu)\phi_0^2+4(4-5\nu)\rho_0^2}{(2-3\nu)^2\phi_0^2+16\rho_0^2}\frac{\partial\delta h}{\partial z}$$

where $\delta h = h + 2\phi_0 x$.

This relation is quite handy as it does not relation on any assumption on the geometry of the perturbation, except for the fact that the perturbations should not depend on x. This relation will be used in the next chapter to decipher the triangular fracture patterns.

4.7 Conclusions

In this chapter we have studied the transition of a planar crack to a fragmented crack under small amounts of mode II and mode III and a fracture energy depending on mode III. The following conclusions are drawn from this analysis:

- The critical threshold for the transition varies with the material parameters γ and κ which describe how G_c depends on ρ. For high values of γ, that correspond to a strong increase of G_c with ρ, the critical threshold for fragmentation is found to lower to the order of a few percents. Mode II also has a significant effect on the threshold and as the value of mode II increases, this threshold increases.

- The shape of the bifurcated mode is found to be an elliptic helix. In the previous analysis of Leblond et al. [2011] for a fracture energy independent of ρ, the shape was a priori assumed to be a elliptic helix.

- The ellipsoidal helix drifts along the z-axis at an angle ξ_2 and emerges due to both the amount of mode II and the dependence of $G_c(\rho)$. If one of these ingredients is missing, the bifurcated mode is not expected to drift.

Chapter 5

How to decipher triangular patterns on fracture surface of PMMA

Contents

In this chapter, we now use the theoretical models presented in Chapters 3 and 4 to interpret the experimental triangular patterns formed on PMMA fracture surfaces. At first we describe and quantify the geometry of these patterns that are subsequently compared to model predictions.

5.1 Triangular fracture pattern

Figure 5.1 shows optical images of a characteristic surface of a TDCB sample of PMMA obtained using Lleica microsystems microscope. Figure 5.1 (a) shows first the whole fracture surface of the broken specimen. We remind that the experiments are carried out under dominantly mode I loading conditions. The crack initiates at high velocity (typically in the range 100-200 ms^{-1} decelerating down to 0.1 mms^{-1} leaving two regions on the fracture surface with strikingly different geometries. At large velocities ($v > v_c$ where $v_c = 15$ mms^{-1}), the fracture surface is optically smooth while at lower speeds ($v < v_c$), the crack seems to form elongated features (also referred to as 'plumes') that

aligns with the local propagation direction of the crack. Fig. 5.1 (b) shows a zoom of the transition region where the fracture surface changes from smooth to rough. Surprisingly, we see that the plumes observed in the region where the roughness is fully developed initiates by the formation of triangles. A typical fracture surface (the width of which is 8 mm) shows about 8 to 10 of them. Figure 5.1(c) shows a zoom of one of these triangular patterns. It can be characterized by an angle β which varies between 15 and 20 ^{o}.

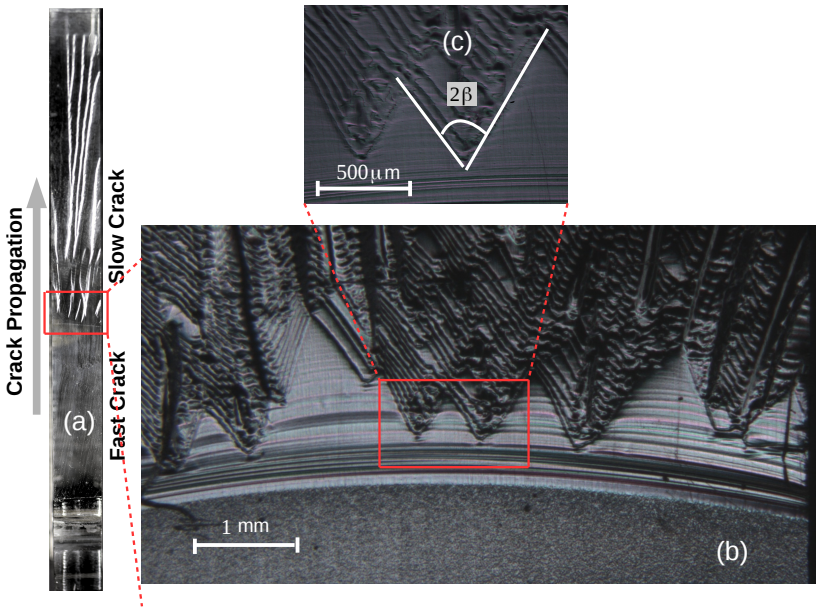

Fig. 5.1 *Morphology of fracture surfaces: (a) Whole fracture surface of a TDCB specimen of PMMA (see chapter 2). The crack spreed goes here from* 200ms^{-1} *at initiation (lower part of the specimen) down to* 0.1 mms^{-1} *at the upper end of the specimen right before it is fully broken. Note the transition from optically smooth to rough as the crack speed decelerates under* $v_c \simeq 15$ mms^{-1}*;(b) shows the transition region between fast and slow speeds where the triangular patterns are formed; (c) Zoom on one of the triangles where* β *defines the half-angle of the triangle*

5.2 Crack front deformation in the vicinity of the triangular patterns

Before the triangles may form, one can clearly see crack front lines of parabolic shape normal to the triangles. In this zone, the crack goes through tremendous deceleration, typically from $50 - 100$ ms^{-1} to 10 mms^{-1} in a matter of μs leading to decelerations of the order of $10^6 ms^{-2}$ (refer to Section 2.3.3 for more details). These lines look strikingly similar to the Wallner lines which are let on fracture surfaces due to the interaction between the crack front and a shear wave produced by a secondary source [Bonamy and Ravi-Chandar, 2003, Wallner, 1939]. We consider these lines as snapshots of the crack

front at a given instant of time. If we look at these lines in the vicinity of the triangles (Fig. 5.2), we see that the crack front is perturbed by the presence of the triangle, showing a U-shape similar to that of a crack front pinned by a tough obstacle [Chopin et al., 2011, Dalmas et al., 2009].

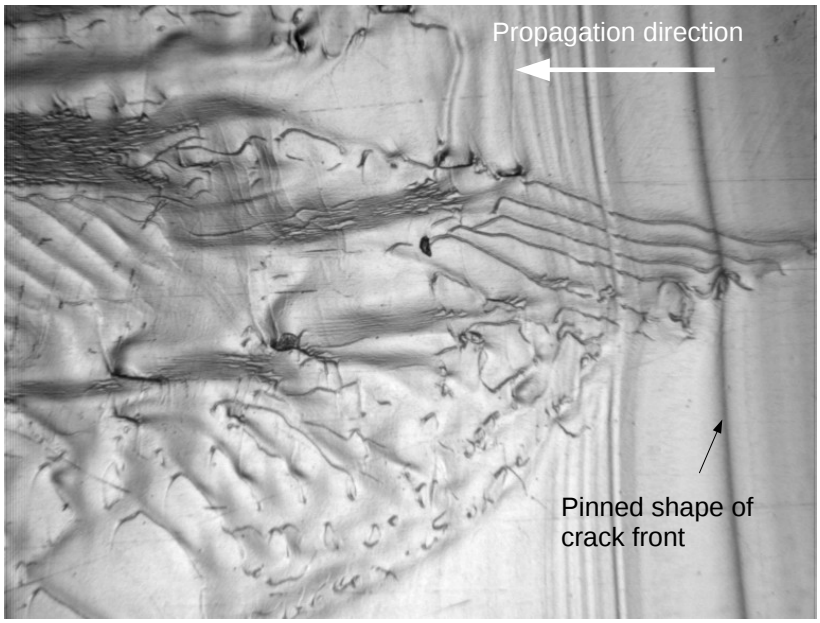

Fig. 5.2 *Snapshot of the perturbed crack front at the vicinity of a triangular pattern*

The pinned shape of the crack front gives us a hint that the fracture energy inside the triangle is higher. In section 3.2.2, we addressed theoretically the problem of a crack front pinned by a triangular obstacle of higher toughness and we apply it here to rationalize the experimentally observed pinned shape of the crack front. To recapitulate, the solution depends on two parameters, the fracture energy contrast, C, of the obstacle and the rate ϵ at which the width of the triangle increases in comparison to a characteristic velocity v_0 of the crack. This value of ϵ is related to the angle of the triangle as $\epsilon = \gamma \tan(\beta)$, where γ is the power in $G_c(v) \sim v^\gamma$ and β, the angle of the triangle.

From image analysis, we extract different front shapes at different positions $f(x, z)$ as the crack penetrates deeper in the triangular region. If we plot $g = \frac{\delta f(z,x)}{d(x)} = \frac{f(x,z)-f(x,0)}{d(x)}$ as a function $u = \frac{z}{d(x)}$, we find that the crack profiles collapse well as shown in Fig. 5.3. The theoretical shape depends on two parameters, the toughness contrast, C and the parameter ϵ proportional to the angle of the triangle. For our experiments, the exponent characterizing the kinetic law $G_c(v)$, $\gamma \sim 0.2$ (see Section 2.2.6) and the angle of the triangle is β are known. The value of $\epsilon \simeq 0.05 - 0.07$ is really small so that the theoretical prediction $\delta f(z, x)$ is almost the same as the one of an obstacle of constant width (See Fig. 3.3). Fixing $\epsilon \sim 0.05$, the experimentally measured front shape is now fit with the theoretical predicted shape with just one adjustable parameter, the toughness contrast C. Applying this procedure for different triangles and different experiments, we do not find a large variation in the toughness contrast and the value remains in the range

Sample name	Initial driving force (G_{ini})	Contrast (C)	Angle $\beta(^o)$
E06 (Erinome)	654	0.15	13.5
E07 (Thelxinoe)	597	0.16	14.6
E09 (Palliaq)	616	0.227	15.7
E10 (Suttungr)	551	0.254	13.8
E13 (Bergelmir)	400	0.27	16
E18 (Parvati)	777	0.231	12.5
E18 (Shiva)	777	0.255	12.83

Table 5.1 – The measurement of contrast, C, angle of the triangle, β as a function of initial elastic energy release rate G_{ini}

$C \sim 0.15-0.25$. For different experiments, table 5.1 provides the contrast value extracted from this procedure together with the angle β of the triangle as a function of the initial elastic energy release rate G_{ini}. We do not evidence any clear correlations between these three quantities.

5.3 Out-of-plane shape of the triangle

From the pinned shape of the crack front, we conclude that the effective fracture energy inside the triangular region must be slightly higher (typically (1+C) = 1.2 times) larger than outside the triangle. But what causes the fracture energy inside the triangle to be

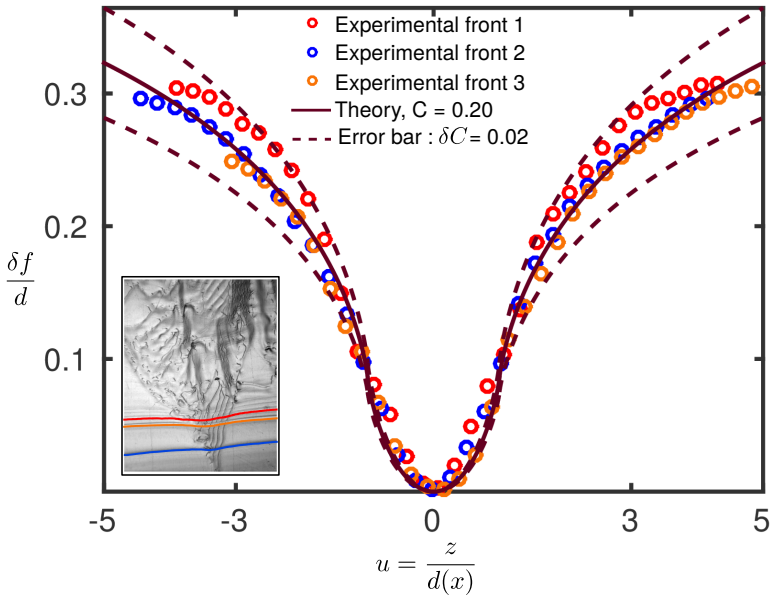

Fig. 5.3 *Collapse of the in-plane front shape when normalized w.r.t the triangular width $d(x)$ and its comparison with the theoretical prediction for a crack pinned by a triangular obstacle*

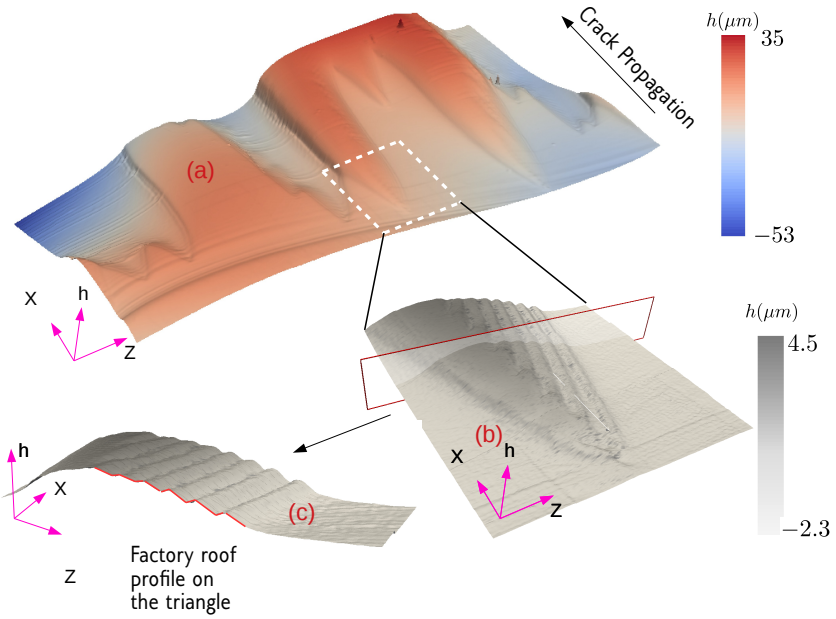

Fig. 5.4 *Out-of-plane profile of the fracture surface close to the transition region: (a) Full width (8mm) showing all the triangles formed (b) Zoom of one of the triangles and (c) cut made corresponding to the section shown in (b) across the triangle. The factory roof profile can be clearly seen and is shown in red. The out-of-plane values are scaled by 15 times for better visualization.*

higher ? To find out this, we look at the out-of-plane deviations of the fracture surface using an interferometric based profilometer (Bruker Contour GT-K) that provides the height map of the fracture surface with a precision of a few orders of nm in height and 2μm lateral spacing. The out-of-plane shape of the fracture surface in the transition region is shown in Figure. 5.4.

From the picture, we observe some important features:

- The triangular region inside shows a small bump, the amplitude of which is increasing as the crack propagates. This bump is not symmetric as it seems to shift to one side of the triangle (See Fig. 5.4 (b)).
- On this bump, we see step like features which run parallel to the side of the triangle. These steps seem to be reminiscent of the factory roof profile emerging from the Mode (I + III) fragmentation instability [Cooke and Pollard, 1996, Hull, 1994, Lazarus et al., 2008, 2001, Sommer, 1969, Yates and Miller, 1989](See Fig. 5.4 (c)). These steps drift along z with the same angle as the one of the triangle.

In the following sections, we decipher these patterns and discuss the mechanisms leading to such a roughening transition. We first try to explain the overall out-of-plane growth of the triangle (assuming a small perturbation of the crack front) and then determine the origin of this in-plane perturbation, what triggers this roughening instability and how these patterns are formed in a self-sustained way is finally discussed at the end of the chapter.

5.3.1 Out-of-plane growth of the triangle

To understand the out-of-plane shape of the triangle, we assume a small amount of mode II and mode III, despite our mechanical test being performed under imposed tensile loading conditions. We assume that they are small in comparison to mode I and that they result from a slight misalignment of the mechanical loading imposed to the specimen. Mode II has a tendency to kink the crack [Gol'dstein and Salganik, 1974] while mode III causes it to twist [Pollard et al., 1982]. At this point we are just interested in the out-of-plane shape of the triangle, we assume that a triangular region of higher toughness already exists and that the crack has already entered into the triangle[1]. In such conditions, the shape of the crack front is perturbed (See section 3.2.2) due to pinning by the triangular obstacle. It was seen in section 3.3 that a perturbed crack subjected to a small amount of mode II and mode III will kink and twist non-uniformly. The problem of a crack pinned by a triangular obstacle and subject to small amounts of mode II and mode III has been studied theoretically in chapter 3 (see Section 3.6). We now compare our theoretical results predictions with the the experimental pattern seen on the PMMA fracture surface. The theoretical out-of-plane shape of the triangle depends on several parameters *viz.*: the toughness contrast C, the mode II mixity ratio $\phi_0 = \frac{K^0_{II}}{K^0_I}$, the mode III mixity ratio $\rho_0 = \frac{K^0_{III}}{K^0_I}$ and angle of the triangle, β (See section 3.6). The toughness contrast C has already been estimated from the in-plane deformation of the front while the angle β of the triangle, has been measured from their optical pictures. This leaves us with two unknown parameters in the theoretical out-of-plane shape which are the two mode mixity factors, ϕ_0 and ρ_0. We now present two independent procedures to extract the value of these parameters from the comparison with theory and experimental out-of-plane profiles.

Method 1 : Normalization of the out-of-plane profiles

The scan of the fracture surface provides a height map h(x,z) that corresponds to successive out-of-plane configurations of the crack. We first define $\delta h(x,z) = h(x,z) - h(x,0)$ (see Figure 5.5) that we normalize using the obstacle width $d(x)$. The out-of-plane front shape corresponding to different positions x collapse very well (see Fig. 5.5). This collapse is predicted by the theory. We then define a master curve $\frac{\delta h(z,x)}{d(x)}$ that depends on z only by computing the average of the renormalized positions corresponding to different values in the range $200\mu\text{m} < x < 800\mu\text{m}$ that corresponds to the two white lines shown in Fig. 5.6(a). Interestingly one can observe that the minimum value of $\delta h(u)$ is not at the centre but is slightly shifted. In our model, this shift can be very well explained by a macroscopic mode III while the major bump is due to the existence of a small amount of mode II. As we already know the toughness contrast, C and the angle β for this triangle, we use a two parameter optimization fit based on Eq. (3.23) to extract the value of ϕ_0 and ρ_0. For the triangle in Fig. 5.6, we find a mode mixity $\phi_0 \sim -0.165 \pm 0.02$ while $\rho_0 \sim -0.016 \pm 0.0025$.

[1] Actually as it will be showed later, the region of higher toughness is created by the crack itself through the process of front fragmentation

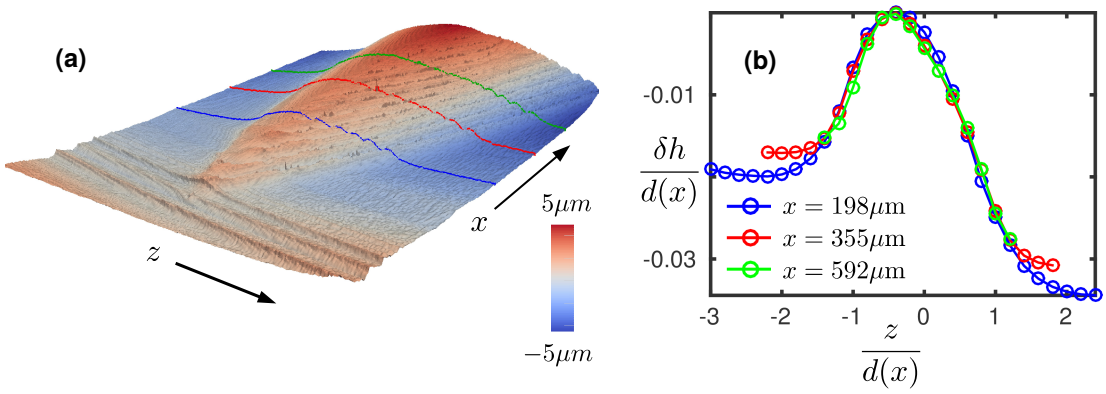

Fig. 5.5 *Normalized height profiles of the crack front: (a) Height profiles at three locations chosen for normalization and (b) shows their normalization. The height profile is smoothened to ignore the facets on the triangle. x in (b) refers to the distance from the tip of the triangle and the image in (a) is scaled by 15 times for better visualization*

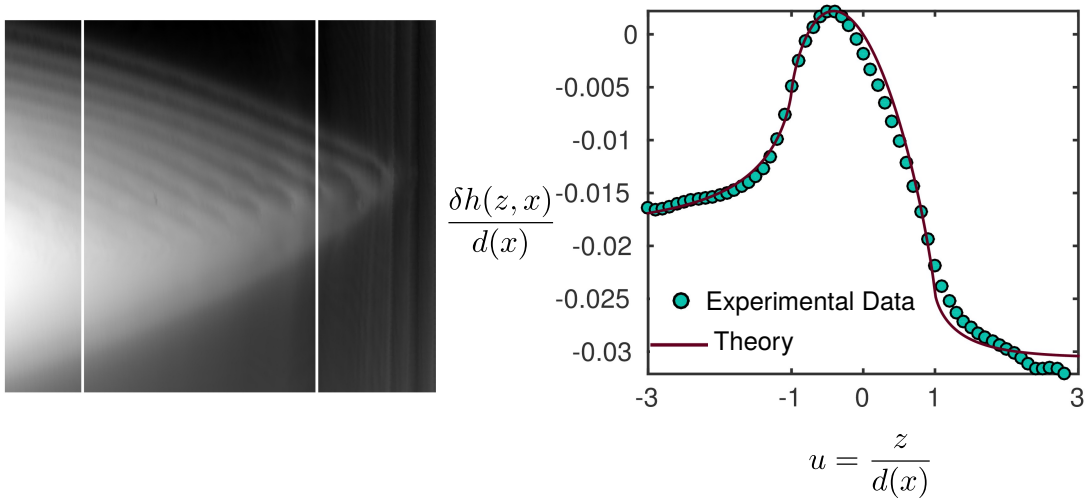

Fig. 5.6 *(a) Gray scale map of the triangle analyzed. An average normalized front is obtained by considering all the front shapes between two white lines. (b) Markers in green show the average experimental front shape after normalization and its comparison with theory. The parameters obtained from the fit are* $\phi_0 = -0.165 \pm 0.02$, $\rho_0 = -0.016^o \pm 0.0025$ *while* $C = 0.225$, $\epsilon = 0.05$ *from the in-plane front geometry in section 5.2*

Method 2 : Inclination of the triangle in different directions

Another way of analyzing the triangular pattern is to exploit an interesting feature of the theoretical out-of-plane profiles: the height $h(z,x)$ once normalized by the triangle width $d(x)$ is a function of $u = \frac{z}{\tan(\beta x)}$. This means that we can write the theoretical out-of-plane shape as $h(z,x) = d(x)[\phi_0 C\Psi(u) + \rho_0 C\Phi(u)]$ where $d(x) = \tan\beta x$. As shown in the following, this means that the slope of the triangular bump in some direction α with respect to the propagation direction is constant. Let us refer to the schematic shown in Fig. 5.7(a). If we pick any direction $\alpha = \text{atan}(\frac{z}{x})$ with respect to the propagation direction x, the value of $h(z,x)$ along that direction varies linearly. This comes from the property that the out-of-plane deviation is proportional to $d(x) = \text{x}\tan\beta$ and so $l = x/\cos\alpha$. The corresponding slope $\tan^{-1}(h/l)$ depends only on the parameter u that is constant if α is fixed. This can then be used to compare theory and experiments and measure the mode-mixity factors, ϕ_0 and ρ_0. The derivation of this slope and its variation with α is as follows:

Along a line making an angle α w.r.t propagation direction, x, $z = x\ \tan\alpha$. The value of $h(z,x)$ along this line is thus given by $h(z = x\ \tan\alpha, x)$ which corresponds to

$$h(z = x\ \tan(\alpha), x) = \text{x}\ \tan\beta \left[\phi_0 C\ \Psi\left(u = \frac{\tan\alpha}{\tan\beta}\right) + \rho_0 C\ \Phi\left(u = \frac{\tan\alpha}{\tan\beta}\right)\right]$$

The slope of the bump along that direction is then given as

$$m^{th}_{\rho_0,\phi_0} = \frac{h(z,x)}{l} = \frac{h(z,x)}{\frac{x}{\cos\alpha}} = \left[\phi_0 C\ \Psi\left(u = \frac{\tan\alpha}{\tan\beta}\right) + \rho_0 C\ \Phi\left(u = \frac{\tan\alpha}{\tan\beta}\right)\right] \tan\beta\cos\alpha \tag{5.1}$$

In the following, one can extract the experimental value of slope as a function of α and compare with the theory, $m_{th}\alpha$. A procedure that finds the values of ϕ_0 and ρ_0 that optimizes the fit of the experimental curve by the theoretical prediction is subsequently used. Once again one observes that the slope is maximum slightly away from the centre $z = 0$, the shift being caused by a small macroscopic mode III. The best fit of the experimental data is shown in Figure 5.7(c). It confirms with the value determined with method 1 and we obtain $\phi_0 \sim -0.15 \pm 0.02$ and mode III mixity, $\rho_0 \sim -0.016 \pm 0.0025$. The triangular fracture patterns let by the crack after failure may serve as a local load cell that measures the applied loading conditions in terms of $\frac{K^0_{II}}{K^0_I}$ and $\frac{K^0_{III}}{K^0_I}$ We will later discuss in detail the measured values of these shear stress intensity factors.

We would like however make a first comment on ϕ_0 that is found to be one order of magnitude larger than ρ_0. An independent measurement of the mode II mixity ratio based on the observation of a macroscopic kink angle $\alpha = 4.6^o$ on the fracture surface before the roughening transition region leads to a mode mixity $\phi_0^{\text{kink}} \simeq -0.023$, in apparent contradiction with the value $\phi_0^{\text{tri}} \simeq 0.15$ extracted from the shape of the triangular patterns.

5.4 Toughening mechanism inside the triangle

In the previous section, we used a model where a crack under mode I +II + III is pinned in-plane by a triangular obstacle. This allowed us to capture very well the out-of-plane

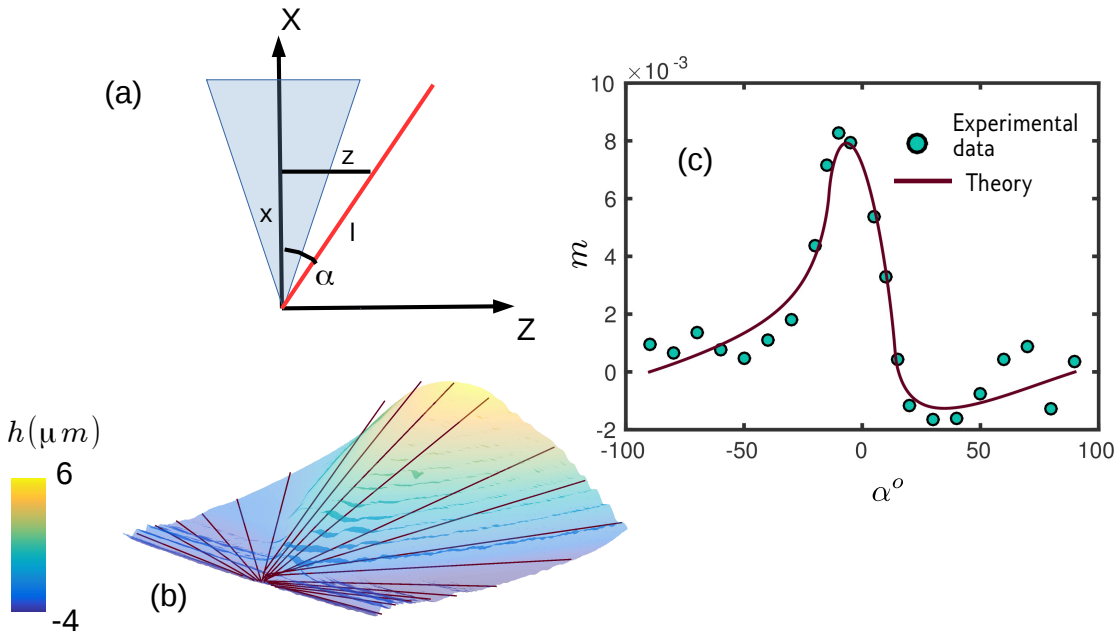

Fig. 5.7 *illustrates the methodology employed to extract the slope of the bump along different angles α from the proagation direction x(a) shows the schematic for the angle definition (b) shows the extraction of the experimental slope $m(\alpha)$, the lines of brown color showing the slopes extracted from the triangular pattern. (c) compares the best fit based on equation (5.1) and experiment. For this triangle, the same as in Figure 5.6, the parameters obtained are $\phi_0 = -0.15$ and $\rho_0 = 0.016$ while $C = 0.25$, $\epsilon = 0.0$ and $\beta = 20^o$ are determined from the in-plane geometry of the front.*

shape of the triangular pattern. However, we still have not addressed a couple of important questions : What induces toughening in the triangle? and what triggers the instability from smooth to a faceted profile? We address them in the sections that follow.

Figure. 5.4 (c), shows step like features on the triangle that resemble the factory-roof profile of fragmented cracks observed subjected to mode I+III observed in various materials (see [Cooke and Pollard, 1996, Hull, 1994, Knauss, 1970, Lazarus et al., 2008, Sommer, 1969]). A typical factory roof schematic of a tensile crack (mode I) subjected to shear parallel to the crack front (mode III) is shown in Figure. 5.8(c). The crack front twists to form two facets which are referred to as type A and type B, the former gradually twisting such that it faces a small anti-plane shear, while the type B twists in the opposite direction to join two successive facets of type A [Hourlier and Pineau, 1979].

In Chapter 4, we studied the effect of an anti-plane shear dependent fracture energy on front fragmentation. In particular, we showed that it could significantly decrease the fragmentation threshold $\frac{K_{III}}{K_I}|_c$ and so potentially account for the experimentally measured values that are generally found very small. If we come back to a faceted crack, type A facets face a very small mode III while type B facets are oriented in the opposite direction and hence face much higher anti-plane shear. Assuming that fracture energy is a quadratic function of the mode III mixity, the fracture energy of type B facets are much

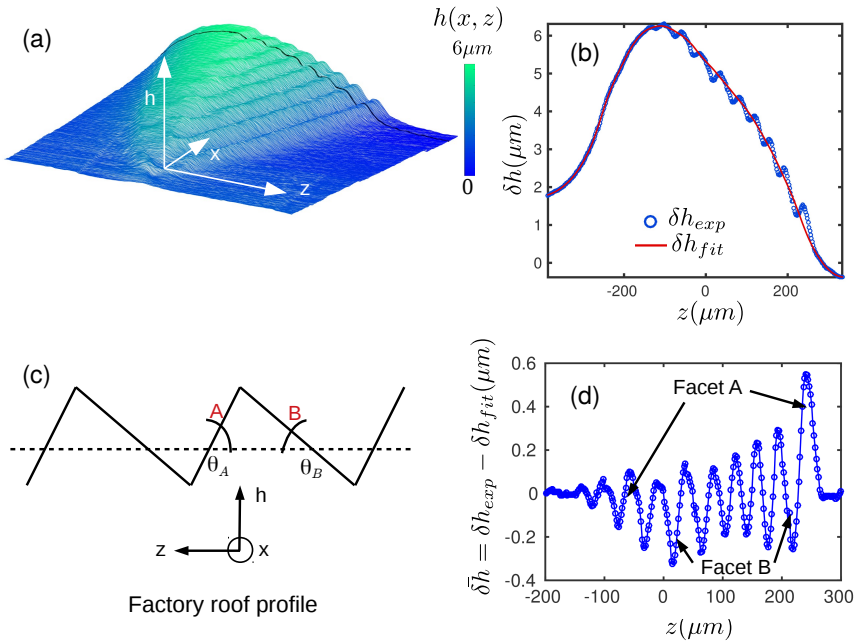

Fig. 5.8 *(a) 3D shape of the triangular pattern with clearly visible facets; (b) height profile along the mean crack front direction z at a distance $x = 600$ μm from the triangle tip (black line in Fig (a)). The dots are the experimental points while the red line is a smooth fit of the experimental shape. (c) schematic of the factory roof profile resulting from front fragmentation while (d) is the experimental faceted profile seen on the triangle after subtraction of the average shape, δh_{fit} from the triangle. This triangle corresponds to the same one analyzed in Fig. 5.7*

higher than the one of type A and much higher than the fracture energy corresponding to the macroscopic anti-plane shear of $\rho_0 = \frac{K^0_{III}}{K^0_I}$. But in the end, is the fracture energy higher for a flat or for a fragmented front?

To address this question consider the example presented in Fig. 5.9. For a planar crack under macroscopic shear ρ_0, $G_c^{planar} = G_c^I(1+\gamma\rho_0^2)$ and the toughening compared to pure mode I is $\Delta G_c^{planar} = \gamma\rho_0^2$. For a fragmented crack, let us assume a simple geometry where the lengths of facets of type A and type B are equal i.e $r = 1/2$ and $\theta_A = \theta_B$ where r is the proportion of facets A and θ_A and θ_B are the angle of the facets of type A and B respectively. We assume that facets A twist such that they face zero anti-plane shear ($\rho_A = 0$) and facets B rotate in the opposite direction thus facing twice the macroscopic shear($\rho_B = 2\rho_0$)[2]. Under these conditions, $G_c^A = G_c^I(1+\gamma\rho_A^2) = G_c^I$ and $G_c^B = G_c^I(1+\gamma\rho_B^2) = G_c^I(1+4\gamma\rho_0^2)$. As the fragmented fronts is periodic with facets A and B, the effective fracture energy inside the triangle is $G_c^{frag} = rG_c^A + (1-r)G_c^B = G_c^I(1+2\gamma\rho_0^2)$ and the toughening compared to pure mode I is $\Delta G_c^{frag} = 2\gamma\rho_0^2$, thus

[2]It will be shown later that the angle of the facet is directly proportional to the local shear it faces. Thus larger the anti-plane shear on the facet, larger is the facet angle.

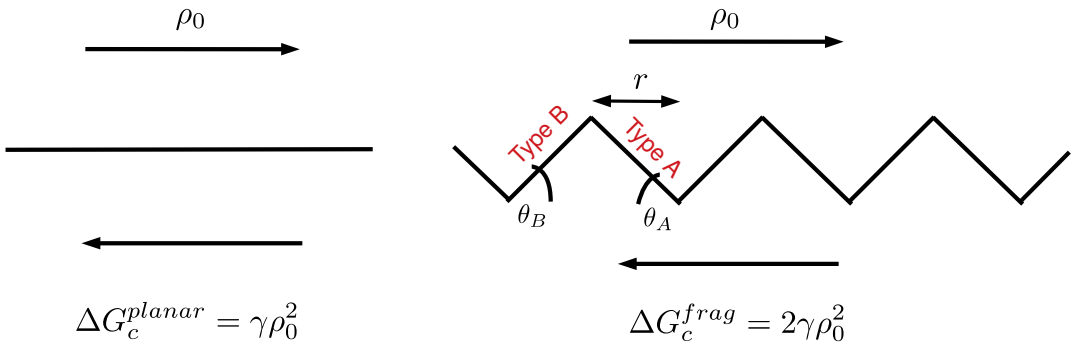

Fig. 5.9 *Effective fracture energy for a (a) Planar crack and (b) fragmented crack.*

showing that a fragmented front is tougher than a planar front.

This toughening mechanism inside the triangular region may be responsible for the pinning of the crack observed in Fig. 5.1 and 5.2. To describe quantitatively this mechanism, one must know how G_c increases with ρ. As a result, one first assumes the shape of the function $G_c(\rho) = G_c^I(1+\gamma\rho^2)$ and then determine the value of γ from the comparison with experiments. We finally propose an independent method to measure the value of γ using the facet geometry.

5.5 A possible explanation for the angle of the triangle

One puzzling feature of the triangular fracture patterns is that the facets translate along the crack front direction z as the crack himself moves forward letting lines with some inclination β with respect to the propagation direction x. This is not without reminding other observations made in other materials (see Baumberger et al. [2008], Gent and Pulford [1984], Kermode et al. [2008], Kolvin et al. [2017] etc.). In Chapter 4, we looked at the stability of a perturbed crack under mode I + II + III with a mode-III dependent fracture energy $G_c(\rho)$. It was found that unstable modes emerge in the form of an elliptic helix. Also, it was found that this elliptic helix drifts along z with an angle $dz/dx = -\tan^{-1}\xi_2$ (see Section 4.6.1). For these facets to translate we also found out mode II must be non-zero and that the fracture energy must depend on mode III. The observation of translating facets on PMMA is a strong indication that the mode II is non-zero and that the fracture energy is a function of the mode III mixity. We remind that according to the scenario proposed in Chapter 4, front fragmentation proceeds in two steps. First, an helicoidal mode of crack growth emerges if ρ_0 is larger than ρ_c. And subsequently, this mode evolves into a faceted front that displays facets of type A and B. With that scenario in mind, We look at these facets as the post bifurcated mode of the fragmentation instability problem in mode I + II + III and compare the measured angle β with ξ_2 which may provide another way to measure ϕ_0. Refering to Eq. (4.17), we predict

$$\xi_2 = -\tan\beta = \frac{-N_1D_2 + N_2D_1}{D_1^2 + D_2^2} \tag{5.2}$$

where N_1, D_1, N_2 and D_2 depend on the material parameters, γ, κ and ν and the loading parameters ϕ_0 and ρ_0. To compare with our experiments, we take $\beta = 18.5^o$, $\kappa = 2$, $\nu = 0.37$ (for PMMA) and $\rho_0 = 0.015$. This leaves us with two unknowns ϕ_0 and γ and a relation between them is given by Eq. (5.2). Note that if we already know γ, this allows us to get another independent measurement of the mode II mixity ϕ_0 that can be compared with the value previously determined in section 5.3.

5.6 Measurement of the parameter γ in shear-dependent fracture toughness

In this section, we present a methodology to extract the value of the pre-factor γ defined in Eq. (4.1) where γ provides a measurement of the dependence of G_c with the amount of shear. Section 4.6.2 presented a formula that provides the mode III mixity, $\delta\rho$ along the crack for stationary conditions i.e. for perturbations independent of x. For a fragmented crack as shown in Fig. 5.8 (c), the shape is independent of x and so this formula can be safely applied. It is reminded here :

$$\delta\rho = -\frac{\rho_0\phi_0(2-3\nu)(4-3\nu)}{(2-3\nu)^2\phi_0^2+16\rho_0^2}\frac{1}{\pi}PV\int_{-\infty}^{\infty}\frac{\delta h(z')-\delta h(z)}{(z'-z)^2}dz+ \\ \frac{2(2-3\nu)^2(1-\nu)\phi_0^2+4(4-5\nu)\rho_0^2}{(2-3\nu)^2\phi_0^2+16\rho_0^2}\frac{\partial\delta h}{\partial z}$$

where ρ_0 and ϕ_0 are the mode-mixity ratios. One notices two terms: the first one is a semi-local term defined as an integral along the out-of-plane profile of the crack. The second term is a local term proportional to the slope of the crack $\frac{\partial\delta h}{\partial z}$. To compare the contributions, we look at the prefactors of each of them for the values of ρ_0 and ϕ_0 determined previously. One finds that the prefactor of the first term is 10 times smaller than the prefactor of the second one. Thus we ignore the contribution of the semi-local term leading to:

$$\delta\rho = \frac{2(2-3\nu)^2(1-\nu)\phi_0^2+4(4-5\nu)\rho_0^2}{(2-3\nu)^2\phi_0^2+16\rho_0^2}\frac{\partial\delta h}{\partial z} = g(\rho_0,\phi_0)\frac{\partial\delta h}{\partial z} \tag{5.3}$$

where the pre-factor is noted as $g(\rho_0, \phi_0)$. This equation is powerful as we now have a direct measurement of the mode III mixity on each facet from their slope. In particular it shows that the larger the slope, the larger the amount of mode III on the facet.

Figure 5.10 shows a schematic representation of the faceted crack profile on the triangle. Let R be the region inside the triangle without any facets (with respect to the total width of the triangle) and r be the proportion of facet A, i.e. the length of the facet A to the wavelength of the elementary fragments made of facet A and B . Let us also note θ_A and θ_B, the angle of facets A and B respectively. To evaluate γ we use the observation that toughening takes place inside the triangle. The contrast is defined as

$$C = \frac{G_c^{in}-G_c^{out}}{G_c^{out}} \tag{5.4}$$

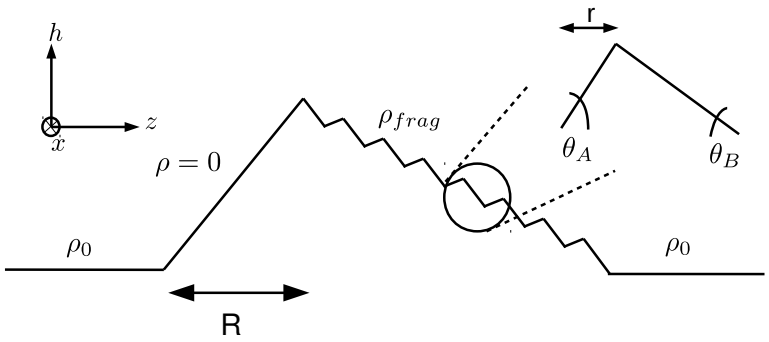

Fig. 5.10 *Schematic of a fragmented crack on a triangle*

Outside the triangle, the fracture energy is straightforward as this part of the front is under macroscopic shear ρ_0 , so that

$$G_c^{out} = G_c^I(1 + \gamma\rho_0^2) \tag{5.5}$$

Inside the triangle, the macroscopic loading is not uniform due to the shape of the triangle. For simplifying the following calculation, we assume that the flat portion of the triangle rotates such that it faces zero shear (Note that this assumption does not affect much the value of γ and ϕ_0 estimated at the end of this section). On the contrary, the characteristic shear in the fragmented region will be higher than ρ_0 as it rotates in the opposite sense. Let us call, ρ_{frag}, as the average shear in the fragmented part. The fragmented region is made of facets of type A and B and we can calculate the amount of mode III on each facet using Eq. (5.3).
If applied on facet A, the total shear on facet A is

$$\rho^A = \rho_{\text{frag}} + \delta\rho = \rho_{frag} + g(\rho_0, \phi_0)\frac{\partial \delta h}{\partial z}|_A = \rho_{frag} - g(\rho_0, \phi_0)(\theta_A)$$

and if applied on facet B, it gives

$$\rho^B = \rho_{frag} + g(\rho_0, \phi_0)\theta_B \tag{5.6}$$

Notice here the facet angles are of opposite signs as they rotate the opposite ways. However, the angle θ_A and θ_B are both defined positive.

We now assume that facet A rotates such that it faces zero shear , $\rho^A = 0$ [3]. This provides an estimate of ρ_{frag} as

$$\rho_{\text{frag}} = g(\rho_0, \phi_0)\theta_A$$

Substituting in Eq. (5.6), we obtain

$$\rho^B = g(\rho_0, \phi_0)[\theta_A + \theta_B]$$

[3]This assumption was first made by Cooke and Pollard [1996] so that facet A remain under purely tensile conditions.

The fracture energy on facet A and facet B, assuming $\kappa = 2$, are

$$\begin{cases} G_c^A = G_c^I(1+\gamma {\rho^A}^2) = G_c^I \\ G_c^B = G_c^I(1+\gamma {\rho^B}^2) = G_c^I[1+\gamma g(\rho_0,\phi_0)^2(\theta_A+\theta_B)^2] \end{cases}$$

As the fragmented region is made up of facets A (in proportion r) and B (in proportion $1-r$) the effective fracture energy of the fragmented part of the triangle is :

$$G_c^{\text{eff frag}} = rG_c^A + (1-r)G_c^B = rG_c^I + (1-r)G_c^I[1+\gamma g(\rho_0,\phi_0)^2(\theta_A+\theta_B)^2]$$

The effective fracture energy inside the triangle is now due to both the flat (of proportion R) and the fragmented part (of proportion $1-R$) which writes as

$$\begin{aligned} G_c^{\text{in}} &= RG_c^{\text{flat}} + (1-R)G_c^{\text{eff frag}} = RG_c^I + (1-R)G_c^{\text{eff frag}} \\ \Longrightarrow G_c^{in} &= RG_c^I + (1-R)rG_c^I + (1-r)G_c^I[1+\gamma g(\rho_0,\phi_0)^2(\theta_A+\theta_B)^2] \end{aligned} \tag{5.7}$$

Thus, substituting Eq. (5.7), (5.5) in the expression of the contrast, (5.4), we obtain γ as a function of the facet geometry and the loading conditions as

$$\gamma = \frac{C}{g^2(\rho_0,\phi_0)(\theta_A+\theta_B)^2[(1-R)(1-r)-(1+C)\rho_0^2]} \tag{5.8}$$

To summarize, if we know the facet geometry [r, R, θ_A,θ_B] , the toughness contrast C and the applied macroscopic loading ρ_0 and ϕ_0, we can measure the value of γ. In the following, we assume that both γ and ϕ_0 (the value which was found to be surprisingly large in section 5.3) are assumed to be unknown. Eq. (5.2) that relates the angle β of the triangle to these parameters provides another way to measure γ so we use the system of equations (5.2) and (5.8) to get γ and ϕ_0. For the triangle analyzed, the geometry of the facet parameters are $r = 0.288$, $R = 0.218$, $\theta_A = 1.7^o$, $\theta_B = 0.9^o$ together with $\nu = 0.37$, $C = 0.225$, $\rho_0 = -0.016$ and $\beta = 18.5^o$ we obtain thus :

$$\boxed{\gamma = 850 \quad \text{and} \quad \phi_0 = 0.029}$$

The experimentally measured value of γ is found to be very large! As $G_c(\rho) = G_c^I(1+\gamma\rho^2)$, even a small amount of anti-plane shear will increase the fracture energy to a large extent. In our case, the macroscopic shear is of the order of 2% which is enough to increase the fracture energy inside the triangle by 20 % !

Comment on the value of ϕ_0

The value of ϕ_0 obtained from the previous method is rather small $\phi_0 \simeq 3\%$. This is rather expected as misalignment in the applied loading during the test or imperfections in geometry (see Fig. 2.4) may result in some mode II of the order of a few percent. In addition, we do observe a small kink in the fracture surface right before the formation of triangles. This kink angle corresponds to a mode II mixity, $\phi_0^{\text{kink}} \sim 0.025$. Then why is the mode II,$\phi_0^{\text{tri}} \sim 0.15$ extracted from the shape of the triangle so high?. The response to this question is not clear and it would deserve further investigations: A possible qualitative

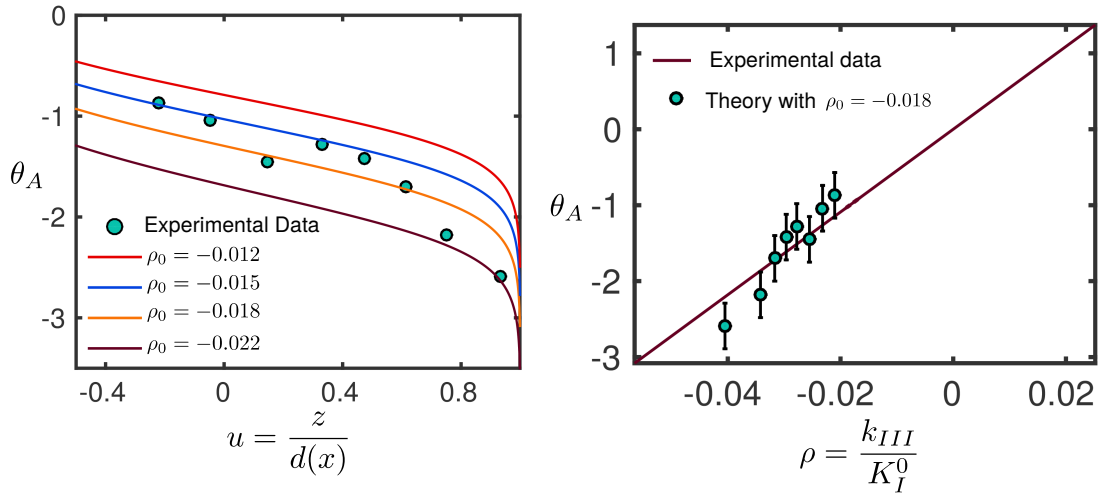

Fig. 5.11 *Comparison of facet angles measured experimentally vs theory (a) θ_A vs u for different values of ρ_0 and (b) θ_A vs ρ for $\rho_0 = -0.018$*

explanation would be that the triangular bump itself is a facet and as such its amplitude would grow rapidly, much faster than the growth rate induced by the presence of a small macroscopic mode II, $\phi_0 \sim 2\%$[4]. So quantitatively from now on, we consider $\phi_0 \sim 0.029$ as a good estimate of ϕ_0. In the previous analysis, we have used the value of $\rho_0 = -0.016$ which was obtained from the shape of the triangle. We will justify this choice of ρ_0 in the next section where we analyse the angle of the facets of type A within the triangular region.

5.7 Variation of angle of type A facets

We now have a rather good understanding of the toughening mechanism within the triangle that relates to the fragmentation of the front. This allows us to explore more subtle effects like the variation of the angle of the facets within the triangle. If we look closely at Fig. 5.8(b) and (d), we find that the angle of the facet A is higher at the border of the triangle and lower at the top. As the facet angle is directly proportional to the amount of mode III shear the facet angle can be predicted from the calculation of the local applied shear inside the triangle. This local k_{III} is due to the in-plane and out-of-plane perturbations of the front and can be calculated using the formulae relating the stress-intensity factor to the front geometry (Eqs. (3.13) and (3.14)) leading to

$$k_{III} = K^0_{III} + K^0_I \frac{2(1-\nu)^2}{2-\nu} \frac{\partial \delta h}{\partial z} + K^0_{II} \frac{2(1-\nu)}{2-\nu} \frac{\partial \delta f}{\delta z}$$

Dividing by K^0_I we obtain,

[4]Among the puzzling similarities of the triangular bump with the elementary features resulting from front fragmentation, one may notice the presence of the two sides of the bump, one under dominantly mode I (akin to facet A) and another one under anti-plane shear (akin to facet B), see Fig. 5.8(a)

$$\rho(z) = \rho_0 + \frac{2(1-\nu)^2}{2-\nu}\frac{\partial \delta h}{\partial z} + \phi_0 \frac{2(1-\nu)}{2-\nu}\frac{\partial \delta f}{\delta z} \tag{5.9}$$

To predict the distribution of shear in the triangle, we need the in-plane and out-of-plane shape of the front. These can be obtained experimentally (see Fig. 5.2 for in-plane and Fig 5.8 for out-of-plane deformation). However, for practical purposes, we use the theoretically predicted shape with the parameters $\phi_0 = -0.15$, $\rho_0 = -0.016$ and $C = 0.225$ that provides a very good fit to the out-of-plane experimental shape. The prefactor to the in-plane term is the macroscopic mode II, ϕ_0 for which we take $\phi_0 = -0.029$.

To predict the facet angle we make the assumption that facet A undergoes zero anti-plane shear. This allows us to write

$$\rho^A = 0 = \rho(z) - g(\rho_0, \phi_0)\theta_A \Longrightarrow \theta_A = \frac{\rho(z)}{g(\rho_0, \phi_0)}$$

where the expression $g(\rho_0, \theta_0)$ is provided in Eq.(5.3). To extract the facet angle from our experiments, one must measure them w.r.t the reference position of the front. To proceed, we fit the experimental shape by a smooth curve and then subtract it from the experimental surface to obtain the factory roof profile shown in Fig. 5.8(d). The angles of facet A is then measured as a function of z.

The comparison between the experimentally measured facet angles and the model prediction is shown in Fig. 5.11(a) for different values of ρ_0. For $\rho_0 = -0.018$, the model prediction compares well with the experiments. This values is chosen again to compare the predicted value of θ_A as a function of $\rho(z)$ with experiments (see Fig. 5.11 (b)). This value of ρ_0 is very close to the one determined from the out-of-plane shape of the triangular patterns in section 5.3, confirming the previous estimate.

5.7.1 Another measurement of parameter γ through local shear

In section 5.6, γ is measured using the fragmented geometry of the front within the triangle assuming that the mode III mixity on the non-fragmented part of the triangle (of proportion R, see Fig. 5.10) and on type A facets in the fragmented region is zero. Here we follow another methodology that do not take into account the fragmented geometry of the crack front within the triangle. In the previous section, we showed how the field of local shear $\rho(z)$ can be computed from the experimental front geometry. Thus the effective fracture energy inside the triangle is

$$G_c^{in^{\text{eff}}} = \frac{\int_{-d}^{d} G_c(\rho(z))dz}{2d}$$

The toughness contrast then writes as

$$C = \frac{G_c^{in^{\text{eff}}} - G_c^{\text{out}}}{G_c^{\text{out}}} = \frac{1}{2d}\frac{\int_{-d}^{d} G_c^I(1+\gamma\rho(z)^2)dz}{G_c^I(1+\gamma\rho_0^2)} - 1$$

From the loading parameters $\rho_0 \sim -0.018$ and $\phi_0 \sim -0.029$ and the toughness contrast $C = 0.225$, the above equation can be used to evaluate γ. This calculation is done numerically and gives $\gamma = 800$ which compares with the previous estimate of $\gamma = 850$. In the previous methodology, the type B facets face larger mode III shear in comparison

to the macroscopic one was the main reason for toughening in the triangle while in this calculation, toughening results from the increase in local shear due to the shape of the triangle. Both approaches are slightly different but however lead to comparable values of γ. At lower velocity, in the rough region of the fracture surface we do observe triangular patterns with similar out-of-plane shapes but with facets on the border of the triangle only. This suggests that the shear induced by the front deformation (without facets) may be enough to toughen some region of the front and lead to triangular patterns. However, front fragmentation seems necessary to trigger the front formation of the triangle and initiate the toughening process. A scenario describing the different phase of the triangular pattern formation is proposed in Chapter 6.

5.8 From smooth to a faceted fracture surface

Upto now we have proposed explanations for the shape of the triangular patterns as well as the toughening mechanism taking place inside the triangle. These relied on the assumption that the front did fragment prior the emergence of the triangles. In this section, I address the issue of the transition from a planar to a fragmented front. In particular, how to explain that such a low value of macroscopic mode III can lead to front fragmentation? We have learnt from the shape of the triangular patterns that the crack is not only subjected to mode I but also to small amounts of mode II and mode III. We now come back to Chapter 4 where we have theoretically studied the stability of a straight crack under mode I, II and III when the fracture energy depends on the amount of shear. It was shown that the critical mode III mixity ratio ρ_c for front fragmentation could be actually very low. More quantitatively, ρ_c depends on the material parameters, γ, κ and ν and loading parameter, ϕ_0. The critical ratio for fragmentation is a solution to the equation

$$[2-3\nu-A(4-5\nu)](2-\nu-A\nu)+4A^2(1-\nu)^2(2-3\nu)\frac{\phi_0^2}{\rho_c^2}=0 \text{ where } A=\frac{\kappa\gamma\rho_c^\kappa}{1+\gamma\rho_{cr}^\kappa}$$

Through our analysis of the shape of the triangular pattern, we were able to extract the value of γ and ϕ_0. Taking $\kappa = 2$, $\nu = 0.37$, we can then predict the critical ratio for fragmentation. We find $\rho_c \simeq 0.0261$ that is very close to the macroscopic shear $\rho_0 \sim 0.02$ applied to the specimen and determined from the triangular pattern geometry. In Chapter 4, it was shown that if a mode-III dependent fracture energy is considered, then the critical ratio for instability is not of the order of 0.4 but significantly lower down to a few percents when γ is large, as for PMMA. This prediction is in full line with our experimental findings. In the following chapter, I present the general conclusions of this work and propose some perspectives.

Chapter 6

Conclusion and Perspectives

This work is dedicated to the roughening transition observed in PMMA as the crack decelerates. To study the transition, we designed a new fracture test geometry that allowed us to explore crack propagation from a high velocity (typically $\sim 100\text{ms}^{-1}$) down to lower speeds ($\sim 0.1\text{mms}^{-1}$). At a critical velocity close to $v_c = 15$ mms^{-1}, the crack changes its behavior: from smooth the front fragments by forming facets of the order of 50 μm on the fracture surface. These fragments drift along z at an angle β from the propagation direction x leaving triangular patterns on the fracture surface. Deciphering these patterns improved our understanding on how material fails under mixed mode loading conditions. We list in the coming sections the important results of this work and provide prospectives for future work.

6.1 Conclusions

- The shape of the triangular patterns provided a way to measure the macroscopic loading conditions applied to the specimen. This was achieved by two different methods : the first one by the out-of-plane shape of the triangle while the second one interprets the angle at which the facets drift. This resulted in two different measurements of the amount of mode II, ϕ_0: The first method predicts $\phi_0^{tri} \sim -0.15$ while the second method gave $\phi_0^{\text{drift}} \sim -0.029$ in better agreement with a slight misalignment of the applied mode I loading during the experiments. The amount of mode III, ρ_0 are rather consistent and give $\rho_0 \sim -0.02$.

- These patterns allowed us to characterize the dependency of the fracture energy to anti-plane shear. Assuming fracture energy of the form $G_c(\rho) = G_c^I(1 + \gamma\rho^2)$, we were able to measure the value of γ and is found to be really large, $\gamma = 850$ for our experiments.

- As shown in Chapter 4, large value of γ results in a low value of the critical mode III mixity ratio ρ_c for fragmentation. Our linear stability analysis predicts a value $\rho_c \sim 0.026$ which is comparable to the level of mode III shear $\rho_0 \sim 0.02$ inferred from the fracture pattern. This low value is in line with other experiments where the fragmentation threshold is also very small [Pham and Ravi-Chandar, 2014, Sommer, 1969].

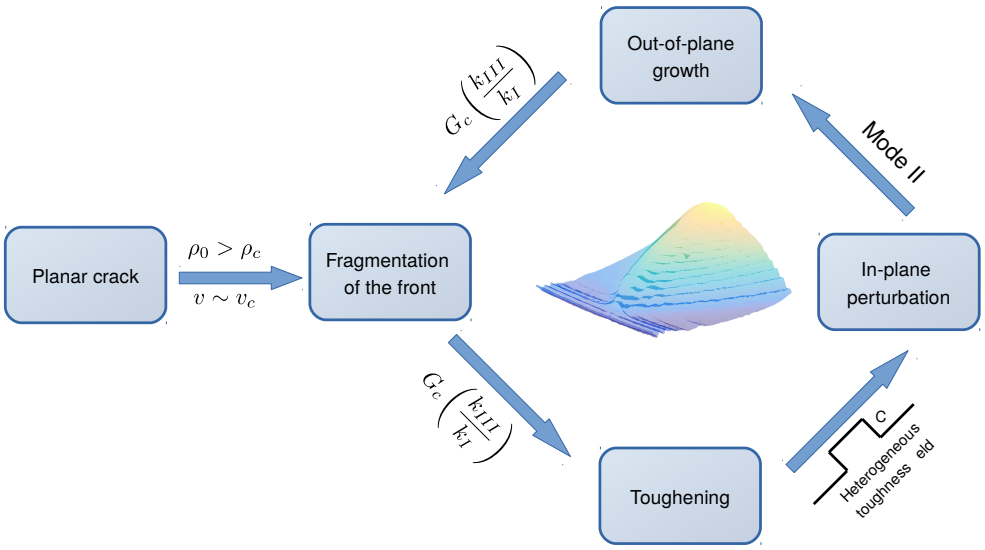

Fig. 6.1 *Self-sustained mechanism proposed to explain the formation of triangular patterns: Beyond a critical threshold, the planar crack front fragments to form the first facets. These facets toughen the material leading to in-plane deformation of the crack. Under a small amount of mode II, the crack deviates out-of-plane non-uniformly. The out-of-plane crack perturbations, induces a further local shear k_{III} causing more fragmentation and more toughening, forming ultimately large triangular fracture patterns in a self-sustained way.*

- Our experiments were performed on dominantly tensile on a nominally homogeneous material. However large scale fracture patterns emerge in a self-sustained manner that we describe in Fig. 6.1. When the fragmentation threshold decreases down to the level of the macroscopic shear, the crack fragments forming precursory facets. As shown in section 5.4, front fragmentation induces toughening hence causing in-plane deformation of the front that takes a characteristic U shape clearly visible on the fracture surface. Under a small amount of mode II, this perturbed crack kinks non-uniformly along z leading to an out-of-plane growth of a triangular bump. The formation of this bump induces a higher local shear (see Eq.(5.9)) leading to front fragmentation. The same feedback loop takes place again, as more fragmentation results in more in-plane deformation and ultimately more out-of-plane deviations of the front.

- Under the influence of a small amount of Mode II and a mode-dependent fracture energy, our stability analysis predicts that the facets will drift along the crack front during propagation. This phenomenon is observed in our experiments and the amount of mode II inferred from the drift angle provides $\phi_0 \simeq 0.03$, a reasonable value for our experiments. This mechanism may explain the observation of drifting facets observed in other materials like gels [Baumberger et al., 2008, Kolvin et al., 2017, Tanaka et al., 1998] and rubber [Gent and Pulford, 1984].

6.2 Perspectives

In this section we propose some possible future directions of research that could address the question raised by our findings.

- Crack in PMMA remains smooth at high velocities and fragments only below a certain speed $v_c = 15\text{mms}^{-1}$. Such an observation is also made in the experiments on gels [Baumberger et al., 2008] where cross hatch instabilities are seen below some critical crack speed. We recall that fragmentation threshold is inversely proportional to γ, the parameter which controls how the fracture energy depends on mode III mixity. We make the assumption that γ (that is a material property) increases as the velocity decreases. As a result, the fragmentation threshold decreases when the crack decelerates. This hypothesis is supported by the fact that for cracks that propagate at slow velocities (in the stick regime), we do observe systematically the fracture surface is always fragmented, implying a high value of γ at low velocities.

- The wavelength of the facets does not vary much in our experiments and is typically $\lambda \simeq 40\mu m$. Such a length scale is also observed in other crack front fragmentation problems under mode I + III (see [Chen et al., 2015, Lin et al., 2010, Pham and Ravi-Chandar, 2014]. The framework of LEFM is scale-free, so that our stability analysis does not predict any characteristic deformation of the fragmented patterns. This raises the question of the origin of this length scale. In the work of [Baumberger et al., 2008], the height of the facet is found to correlate with the non-linear length scale, l_{NL}, which is the length below which non-linear elastic dissipative processes occur [Bouchbinder et al., 2010]. The non-linear length scale is calculated using : $l_{NL} \sim \frac{G_c}{E}$, where G_c is the fracture energy and E is the Young's modulus of the material. This gives us the non-linear length scale in PMMA as $l_{NL} \simeq 1\mu m$, which is also the height of the facets in our experiments. Finally, the wavelength could then be understood as a combined effect of the non-linear length scale and mode III shear (which sets the angle of the facets). A detailed investigation of the effect of non-linear elasticity on fragmentation would then be necessary to understand the facet size.

- Along the width of the sample, we find typically 8 to 10 triangles, which sets a distance of 1 mm between these triangles. Let us imagine that the crack is under a macroscopic shear close to the critical threshold for fragmentation. Defects in the material are always ubiquitous, so if a fragmented fracture mode may emerge, it will then preferentially initiate at the location of these defects. Thus the distance between the triangles (in our case $\sim$ 1mm) is reminiscent of microstructural defects in PMMA. Triangular fracture patterns similar to the ones studied here are also observed at low crack speeds in silicon crystals [Kermode et al., 2008]. In their experiments, they find that the spacing between these triangles is directly related to the defect density and with increasing defect density controlled through the doping with Boron atoms [Kermode et al., 2013]), they found that the distance between triangles decreased. We expect a similar mechanism controlling the distance between the triangles in PMMA too. One must also investigate if these defects relate to ones responsible for the nucleation of crack at high crack speeds [Guerra et al., 2012]? or

on the contrary, if they correspond to regions within the PMMA structure that are particularly tough?

- We have presented two ways of extracting the applied macroscopic mode II : from the shape of the triangle, $\phi_0^{\text{tri}} \sim 0.15$ and from the translation of the facets, $\phi_0^{\text{drift}} \sim 0.029$. A misalignment in the loading or with the sample preparation may result in a mode II of the order of a few percents, so that the value of ϕ_0^{tri} seems too large. Then what is the origin of such a large bump inside the triangle? In the fracture of silicon crystals, [Kermode et al., 2008], cracks show an instability at low velocities and deviate out-of-plane leaving triangular fracture patterns on the fracture surface. Using molecular dynamics, they show that at low velocities, the atoms just ahead of the crack tip favour rearrangement triggering an out-of-plane deviation of the crack leading to these patterns. From a continuum mechanics perspective, this can be thought of the existence of a preferential direction for crack propagation where G_c is lower. This can be seen as an anisotropy in the fracture energy with a preferential direction θ, where this angle θ is measured from the propagation plane (x-z). This results in a propagation for a finite value of k_{II} as $k_{II} = 0$ would correspond to a path straight ahead. If we now assume a mode-II dependence of fracture energy, $G_c = G_c^I(1 - \alpha|\frac{k_{II}}{K_I^0}|)$, then G_c decreases away from the main propagation plane and could explain the large amplitude of the bump seen on the triangles. This idea will be explored in the future to understand the amplitude of the out-of-plane excursion of the crack within the triangle.

- The dependency of mode-mixity on the fracture energy is important to understand the fragmentation instability. The magnitude of G_c depends on the dissipative mechanisms happening in the process zone. These processes depend on the nature of the surrounding stress field that can be characterized by its triaxiality (which is zero for pure shear and infinite for hydrostatic pressure). To understand the physical origins of the mode-dependency on the fracture energy, it requires the study of the failure mechanisms within the process zone of PMMA which could be interesting to investigate in the future.

Bibliography

Mokhtar Adda-Bedia and Yves Pomeau. Crack instabilities of a heated glass strip. *Phys. Rev. E*, 52:4105–4113, Oct 1995. doi: 10.1103/PhysRevE.52.4105. URL https://link.aps.org/doi/10.1103/PhysRevE.52.4105. 4

D. Bahat. *Tectonofractography*. Springer Verlag, 1991. i, 5

T. Baumberger, C. Caroli, D. Martina, and O. Ronsin. Magic angles and cross-hatching instability in hydrogel fracture. *Phys. Rev. Lett.*, 100:178303, May 2008. doi: 10.1103/PhysRevLett.100.178303. URL https://link.aps.org/doi/10.1103/PhysRevLett.100.178303. 31, 81, 90, 91

B.R.K Blackman, H Hadavinia, A.J Kinloch, M Paraschi, and J.G Williams. The calculation of adhesive fracture energies in mode i: revisiting the tapered double cantilever beam (tdcb) test. *Engineering Fracture Mechanics*, 70(2):233 – 248, 2003. ISSN 0013-7944. doi: http://dx.doi.org/10.1016/S0013-7944(02)00031-0. URL http://www.sciencedirect.com/science/article/pii/S0013794402000310. 9

D. Bonamy and E. Bouchaud. Failure of heterogeneous materials: A dynamic phase transition? *Physics Reports*, 498(1):1 – 44, 2011. ISSN 0370-1573. doi: https://doi.org/10.1016/j.physrep.2010.07.006. URL http://www.sciencedirect.com/science/article/pii/S0370157310002115. 6

D. Bonamy and K. Ravi-Chandar. Interaction of shear waves and propagating cracks. *Phys. Rev. Lett.*, 91:235502, Dec 2003. doi: 10.1103/PhysRevLett.91.235502. URL https://link.aps.org/doi/10.1103/PhysRevLett.91.235502. 31, 72

Eran Bouchbinder, Ariel Livne, and Jay Fineberg. Weakly nonlinear fracture mechanics: experiments and theory. *International Journal of Fracture*, 162(1):3–20, Mar 2010. ISSN 1573-2673. doi: 10.1007/s10704-009-9427-3. URL https://doi.org/10.1007/s10704-009-9427-3. i, 4, 5, 91

Tamar Goldman Boué, Gil Cohen, and Jay Fineberg. Origin of the microbranching instability in rapid cracks. *Phys. Rev. Lett.*, 114:054301, Feb 2015. doi: 10.1103/PhysRevLett.114.054301. URL https://link.aps.org/doi/10.1103/PhysRevLett.114.054301. 24

Castem. Castem, a finite element package developed by cea, france.

T.J Chang and J.W Rudnicki. *Multiscale Deformation and Fracture in Materials and Structures The James R. Rice 60th Anniversary Volume*, volume 84 of *Solid Mechanics and its applications*. Kluwer Academic Publishers, Dordrecht, 2000. 1

Chih-Hung Chen, Tristan Cambonie, Veronique Lazarus, Matteo Nicoli, Antonio J. Pons, and Alain Karma. Crack front segmentation and facet coarsening in mixed-mode fracture. *Phys. Rev. Lett.*, 115:265503, Dec 2015. doi: 10.1103/PhysRevLett.115.265503. URL https://link.aps.org/doi/10.1103/PhysRevLett.115.265503. iv, 56, 57, 91

J. Chopin, A. Prevost, A. Boudaoud, and M. Adda-Bedia. Crack front dynamics across a single heterogeneity. *Phys. Rev. Lett.*, 107:144301, Sep 2011. doi: 10.1103/PhysRevLett.107.144301. URL https://link.aps.org/doi/10.1103/PhysRevLett.107.144301. 34, 37, 38, 41, 45, 73

Michele L. Cooke and David D. Pollard. Fracture propagation paths under mixed mode loading within rectangular blocks of polymethyl methacrylate. *Journal of Geophysical Research: Solid Earth*, 101(B2):3387–3400, 1996. ISSN 2156-2202. doi: 10.1029/95JB02507. URL http://dx.doi.org/10.1029/95JB02507. 55, 75, 79, 83

F. Corson, M. Adda-Bedia, H. Henry, and E. Katzav. Thermal fracture as a framework for quasi-static crack propagation. *International Journal of Fracture*, 158(1):1–14, Jul 2009. ISSN 1573-2673. doi: 10.1007/s10704-009-9361-4. URL https://doi.org/10.1007/s10704-009-9361-4. 4

Pierre-Philippe Cortet, Matteo Ciccotti, and Loïc Vanel. Imaging the stick–slip peeling of an adhesive tape under a constant load. *Journal of Statistical Mechanics: Theory and Experiment*, 2007(03):P03005, 2007. URL http://stacks.iop.org/1742-5468/2007/i=03/a=P03005. ii, 22

Marie-Julie Dalbe, Pierre-Philippe Cortet, Matteo Ciccotti, Loïc Vanel, and Stéphane Santucci. Multiscale stick-slip dynamics of adhesive tape peeling. *Phys. Rev. Lett.*, 115:128301, Sep 2015a. doi: 10.1103/PhysRevLett.115.128301. URL https://link.aps.org/doi/10.1103/PhysRevLett.115.128301. 21

Marie-Julie Dalbe, Juha Koivisto, Loïc Vanel, Amandine Miksic, Osvanny Ramos, Mikko Alava, and Stéphane Santucci. Repulsion and attraction between a pair of cracks in a plastic sheet. *Phys. Rev. Lett.*, 114:205501, May 2015b. doi: 10.1103/PhysRevLett.114.205501. URL https://link.aps.org/doi/10.1103/PhysRevLett.114.205501. 6

D. Dalmas, E. Barthel, and D. Vandembroucq. Crack front pinning by design in planar heterogeneous interfaces. *Journal of the Mechanics and Physics of Solids*, 57(3):446 – 457, 2009. ISSN 0022-5096. doi: https://doi.org/10.1016/j.jmps.2008.11.012. URL http://www.sciencedirect.com/science/article/pii/S002250960800210X. 34, 37, 73

J.F. Davalos, P. Madabhusi-Raman, P.Z. Qiao, and M.P. Wolcott. Compliance rate change of tapered double cantilever beam specimen with hybrid interface bonds. *Theoretical and Applied Fracture Mechanics*, 29(2):125 – 139, 1998. ISSN 0167-8442. doi: http://dx.doi.org/10.1016/S0167-8442(98)00024-X. URL http://www.sciencedirect.com/science/article/pii/S016784429800024X. 9

V. Démery, A. Rosso, and L. Ponson. From microstructural features to effective toughness in disordered brittle solids. *EPL (Europhysics Letters)*, 105(3):34003, 2014. URL http://stacks.iop.org/0295-5075/105/i=3/a=34003. iii, 35

A. Eberlein, H.A. Richard, and G. Kullmer. Facet formation at the crack front under combined crack opening and anti-plane shear loading. *Engineering Fracture Mechanics*, 174(Supplement C):21 – 29, 2017. ISSN 0013-7944. doi: https://doi.org/10.1016/j.engfracmech.2016.12.004. URL http://www.sciencedirect.com/science/article/pii/S0013794416307354. Special Issue on Multiaxial Fracture 2016. 55

F. Erdogan and G. C. Sih. On the crack extension in plates under plane loading and transverse shear. *Journal of Basic Engineering*, 85(4):519–525, Dec 1963. ISSN 0098-2202. doi: 10.1115/1.3656897. URL http://dx.doi.org/10.1115/1.3656897. 4, 42

A. S. Eremenko, S. A. Novikov, and A. P. Pogorelov. Investigation of the propagation and interaction of fast cracks in plexiglas. *Journal of Applied Mechanics and Technical Physics*, 20(4):477–480, Jul 1979. ISSN 1573-8620. doi: 10.1007/BF00905603. URL https://doi.org/10.1007/BF00905603. i, 5

Jean-Yvon Faou, Guillaume Parry, Sergey Grachev, and Etienne Barthel. How does adhesion induce the formation of telephone cord buckles? *Phys. Rev. Lett.*, 108:116102, Mar 2012. doi: 10.1103/PhysRevLett.108.116102. URL https://link.aps.org/doi/10.1103/PhysRevLett.108.116102. 4, 57

L. B Freund. *Dynamic fracture mechanics*. Cambridge University Press, Cambridge, New York, 1990. 24, 27

L. B. Freund and S. Suresh. *Thin Film Materials: Stress, Defect Formation and Surface Evolution*. Cambridge University Press, 2004. doi: 10.1017/CBO9780511754715. 57

Huajian Gao and James R. Rice. Shear stress intensity factors for a planar crack with slightly curved front. *Journal of Applied Mechanics*, 53(4):774–778, Dec 1986. ISSN 0021-8936. doi: 10.1115/1.3171857. URL http://dx.doi.org/10.1115/1.3171857. 43

Huajian Gao and James R. Rice. A first-order perturbation analysis of crack trapping by arrays of obstacles. *Journal of Applied Mechanics*, 56(4):828–836, Dec 1989. ISSN 0021-8936. doi: 10.1115/1.3176178. URL http://dx.doi.org/10.1115/1.3176178. 34, 35

A. N. Gent and C. T. R. Pulford. Micromechanics of fracture in elastomers. *Journal of Materials Science*, 19(11):3612–3619, Nov 1984. ISSN 1573-4803. doi: 10.1007/BF02396933. URL https://doi.org/10.1007/BF02396933. 81, 90

A. Ghatak and L. Mahadevan. Crack street: The cycloidal wake of a cylinder tearing through a thin sheet. *Phys. Rev. Lett.*, 91:215507, Nov 2003. doi: 10.1103/PhysRevLett.91.215507. URL https://link.aps.org/doi/10.1103/PhysRevLett.91.215507. i, 5

Gustavo Gioia and Michael Ortiz. Delamination of compressed thin films. volume 33 of *Advances in Applied Mechanics*, pages 119 – 192. Elsevier, 1997. doi: https:

//doi.org/10.1016/S0065-2156(08)70386-7. URL http://www.sciencedirect.com/science/article/pii/S0065215608703867. 4

Lucas Goehring, L. Mahadevan, and Stephen W. Morris. Nonequilibrium scale selection mechanism for columnar jointing. *Proceedings of the National Academy of Sciences*, 106(2):387–392, 2009. doi: 10.1073/pnas.0805132106. URL http://www.pnas.org/content/106/2/387.abstract. i, 5

Tamar Goldman, Ariel Livne, and Jay Fineberg. Acquisition of inertia by a moving crack. *Phys. Rev. Lett.*, 104:114301, Mar 2010. doi: 10.1103/PhysRevLett.104.114301. URL https://link.aps.org/doi/10.1103/PhysRevLett.104.114301. 27

R. V. Goldstein and N. M. Osipenko. Successive development of the structure of a fracture near the front of a longitudinal shear crack. *Doklady Physics*, 57(7):281–284, Jul 2012. ISSN 1562-6903. doi: 10.1134/S1028335812070087. URL https://doi.org/10.1134/S1028335812070087. iv, 55, 56

R. V. Gol'dstein and R. L. Salganik. Brittle fracture of solids with arbitrary cracks. *International Journal of Fracture*, 10(4):507–523, Dec 1974. ISSN 1573-2673. doi: 10.1007/BF00155254. URL https://doi.org/10.1007/BF00155254. 4, 42, 45, 51, 76

A. A. Griffith. Vi. the phenomena of rupture and flow in solids. *Philosophical Transactions of the Royal Society of London A: Mathematical, Physical and Engineering Sciences*, 221(582-593):163–198, 1921. ISSN 0264-3952. doi: 10.1098/rsta.1921.0006. URL http://rsta.royalsocietypublishing.org/content/221/582-593/163. 3, 33

Claudia Guerra, Julien Scheibert, Daniel Bonamy, and Davy Dalmas. Understanding fast macroscale fracture from microcrack post mortem patterns. *Proceedings of the National Academy of Sciences*, 109(2):390–394, 2012. doi: 10.1073/pnas.1113205109. URL http://www.pnas.org/content/109/2/390.abstract. 6, 24, 91

F. Hourlier and A. Pineau. Fissuration par fatigue sous sollicitation polymodales (mode i ondulé + mode iii permanent) d'un acier pour rotors 26ncdv14. *Mémoires Scientifique de la Revue de Métallurgies*, 76:175–185, 1979. 56, 79

Derek Hull. The effect of mixed mode i/iii on crack evolution in brittle solids. *International Journal of Fracture*, 70(1):59–79, Jan 1994. ISSN 1573-2673. doi: 10.1007/BF00018136. URL https://doi.org/10.1007/BF00018136. 43, 55, 75, 79

Derek Hull. *Fractography*. Cambridge University Press, 1999. 1

D.P. Isherwood and J.G. Williams. Some observations on the tearing of ductile materials. *Engineering Fracture Mechanics*, 10(4):887 – 895, 1978. ISSN 0013-7944. doi: https://doi.org/10.1016/0013-7944(78)90042-5. URL http://www.sciencedirect.com/science/article/pii/0013794478900425. 21

J. R. Kermode, T. Albaret, D. Sherman, N. Bernstein, P. Gumbsch, M. C. Payne, G. Csanyi, and A. De Vita. Low-speed fracture instabilities in a brittle crystal. *Nature*, 455(7217):1224–1227, Oct 2008. ISSN 0028-0836. doi: 10.1038/nature07297. URL http://dx.doi.org/10.1038/nature07297. 81, 91, 92

J. R. Kermode, L. Ben-Bashat, F. Atrash, J. J. Cilliers, D. Sherman, and A. De Vita. Macroscopic scattering of cracks initiated at single impurity atoms. *Nature Communications*, 4:2441 EP –, Sep 2013. URL http://dx.doi.org/10.1038/ncomms3441. Article. 91

W. G. Knauss. An observation of crack propagation in anti-plane shear. *International Journal of Fracture Mechanics*, 6(2):183–187, Jun 1970. ISSN 1573-2673. doi: 10.1007/BF00189825. URL https://doi.org/10.1007/BF00189825. iv, 55, 56, 79

Itamar Kolvin, Gil Cohen, and Jay Fineberg. Topological defects govern crack front motion and facet formation on broken surfaces. *Nature Materials*, pages EP –, Oct 2017. URL http://dx.doi.org/10.1038/nmat5008. 81, 90

V. Lazarus, F.-G. Buchholz, M. Fulland, and J. Wiebesiek. Comparison of predictions by mode ii or mode iii criteria on crack front twisting in three or four point bending experiments. *International Journal of Fracture*, 153(2):141–151, Oct 2008. ISSN 1573-2673. doi: 10.1007/s10704-008-9307-2. URL https://doi.org/10.1007/s10704-008-9307-2. 55, 75, 79

Véronique Lazarus, Jean-Baptiste Leblond, and Salah-Eddine Mouchrif. Crack front rotation and segmentation in mixed mode i+iii or i+ii+iii. part ii: Comparison with experiments. *Journal of the Mechanics and Physics of Solids*, 49(7):1421 – 1443, 2001. ISSN 0022-5096. doi: https://doi.org/10.1016/S0022-5096(01)00008-4. URL http://www.sciencedirect.com/science/article/pii/S0022509601000084. 55, 75

Jean-Baptiste Leblond and Laurent Ponson. Out-of-plane deviation of a mode i+iii crack encountering a tougher obstacle. *Comptes Rendus Mécanique*, 344(7):521 – 531, 2016. ISSN 1631-0721. doi: https://doi.org/10.1016/j.crme.2016.04.003. URL http://www.sciencedirect.com/science/article/pii/S1631072116300365. 42, 52

Jean-Baptiste Leblond, Alain Karma, and Véronique Lazarus. Theoretical analysis of crack front instability in mode i+iii. *Journal of the Mechanics and Physics of Solids*, 59(9):1872 – 1887, 2011. ISSN 0022-5096. doi: https://doi.org/10.1016/j.jmps.2011.05.011. URL http://www.sciencedirect.com/science/article/pii/S0022509611001141. 56, 57, 67, 69

Jean-Baptiste Leblond, Alain Karma, Laurent Ponson, and Aditya Vasudevan. On the effect of a mode-dependent fracture toughness upon isntability of coplanar crack propagation in mode i + iii. in prep. iv, 57, 65

P.S. Leevers. Crack front shape effects on propagation stability in thermosetting polyesters. *Theoretical and Applied Fracture Mechanics*, 6(1):45 – 55, 1986. ISSN 0167-8442. doi: https://doi.org/10.1016/0167-8442(86)90049-2. URL http://www.sciencedirect.com/science/article/pii/0167844286900492. 21

Bisen Lin, M. E. Mear, and K. Ravi-Chandar. Criterion for initiation of cracks under mixed-mode i + iii loading. *International Journal of Fracture*, 165(2):175–188, Oct 2010. ISSN 1573-2673. doi: 10.1007/s10704-010-9476-7. URL https://doi.org/10.1007/s10704-010-9476-7. 31, 55, 58, 91

Ariel Livne, Oded Ben-David, and Jay Fineberg. Oscillations in rapid fracture. *Phys. Rev. Lett.*, 98:124301, Mar 2007. doi: 10.1103/PhysRevLett.98.124301. URL https://link.aps.org/doi/10.1103/PhysRevLett.98.124301. 4

Benoit B. Mandelbrot, Dann E. Passoja, and Alvin J. Paullay. Fractal character of fracture surfaces of metals. *Nature*, 308:721 EP –, Apr 1984. URL http://dx.doi.org/10.1038/308721a0. 6

D Maugis and M Barquins. Fracture mechanics and the adherence of viscoelastic bodies. *Journal of Physics D: Applied Physics*, 11(14), 1978. URL http://stacks.iop.org/0022-3727/11/i=14/a=011. 19, 21

Daniel Maugis and Michel Barquins. *Stick-Slip and Peeling of Adhesive Tapes*, pages 205–222. Springer Netherlands, Dordrecht, 1988. ISBN 978-94-009-1349-3. doi: 10.1007/978-94-009-1349-3_14. URL https://doi.org/10.1007/978-94-009-1349-3_14. 21

S. Morel, N. Dourado, G. Valentin, and J. Morais. Wood: A quasi-brittle material. r-curve behavior and peak load evaluation. *Int. J. Frac.*, 131:385–400, 2005. 17

Stéphane Morel, Guillaume Mourot, and Jean Schmittbuhl. Influence of the specimen geometry on r-curve behavior and roughening of fracture surfaces. *International Journal of Fracture*, 121(1):23–42, May 2003. ISSN 1573-2673. doi: 10.1023/A:1026221405998. URL https://doi.org/10.1023/A:1026221405998. 9

A.B. Movchan, H. Gao, and J.R. Willis. On perturbations of plane cracks. *International Journal of Solids and Structures*, 35(26):3419 – 3453, 1998. ISSN 0020-7683. doi: https://doi.org/10.1016/S0020-7683(97)00231-X. URL http://www.sciencedirect.com/science/article/pii/S002076839700231X. 42, 43, 59

K. H. Pham and K. Ravi-Chandar. Further examination of the criterion for crack initiation under mixed-mode i+iii loading. *International Journal of Fracture*, 189(2):121–138, Oct 2014. ISSN 1573-2673. doi: 10.1007/s10704-014-9966-0. URL https://doi.org/10.1007/s10704-014-9966-0. 57, 58, 89, 91

K. H. Pham and K. Ravi-Chandar. The formation and growth of echelon cracks in brittle materials. *International Journal of Fracture*, 206(2):229–244, Aug 2017. ISSN 1573-2673. doi: 10.1007/s10704-017-0212-4. URL https://doi.org/10.1007/s10704-017-0212-4. 57

David D. Pollard and Atilla Aydin. Progress in understanding jointing over the past century. *GSA Bulletin*, 100(8):1181, 1988. doi: 10.1130/0016-7606(1988)100<1181:PIUJOT>2.3.CO;2. URL +http://dx.doi.org/10.1130/0016-7606(1988)100<1181:PIUJOT>2.3.CO;2. 55

David D.. Pollard, Paul Segall, and Paul T. Delaney. Formation and interpretation of dilatant echelon cracks. *GSA Bulletin*, 93(12):1291–1303, 1982. ISSN 0016-7606. doi: 10.1130/0016-7606(1982)93\<1291:FAIODE\>2.0.CO;2. URL http://bulletin.geoscienceworld.org/content/93/12/1291. 55, 76

Antonio J. Pons and Alain Karma. Helical crack-front instability in mixed-mode fracture. *Nature*, 464:85 EP –, Mar 2010. URL http://dx.doi.org/10.1038/nature08862. 56, 67

L. Ponson. *Tensile and compressive failure of brittle heterogeneous materials: Effective properties and fluctuation*. Habilitation à diriger des recherches, 2017. 34

Laurent Ponson and Daniel Bonamy. Crack propagation in brittle heterogeneous solids: Material disorder and crack dynamics. *International Journal of Fracture*, 162(1):21–31, Mar 2010. ISSN 1573-2673. doi: 10.1007/s10704-010-9481-x. URL https://doi.org/10.1007/s10704-010-9481-x. 34

Laurent Ponson, Harold Auradou, Philippe Vié, and Jean-Pierre Hulin. Low self-affine exponents of fractured glass ceramics surfaces. *Phys. Rev. Lett.*, 97:125501, Sep 2006. doi: 10.1103/PhysRevLett.97.125501. URL https://link.aps.org/doi/10.1103/PhysRevLett.97.125501. 6

Pizhong Qiao, Jialai Wang, and Julio F Davalos. Tapered beam on elastic foundation model for compliance rate change of {TDCB} specimen. *Engineering Fracture Mechanics*, 70(2):339 – 353, 2003. ISSN 0013-7944. doi: http://dx.doi.org/10.1016/S0013-7944(02)00023-1. URL http://www.sciencedirect.com/science/article/pii/S0013794402000231. 9

K. Ravi-Chandar and M. Balzano. On the mechanics and mechanisms of crack growth in polymeric materials. *Engineering Fracture Mechanics*, 30(5):713 – 727, 1988. ISSN 0013-7944. doi: https://doi.org/10.1016/0013-7944(88)90161-0. URL http://www.sciencedirect.com/science/article/pii/0013794488901610. 21

K. Ravi-Chandar and W. G. Knauss. An experimental investigation into dynamic fracture: Iii. on steady-state crack propagation and crack branching. *International Journal of Fracture*, 26(2):141–154, Oct 1984. ISSN 1573-2673. doi: 10.1007/BF01157550. URL https://doi.org/10.1007/BF01157550. 24

K. Ravi-Chandar and B. Yang. On the role of microcracks in the dynamic fracture of brittle materials. *Journal of the Mechanics and Physics of Solids*, 45(4):535 – 563, 1997. ISSN 0022-5096. doi: https://doi.org/10.1016/S0022-5096(96)00096-8. URL http://www.sciencedirect.com/science/article/pii/S0022509696000968. 6, 24

J.R. Rice. First-order variation in elastic fields due to variation in location of a planar crack front. *Journal of Applied Mechanics*, 52:571–579, 1985. 42

O. Ronsin, C. Caroli, and T. Baumberger. Crack front échelon instability in mixed mode fracture of a strongly nonlinear elastic solid. *EPL (Europhysics Letters)*, 105(3):34001, 2014. URL http://stacks.iop.org/0295-5075/105/i=3/a=34001. iv, 56, 58

J. Scheibert, C. Guerra, F. Célarié, D. Dalmas, and D. Bonamy. Brittle-quasibrittle transition in dynamic fracture: An energetic signature. *Phys. Rev. Lett.*, 104:045501, Jan 2010. doi: 10.1103/PhysRevLett.104.045501. URL https://link.aps.org/doi/10.1103/PhysRevLett.104.045501. 27

Jean Schmittbuhl, Stéphane Roux, Jean-Pierre Vilotte, and Knut Jorgen Måløy. Interfacial crack pinning: Effect of nonlocal interactions. *Phys. Rev. Lett.*, 74:1787–1790, Mar 1995. doi: 10.1103/PhysRevLett.74.1787. URL https://link.aps.org/doi/10.1103/PhysRevLett.74.1787. 34

Eran Sharon and Jay Fineberg. Confirming the continuum theory of dynamic brittle fracture for fast cracks. *Nature*, 397:333 EP –, Jan 1999. URL http://dx.doi.org/10.1038/16891. 27

G.C. Sih. *Mechanics of fracture*, volume 1. 1972. 4, 14

E. Sommer. Formation of fracture 'lances' in glass. *Engineering Fracture Mechanics*, 1(3):539 – 546, 1969. ISSN 0013-7944. doi: https://doi.org/10.1016/0013-7944(69)90010-1. URL http://www.sciencedirect.com/science/article/pii/0013794469900101. iv, 6, 31, 55, 56, 75, 79, 89

A. Srivastava, L. Ponson, S. Osovski, E. Bouchaud, V. Tvergaard, and A. Needleman. Effect of inclusion density on ductile fracture toughness and roughness. *Journal of the Mechanics and Physics of Solids*, 63(Supplement C):62 – 79, 2014. ISSN 0022-5096. doi: https://doi.org/10.1016/j.jmps.2013.10.003. URL http://www.sciencedirect.com/science/article/pii/S0022509613002111. 6

Subra Suresh and Elmar K. Tschegg. Combined mode i-mode iii fracture of fatigue-precracked alumina. *Journal of the American Ceramic Society*, 70(10):726–733, 1987. ISSN 1551-2916. doi: 10.1111/j.1151-2916.1987.tb04871.x. URL http://dx.doi.org/10.1111/j.1151-2916.1987.tb04871.x. 55

Y. Tanaka, K. Fukao, Y. Miyamoto, and K. Sekimoto. Discontinuous crack fronts of three-dimensional fractures. *EPL (Europhysics Letters)*, 43(6):664, 1998. URL http://stacks.iop.org/0295-5075/43/i=6/a=664. 90

Manish Vasoya, Jean-Baptiste Leblond, and Laurent Ponson. A geometrically nonlinear analysis of coplanar crack propagation in some heterogeneous medium. *International Journal of Solids and Structures*, 50(2):371 – 378, 2013. ISSN 0020-7683. doi: https://doi.org/10.1016/j.ijsolstr.2012.10.001. URL http://www.sciencedirect.com/science/article/pii/S0020768312004118. 34, 37, 38

Manish Vasoya, Aparna Beena Unni, Jean-Baptiste Leblond, Veronique Lazarus, and Laurent Ponson. Finite size and geometrical non-linear effects during crack pinning by heterogeneities: An analytical and experimental study. *Journal of the Mechanics and Physics of Solids*, 89(Supplement C):211 – 230, 2016. ISSN 0022-5096. doi: https://doi.org/10.1016/j.jmps.2015.12.023. URL http://www.sciencedirect.com/science/article/pii/S0022509615303884. 41

Stéphane Vernède, Laurent Ponson, and Jean-Philippe Bouchaud. Turbulent fracture surfaces: A footprint of damage percolation? *Phys. Rev. Lett.*, 114:215501, May 2015. doi: 10.1103/PhysRevLett.114.215501. URL https://link.aps.org/doi/10.1103/PhysRevLett.114.215501. 6

H. Wallner. *Z. Phys.*, 114, 1939. 31, 72

P. Waters and A. A. Volinsky. Stress and moisture effects on thin film buckling delamination. *Experimental Mechanics*, 47(1):163–170, Feb 2007. ISSN 1741-2765. doi: 10.1007/s11340-006-9346-4. URL https://doi.org/10.1007/s11340-006-9346-4. i, 5

CW Wu. Maximum energy release rate criterion. *Journal of Elasticity*, 8:2235–2257, 1978. 4

Salim Yamini and Robert J. Young. Crack propagation in and fractography of epoxy resins. *Journal of Materials Science*, 14(7):1609–1618, Jul 1979. ISSN 1573-4803. doi: 10.1007/BF00569280. URL https://doi.org/10.1007/BF00569280. 21

B. Yang and K. Ravi-Chandar. Crack path instabilities in a quenched glass plate. *Journal of the Mechanics and Physics of Solids*, 49(1):91 – 130, 2001. ISSN 0022-5096. doi: https://doi.org/10.1016/S0022-5096(00)00022-3. URL http://www.sciencedirect.com/science/article/pii/S0022509600000223. 4

J. R. Yates and K. J. Miller. Mixed mode (i + iii) fatigue thresholds in a forging steel. *Fatigue and Fracture of Engineering Materials and Structures*, 12(3):259–270, 1989. ISSN 1460-2695. doi: 10.1111/j.1460-2695.1989.tb00532.x. URL http://dx.doi.org/10.1111/j.1460-2695.1989.tb00532.x. 55, 75

A. Yuse and M. Sano. Transition between crack patterns in quenched glass plates. *Nature*, 362:329 EP –, Mar 1993. URL http://dx.doi.org/10.1038/362329a0. i, 4, 5

Alan T. Zehnder. *Fracture Mechanics*, volume 62. Springer Netherlands, 2012. i, 2, 4